TOWARD DIFFRACTION-LIMITED HIGH POWER FIBER LASER SOURCES

by

Tsai-wei Wu

A dissertation submitted in partial fulfillment
of the requirements for the degree of
Doctor of Philosophy
(Electrical Engineering)
in The University of Michigan
2010

Doctoral Committee:

Professor Herbert G. Winful, Chair
Professor Almantas Galvanauskas
Professor Peter Miller
Professor Theodore B. Norris
Professor Stephen C. Rand

© Tsai-wei Wu 2010
All Rights Reserved

DEDICATION

To my family

ACKNOWLEDGEMENTS

Above all, I would like to express my deepest gratitude to my advisor Professor Herbert G. Winful for all his support and guidance through my PhD years. If it were not his patience, encouragement and instruction, it would not be able for me to come up to this level and achieve this feat. He provided me much freedom to explore diverse topics and thoughts and inspired me to look into the cores and the nature of the problems, instead of just giving me the answers directly. In spite of his tight schedule, he always manages to discuss with me and helps me proceed with my research work. I want to extend my appreciation for his assistance and inspirations especially when I felt lost or went through difficulties. I learnt a lot from him both said and unsaid.

I am also extremely grateful to Professor Almantas Galvanauskas, Professor Peter Miller, Professor Theodore Norris and Professor Stephen Rand for agreeing to be my dissertation committee and taking time to evaluate my thesis work and to participate in the final defense. Special thanks are given to Prof. Galvanauskas for his supports in the laser array project. I benefit greatly and acquired many physical insights through valuable discussions with him. I enjoyed very much the course "Nonlinear Partial Differential Equations" taught by Prof. Miller which truly broadened and sharpened my mind and made me realize how shallow my mathematical perception was. I am also thankful to Prof. Norris and Prof. Rand as well for their patience in the correspondence of scheduling the defense meeting.

I wish to thank all my friends in Ann Arbor who had accompanied me through all these years. Among them, I am particularly thankful to Dr. Guoqing (Noah) Chang who had been more than a friend; he is also a mentor that generously helped and assisted me through research difficulties and I felt there are a lot more I need to learn from him. I would like to thank Dr. Chi-Hung Liu for being a great friend and senior to me and other EECS classmates: Hsien-Kai Hsiao, Yihao Chen, Galen (Chia-Chu) Chen and my collaborator from Galvanauskas' lab: Wei-zung Chang as well.

The fellowships of my bible study group members: Dianne Roeper, Katharine Chang, Angela Lausche, Dr. Ching-Mei Lin, Jane (Yu-Chen) Liu, Katie Glupker, Dr. Abby Wolfe, Shinobu Yoshida, Jean (Kang-Ching) Chu, Karen (Kai-Yuan) Hou, Toni (Yu-Ching) Liao and Tonye Burutolu have enriched my life and made the challenging PhD studies less stressful. I enjoy very much their company and really cherish and appreciate their friendships.

Most importantly, I want to express my gratitude to my parents Chi-Jui Wu, Yun-Mei Hsu, my sister Tsai-Chin Wu and my husband Meng Cui. Their endless loves and supports have been the greatest strength giving me confidence and courage to face and cope all the difficulties in my life. Without their caring and love, it may not be possible for me to accomplish any of those; therefore, I devote this dissertation to my family.

TABLE OF CONTENTS

LIST OF FIGURES

LIST OF TABLES

CHAPTER I

Introduction

1

1.1 Diffraction-limited high power fiber lasers: a brief review

Realization of high power coherent laser sources has been an ongoing effort since 1970s due to their utility in science and industry. High power coherent sources are needed in many fields, including material processing, remote sensing, fundamental science, medical and military applications. Among the many different kinds of lasers that are available, diode lasers and bulk solid-state lasers are capable of generating up to kilowatt output powers, yet they often display poor beam quality or suffer from beam distortions due to the thermo-optic effects at high power levels [1]. They are thus used for applications where good beam profiles are not essential. Others applications, however, require more than that. The demand for diffraction-limited high power radiation has led to the development of fiber lasers because of some of their attractive features: low propagation losses, ideal beam quality from single mode fibers, broad gain spectrum from rare-earth doping, compactness and robust operation. High quantum efficiency is also an important factor which makes fiber lasers superior to other kinds. Due to its large surface-to-active-volume ratio [2], the beam quality is mainly determined by the physical structure of the fiber itself and is relatively immune to thermal issues. The maturation of fiber fabrication technology further made possible various fiber-based components and

devices, which would allow all-fiber configurations to avoid any diffractive losses in free space optics.

Along the path of developing high power coherent laser sources with diffraction-limited beam quality, the power scalability of fiber lasers, however, is limited by the presence of nonlinear effects associated with the third-order susceptibility $\chi^{(3)}$ [3]. The interaction of strong light fields with dielectric materials, e.g. SiO_2, induces a nonlinear polarization field which gives rise to a variety of phenomena including self-phase modulation (SFM), third harmonic generation (THG), four-wave mixing (FWM), stimulated Raman scattering (SRS) and stimulated Brillouin scattering (SBS). Depending on the application, these phenomena are beneficial in some processes such as the formation of solitons, mode-locking, super continuum generation, Raman lasers/amplifiers, optical wavelength conversions and nonlinear spectral broadening in fiber chirp pulse amplification (FCPA) system. Nevertheless, for the purpose of extracting high powers from fiber lasers, these mechanisms are generally detrimental and should be suppressed or bypassed. To this end, several techniques have been developed based on two main working principles: laser arrays or coherent beam combining and large-mode-area (LMA) fibers with distributed filtering of higher-order-modes.

1.1.1 **Laser array approach**

Since nonlinear processes occur at high optical intensities, the array approach combines a number of individual lasers at relatively lower intensity fields in the attempt to obtain high total powers in free space. It can be further categorized into two subsets of active and passive combining where active arrays implement electronic phase detection and feedback instantaneously to adjust the fiber length/phase variations as illustrated in

Figure 1.1. Although successful demonstrations of active combining have been reported with fiber lasers by Shay, Agust and Bellanger and references therein [4-8], the active-feedback implementation involves complicated electronics for real-time phase corrections and some issues must be considered including determining detection method and algorithms for optical path length difference [1] and the speed limitation of electronics for dynamical adaption of phase variations in optical path length. In an early attempt to phase a 100-element array of semiconductor amplifiers [9], a total output of 7.9 W is obtained yet only 1.6 W resides within the central lobe. The phase equalization is thus partial and static [1]. Of course, much progress has been made on active combining since, but with this approach, the system requires space that increases quickly with array size and the idea of complicated schemes for implementation and heavy loads of signal processing are against the principles of pursuing compact and robust optical laser sources. Active arrays are thus sometimes less favored.

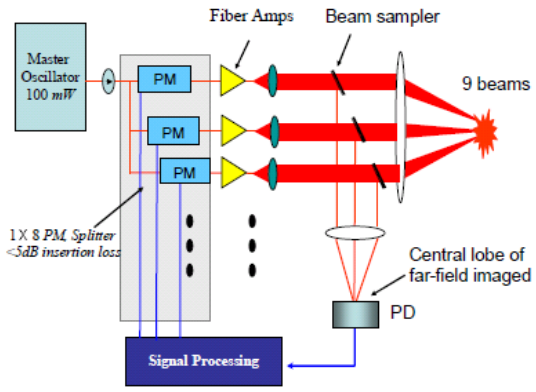

Figure 1.1: Schematic of active coherent combining for laser arrays. [7, 8]

Passive laser arrays, on the other hand, have long been subject to extensive investigations almost as soon as the invention of lasers in 1950s. Initial motivations for studying passive laser arrays were not to develop high power radiation sources but to

understand the physics of synchronization between coupled oscillators. It was not until later that the semiconductor laser array structures received great attention for their potentials to provide high-brightness coherent light and now, more recently fiber laser arrays are attracting similar attention.

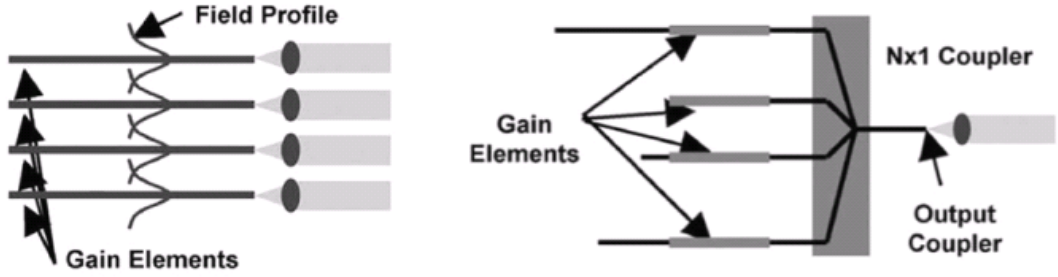

Figure 1.2: Distributed (left) and discretely (right) coupled passive laser arrays. [1]

Based on the implementation methods, passive laser arrays can be divided into distributed coupling and discrete coupling configurations as illustrated in Figure 1.2. For distributed laser arrays, the laser elements are positioned sufficiently close to each other so their field distributions overlap with adjacent ones and the coupling takes place through leaky or evanescent waves. This approach is particularly popular for semiconductor laser arrays due to the short nature of their laser cavities and is relatively easy for fabrication. As for distributively-coupled fiber laser arrays, multicore fibers [10-12] were originally considered. However, very few successful experiments were reported using this scheme, possibly because it is quite difficult to maintain constant separations among cores over a long distance, which is typically the case for fiber laser systems. Therefore, attention have turned to the simple alternative of discrete coupling method, where field exchange only happens within a short region as shown in Figure 1.2.

In the aspects of beam combining, at least three methods exist for discretely-coupled fiber laser arrays including Talbot effects [13-19], self-Fourier cavities [20] and the fiber directional couplers as illustrated in Figure 1.3. The first two of them are based on diffractive coupling while directional couplers enable compact and all-waveguide configurations avoiding any diffractive losses. Successful demonstrations of coherent beam combining utilizing 50:50 directional couplers have been reported by many groups with the aid of differential output coupling coefficient. This way, diffraction-limited high powers, in proportional to the array elements, are truly obtained without any ambiguities [21] from partially-reflected light at the output port. Although up to 200 W powers have been reported based on this approach [22, 23], the combining mechanism is not fully understood and further power scaling is inhibited by drastic decreases in the combining efficiency accompanied by an increasing level of power fluctuations.

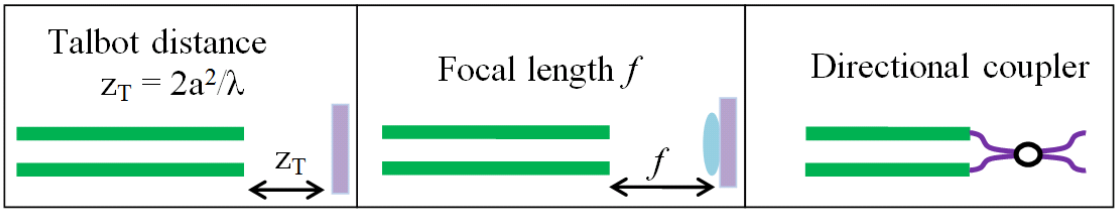

Figure 1.3: Schematic of coupling method of discretely coupled laser arrays by the means of (from left to right) Talbot effects, self-Fourier cavity and directional couplers.

1.1.2 **Large mode area approach**

Somewhat similar to the idea of laser array approach, the use of large mode area (LMA) fibers pursues a high total output power while keeping low optical intensities per square area. A typical step-index single mode fiber (SMF) has a core diameter of ~8 μm and mode field diameter (MFD) of ~10 μm [24]. The powers carried by SMFs are often

very limited due to the effects of third-order nonlinear refraction occurring at high intensity fields. The critical intensities for the onset of nonlinear phenomena is associated with high electric fields close to the interatomic level of 10^7 V/m [25] and this, according to simple formulation of $P = \int_{MFD} (c_0 \varepsilon_0 n |E|^2 /2) dA,$ sets the maximum powers to be on the order of Watts under narrow-linewidth operations [26]. In order to go beyond this threshold, one of the intuitive approaches is to enlarge fiber core diameters. This way the total powers scale up proportionally with effective mode areas while local intensities can be kept low to avoid nonlinear or thermal issues. Unfortunately, a direct consequence of LMA fibers is the emergence of a great number of guided modes supported by the relaxed boundary conditions. As illustrated in Figure 1.4, unlike the fundamental mode (top left), higher order modes generally have multi-lobed spatial distributions and distinct effective refractive indices, (i.e. different phase velocities) and the resulting beam profiles thus feature fragmented and time-varying interference patterns instead of the clean, focused ones in the fundamental mode as seen in Figure 1.5.

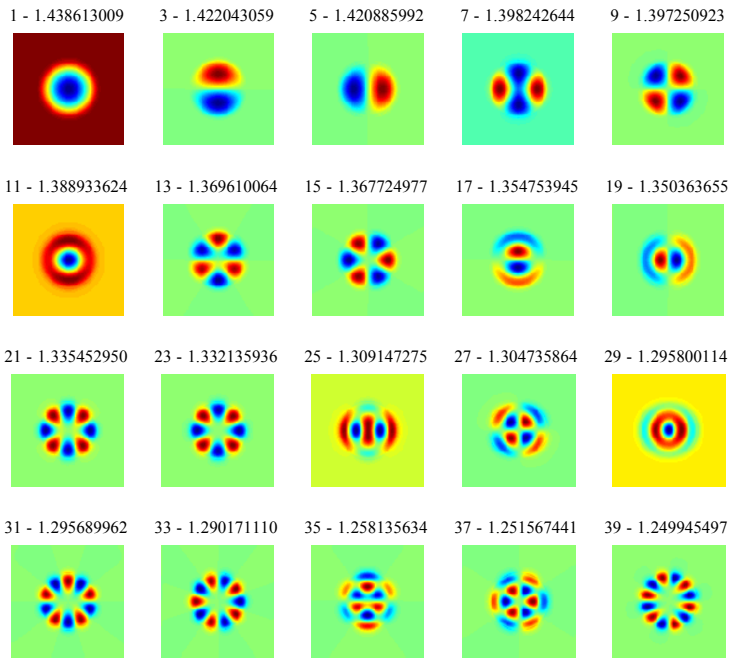

Figure 1.4: Eigenmodes of a LMA fiber calculated by finite difference frequency domain (FDFD) method with mode numbers and the corresponding effective refractive index shown above. Note only odd number modes are plotted since symmetry gives two degenerate modes for each polarization direction. Simulation parameters used: λ = 1.5 μm, index of core = 1.45, index of cladding = 1, core diameter = 6 μm.

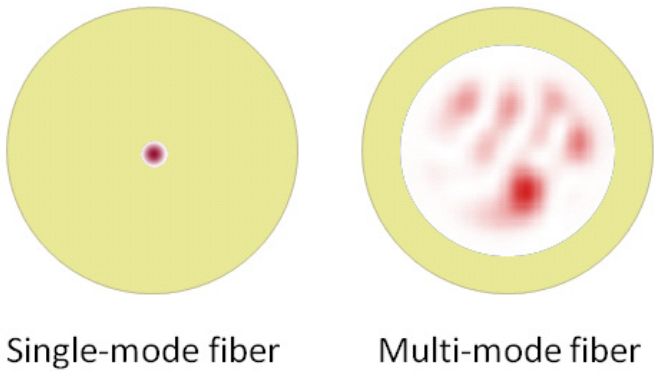

Figure 1.5: The beam quality of SM and MM fibers.

The number of eigenmodes within a multimode (MM) fiber can be estimated approximately by $4V^2/\pi^2$, where V is the normalized frequency such that

$$V = \frac{2\pi}{\lambda} a \sqrt{n_{core}^2 - n_{cladding}^2} \tag{1.1}$$

λ is the optical wavelength in vacuum, *a* is the fiber core radius and the expression of square root refers to numerical aperture *NA* [27]. For SMFs, *V* is smaller than 2.405 and the beam quality factor, M^2, is ~1 for diffraction-limited beams. When more modes are present, the beam quality degrades and the corresponding M^2 becomes greater than 1. To overcome such limitations, it is possible to build LMA fibers with $V < 2.405$ to ensure single-mode operations at the expense of reducing *NA* [28]. As seen in Eq. (1.1), *NA* is the measure of the contrast between core and cladding refractive indices. A waveguide of high *NA* means strong guiding, i.e. the modes are well-confined to the core, and this leads to the robust and rugged operation of fibers since they are insensitive to outer disturbances. For that reason, lowering *NA* imposes greater bending losses (as shown in Figure 2.16) and raises the bending limitations for such LMA fibers that it may find restricted use in many applications.

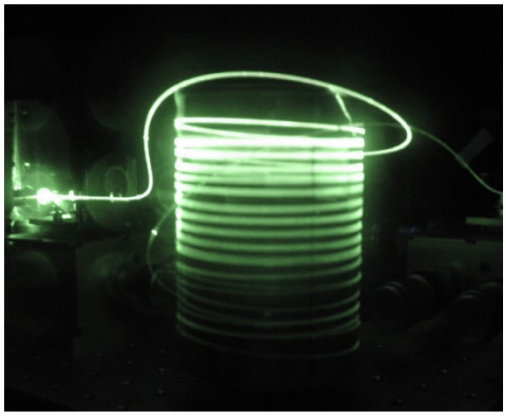

Figure 1.6: A LMA fiber coiled around a can. (Courtesy of Guo-qing Chang.)

Another approach sharing the similar principle is reported by Koplow *et al* that they achieve SM operation by wrapping a 25μm core diameter MM fiber ($V \sim 7.4$) around a

cylindrical mandrel (as in Figure 1.6) to effectively suppress higher order modes [29]. To understand the origin of these differential losses, we need to first review the waveguide theories. Based on the ray optics, light traveling within fibers is described by total internal reflections with each guided mode propagating at a certain angle above the critical value θ_c. As shown in Figure 1.7(a), the angle θ is defined as the one between the incident ray and the perpendicular axis to the core/cladding interface. Among all the modes, the fundamental mode has largest θ and experiences the lowest number of reflections from the wall. The angle decreases monotonically for higher order modes until it hits the cut-off condition set by θ_c that no mode exists for θ smaller than θ_c, at which light escapes into cladding through normal refractions. When the fiber is curved, the geometry distorts and all angles diminish somewhat as exemplified in Figure 1.7(b). It is clear then higher order modes are more likely to leak through bending since their angles are closer to θ_c than that of fundamental modes and may drop below the critical angle at bends. In this way, differential losses can be introduced to achieve SM operation in MM fibers. Successful demonstration of high power fiber lasers/amplifiers using this method has been reported up to 500W in a 30 μm MM fiber [30].

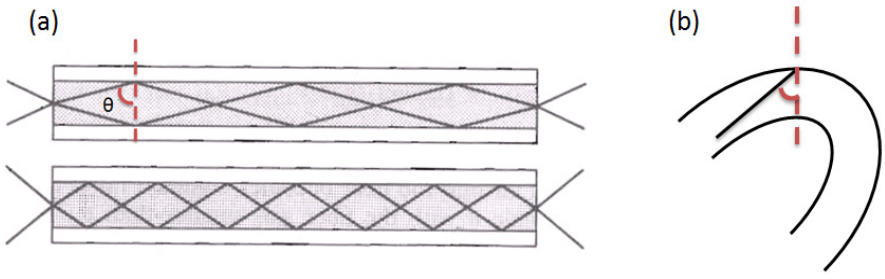

Figure 1.7: (a) The definition of θ is illustrated. The upper fiber shows the fundamental or lower order mode propagation as opposed to higher order ones in the lower figure. [Saleh and Teich.] (b) The illustration of a bent fiber and its resulting angle distortion.

Beyond this point LMA fibers of even larger MFDs are, without doubts, being pursued persistently. However, continuing this approach for higher powers is restricted by the bottleneck of insufficient discernible differential losses induced by bending when core diameters exceed 30 μm. This can be understood as follows. Considering a LMA fiber of fixed refractive indices for core and cladding, enlarging its core size would lead to more modes accommodated according to Eq. (1.1). In theory, each of these modes propagates with an effective refractive index enclosed by n_{core} and $n_{cladding}$ (or equivalently, an angle θ between 90º and θ_c), increasing the number of modes would naturally result to denser distribution of indices (or angles) and so to closer mode separations. Therefore, distinguishing between the modes becomes a challenging task and some sort of enhanced filtering mechanism is required in order to proceed further in power scaling.

1.2 Dissertation outline

As introduced in Sec. 1.1, in spite of some progress developed for each of the method, challenges and difficulties are encountered inevitably along the way. With the goal of achieving high-power high-radiance fiber sources with diffraction-limited beam quality, this thesis work presents our efforts to study, analyze and elucidate the mechanism and limitation of rare-earth doped or Raman fiber laser arrays and bent microstructured LMA fibers with each chapter centering on one fiber structure. In CHAPTER II, (Model for coherent combining in passive fiber laser arrays) a novel and effective model utilizing nonlinear Schrödinger equations is proposed for the first time to study the array behaviors of discretely coupled rare-earth doped fiber lasers arrays. Based on this model, the combining mechanism is elucidated and the mystery of decreasing

combining efficiency for large array sizes is resolved. Effects such as electronic nonlinearity, gain dynamics and the backward propagating waves are shown to have little impact on combining performance. Moreover, the resonance mode periodicity is demonstrated to be determined by the greatest common divisor of the participating fiber lengths both numerically and analytically. In CHAPTER III, the important question of the decreasing combining efficiency with increasing array size is explored systematically for the first time for up to 16 laser elements. Both the experimental results of power efficiencies and power fluctuations, which are rarely mentioned in the literature, are fitted with the newly developed model and they show very good agreement with each other. At the end of CHAPTER III, the ultimate solution of limited power scalability by the means of optical phase conjugation mirrors is simulated and demonstrated as a promising direction for future investigations. In CHAPTER IV, (Raman fiber laser arrays) we propose and analyze fiber laser arrays based on Raman gain for the first time. Beginning with a simplified condition of single-mode analysis, it is shown that the nonlinear phases inherent in SRS are essential to the phase-locking of the array outputs. We also carry out the analysis of more realistic scenario of multi-longitudinal-mode operation and it shows huge deviations from that of single mode results. In CHAPTER V, which covers bending performance of leakage channel fibers) our efforts focused on modal analysis of bent microstructured leakage channel fiber (LCF) fibers. With proper mathematical formulations, the complex effective indices of the leaky modes within curved fibers could be solved exactly for accurate evaluation of the differential mode losses. We look for proper designs of micro-structured fibers so as to induce sufficient differential modal losses between fundamental and all other higher-order modes.

CHAPTER II

Model for coherent beam combining in passive fiber laser arrays

2

2.1 Introduction

There is much current interest in scaling up the output power of a single fiber laser by coherently combining the fields of several amplifying fibers into a high-brightness, diffraction-limited beam [11, 31-35]. One approach that has been pursued with some success is the use of discrete 50:50 directional couplers to create an interferometric system of coupled amplifier pairs in a composite cavity. This pair-wise combining scheme forms the basis of a tree architecture that can, in principle, be scaled up to any even number 2x*N* of fiber lasers. Several groups have demonstrated highly efficient coherent beam combining using up to eight erbium-doped fiber lasers.

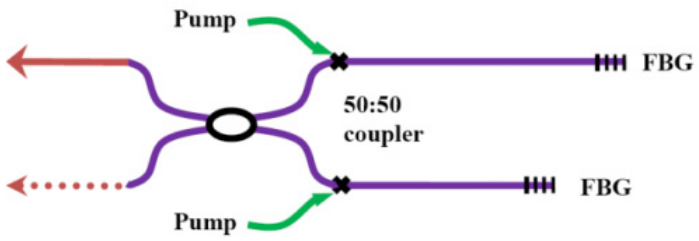

Figure 2.1: A two fiber laser array structure.

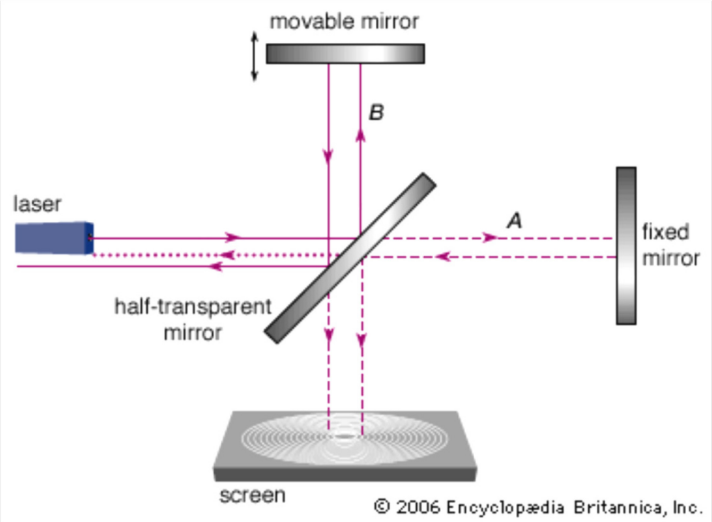

Figure 2.2: A Michelson interferometer

In principle, a two-channel fiber laser array is just a Michelson interferometer (Figure 2.2) except that both arms are replaced by rare-earth-doped fibers. The 50:50 directional coupler acts like a beam splitter as shown in Figure 2.1. Constructive or destructive interference occurs depending on the relative phase of the incident fields if their coherence is assumed. The waves generated from the individual active fibers then add on or cancel out with each other accordingly at the coupler outputs. Since uneven fiber lengths directly relate to the accumulated phase difference of the propagating waves, one might suppose that successful beam combination would require accurate control of fiber lengths. However, experimentation has verified the robust and reliable operation of power addition of two-channel fiber laser arrays even when their lengths are not carefully adjusted. Furthermore the combining efficiency has been seen to drop dramatically when the number of fiber amplifiers exceeds eight, thus limiting the scalability of this method.

Several theoretical analyses have been published aimed at explaining the limitation of power scaling and elucidating the nature of the beam combining process [21, 22, 31,

36-40]. These include static calculations of the spectral response of passive multi-arm interferometers [40] and dynamic simulations based on iterative maps for the rate equations and a single-longitudinal-mode cavity field [21, 38]. Currently there appears to be some debate as to whether the coherent phasing of multiple fiber amplifiers is a "self-organization" process involving coupled nonlinear oscillators [21, 22, 38] or the result of an accidental coincidence between the frequency combs of multiple resonators. Any attempt to resolve this debate must take into account the multiple-longitudinal-mode nature of fiber lasers and allow for arbitrary length differences of the amplifying fibers. Yet the only published dynamic studies are restricted to a single mode, have assured a fixed phase difference, and yield no spectral information.

Here we present a model based on the amplifying Nonlinear Schrödinger Equation that incorporates the multiple longitudinal modes of a fiber laser and allows for the natural selection of the resonant array modes that experience the minimum loss. It is a propagation model that takes into account gain saturation, fiber nonlinearity, group velocity dispersion, and the loss dispersion of bandwidth limiting elements in the complex cavity. In agreement with experimental observations, the model shows that efficient coherent beam combining occurs without the need for interferometric control of fiber lengths so long as there is sufficient bandwidth available. It is the first model, to the best of our knowledge, that provides detailed spectral information on the output of coherently combined fiber lasers.

2.2 Model reviews

Ever since the first demonstration of coherent combining in discretely coupled fiber laser arrays, there have been a number of theoretical models proposed to clarify the

mechanism for successful combining regardless of fiber lengths control and to explain the combining efficiency drop with increasing array elements. In this section, we briefly review and discuss each of these methods considering their modeling approaches, calculation results and the implications or predictions of array behaviors. We will also point out how some of them are deficient in capturing the essence of combining process and thus deviate from actual experimental conditions or observations.

One of the first papers is an on-line memo provided by Siegman in 2004 [40] where he derives the statistical distributions of effective power reflectivity and mode losses in an *N*-to-1 coupled fiber laser structure in terms of the number of array elements *N*. The coupling method is taken to be general and is not specified explicitly. In his discussion, the clarification has been made to the discretely coupled fiber array that it is viewed as a composite laser cavity with internal coupling and one common feedback instead of an assembly of independent individual fiber oscillators coupled externally [41]. Since coupled oscillators may be more complicated and difficult to analyze, all the theoretical models of our interests confine themselves to the former case. The specific expression for output power variations is derived starting from simple addition of the laser fields

$$\bar{r} = \frac{1}{N}\sum_{k=1}^{N} e^{j\theta_k} \tag{2.1}$$

where $\bar{r}$ is the complex amplitude reflectivity locating in front of the single output port and θ_k stands for the total phase of the electric field after roundtrip propagation within the *k*-th fiber [40]. Naturally, θ_k depends on the frequencies of the optical waves and the exact fiber lengths. In practice there is no deliberate length control and a wide range of possibilities exists for the combination of *N* phase variables, it is thus reasonable taking

statistical approaches by assuming θ_k distributing randomly and uniformly over the range of 0 to 2π. In this way, the probability density distributions for the amplitude reflection coefficient magnitude $r = |\tilde{r}|$ and associated power reflection coefficient $R = |r|^2$ can be calculated as a function of *N*. The resulting probability densities of obtaining close to 100% power reflectivity are found to decrease rapidly with array size (not shown here.) Defining the reflection loss $\delta = 1 - R$, the final results of cumulative probabilities of an array with the internal loss ≤ δ are calculated and summarized in Figure 2.3 [40].

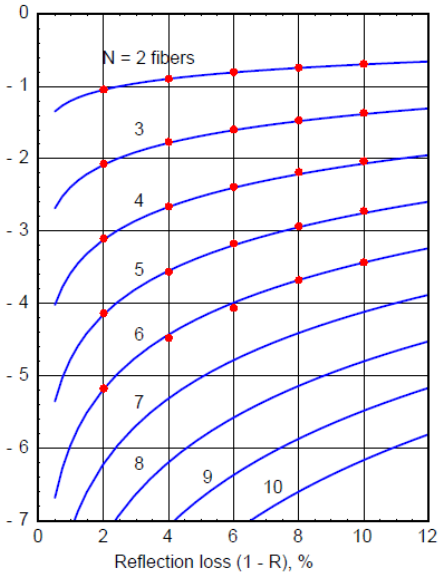

Figure 2.3: The cumulative probabilities of an *N*-channel fiber laser array with internal losses ≤ δ = 1 – *R* [40].

To interpret Figure 2.3, we consider the curve of *N* = 2 and it suggests that up to 10% of the axial modes in a two-channel fiber array will have internal losses δ ≤ 2%, and up to 20% will have internal losses δ ≤ 10% [40]. As *N* increases, the probabilities of finding the longitudinal modes with the same amount of loss δ drop monotonically. In the

extreme case there may be less than one mode existing in the spectrum (e.g. given 30000 axial modes, the fraction number of modes of $\delta \leq 10\%$ is $\sim 1.6 \times 10^{-5}$ for $N = 8$ [40] and so only approximately 0.5 modes will be found.) When no or less than one mode could lase in the array, the decrease of the combining efficiencies can be understood intuitively. Indirectly, the model takes into account the multiple longitudinal modes nature of fiber lasers and computes the number of modes selected based on the probability calculations with known spectral bandwidth and free spectral ranges. The degree of efficiency drop, however, is only vaguely related to the sparsity of coincidental longitudinal modes at large N and no information is given for the connection between exact combining efficiency and the array size. Besides, its formulation implies that combining efficiencies can be considerably improved regardless of the array size N as long as infinite bandwidth is available (See the paragraph below Fig. 5 in Ref. [40].) The idea is of course unrealistic and misleading in some sense. Finally, it is purely static modeling without considering gain dynamics and the frequency pulling effects and the specific form of coupling method is neglected as well.

The second proposal is the model for high gain fiber laser arrays by Roger *et al*, where Rigrod analysis is applied to wave propagation based on the fact that small power reflection coefficient ~ 4% at the output coupler leads to large power transmission and thus to nonuniform distribution of field intensities along the fiber. Starting with circulating field theory, the model numerically solves the wave propagation equation together with the rate equation using finite difference iterative maps. The coupling method is represented by a linear coupling matrix and the simulation is initiated with low intensity spontaneous emission. The paper emphasizes the gain dynamics of array

performance, as opposed to that of Siegman's static modeling and the simulation for a five-element fiber laser array as shown in Figure 2.4 where b and r_0 standing for brightness measure and phase-locking parameter respectively.

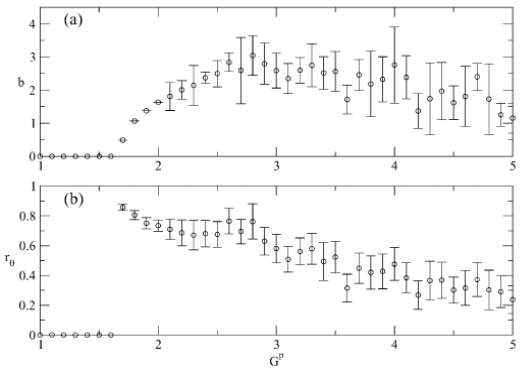

Figure 2.4: (a) Brightness and (b) the phase locking parameters v.s. pumping values for a five elements all-to-all coupled laser array. [21]

Although the interesting result is obtained in this analysis that the array coherence seems to depend on the pumping strength G^p, the basis of the dynamic model is built on single-longitudinal-mode operation, and identical fiber lengths must be assumed for simulation. In this case, the model is confined to impractical array parameters and finds limited use for coherent combining where fiber lengths are not controlled. Around the same time, Kouznetsov *et al* presented an analytical estimate for the number of lasers that can be efficiently combined by

$$\eta = 1 - \frac{\pi^2}{2}\exp(-2\frac{\ln(kL)}{N-1}) \tag{2.2}$$

N is the maximal number of lasers with combined efficiency η. k refers to the bandwidth and L is the fiber length. Although the formula agrees fairly well with other simulation results as seen in Figure 2.5 [37], the reliability of this simple estimate is still debatable. Take an example of N = 16, using the parameters provided by the paper with

$kL = 778\times10^3$ corresponding to a spectral width of 10 nm [37], the efficiency calculated by Eq. (2.2) gives 19% for 16-channel combining. This, however, is considerably lower than the experimental demonstrations of 54% with comparable bandwidth of 10 nm [42]. In addition, the model is limited to cold cavity analysis and provides no further insights to the combining mechanism as we are looking for.

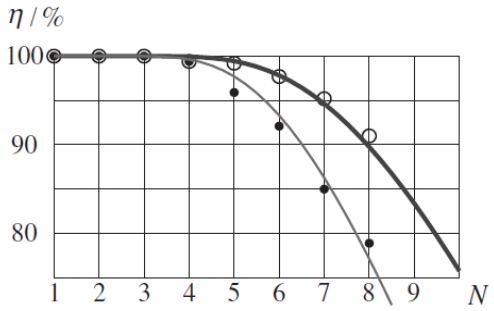

Figure 2.5: The solid curves represent the estimates from Eq. (2.2) [37]. Circles and dots are simulation data from Shirakawa *et al* [43] for different spectral linewidths Δν = 10nm and 0.6 nm respectively.

A series of papers [44-46] have been published utilizing the same model of Ref. [21] to study the synchronization of fiber laser arrays. Although they attempt to explore a combining mechanism as addressed in the abstract of Ref. [44], their efforts are futile and incomplete since, in principle, the single-mode model is only suitable for array configuration, and not for combining configuration, where unbalanced output coupling coefficients and uneven fiber lengths must be taken into account.

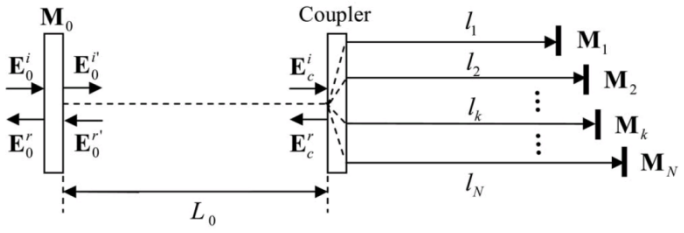

Figure 2.6: An N-arm Michelson interferometer resonator considered in [36]

Another approach proposed by Cao *et al* is based on studying an *N*-arm Michelson interferometer as depicted in Figure 2.6. In some combination of Siegman's and Roger's approaches, the simulation method adopts circulating field theory along with randomly and uniformly distributed phase/length variables and also simple additions of optical waves (Eq. (2.1)) as coupling. Rather than deriving probability density functions [Siegman], the equivalent reflectivity R_{eff}, defined by Eqs. (2.3) and (2.4), is numerically simulated iteratively for a sufficient number of times.

$$R_{eff} = \left| \frac{E_0^r}{E_0^i} \right|^2 = \left| \frac{r_0 + r_{kN} e^{j(2\pi/\lambda)(2L_0)}}{1 + r_0 r_{kN} e^{j(2\pi/\lambda)(2L_0)}} \right|^2 \tag{2.3}$$

and

$$r_{kN} = \frac{E_c^r}{E_c^i} = \frac{1}{N} \sum_{k=1}^{N} r_k e^{j(2\pi/\lambda)(2L_k)} \tag{2.4}$$

The combining efficiency is taken to be the maximum equivalent reflectivity [36]. One interesting point of these results is that in addition to combining efficiency, the power fluctuation is produced as well in terms of the array size *N*, which is rarely mentioned in other literatures. Since it involves multimode concepts, the model is valid for exploring combining physics. Some of its predictions, however, are not intuitive such as huge fluctuation > 40% may occur for four-channel arrays, while large arrays, e.g. $N = 50$, exhibits much more stable outputs with fluctuation lower than 10% [36]. Also the fact that it excludes gain dynamics and deals with cold resonators cannot be overlooked. Finally, the latest model is laid out by Cao *et al* with Maxwell-Bloch equations, although as general as it could be [36], the complexity of including polarization fields is unnecessary for fiber lasers and it gives no meaningful results unless the full equations are solved, which the authors fail to do.

In summary, overall, there is no model comprehensive enough for studying coherent combining in passive fiber laser arrays and the lack of such good tools motivates us to develop a model on the basis of both multi-longitudinal modes and also laser dynamics. In the following sections, the novel and effective model is introduced and investigated in details.

2.3 Model equations

Figure 2.7 depicts two independent single mode fibers coupled discretely by a directional coupler. The continuous-wave pump beams are launched into each fiber by a wavelength division multiplexer (WDM) at $z = 0$ and excite active ions that give rise to gain at longer wavelengths. Assuming single polarization, the coherent waves generated in each amplifying fiber are governed by the nonlinear Schrödinger equation in conjunction with the rate equation for the population inversion [47]

$$\frac{\partial E_j}{\partial z} = \frac{1}{2}(g_j - \alpha)E_j - \beta_1 \frac{\partial E_j}{\partial t} + \frac{1}{2}(b - i\beta_2)\frac{\partial^2 E_j}{\partial t^2} + i\gamma \left|E_j\right|^2 E_j \qquad (2.5)$$

$$\frac{\partial \Delta N_j}{\partial t} = R_p(t) - \frac{\Delta N_j}{\tau} - \frac{\sigma \left|E_j\right|^2}{h\nu A_{eff}} \Delta N_j \qquad (2.6)$$

$E_j(z,t)$ and ΔN_j refer to the slowly varying envelope of the electric field and the population inversion in the first and second fiber for $j = 1,2$ respectively. From left to right, the terms in Eq. (2.5) account for the effects of linear gain $g_j(\Delta N_j)$, fiber losses α, the inverse of the group velocity β_1, the frequency-dependent losses b, the group velocity dispersion β_2, and lastly the nonresonant Kerr nonlinearity γ. As for gain dynamics in Eq. (2.6), $R_p(t)$ specifies the pumping rate. Its second and third terms describe the process of excited population relaxation with upper-state lifetime τ and laser gain saturation at high

intensity fields. The electric field amplitudes are normalized such that $|E_j|^2$ represents power distributions.

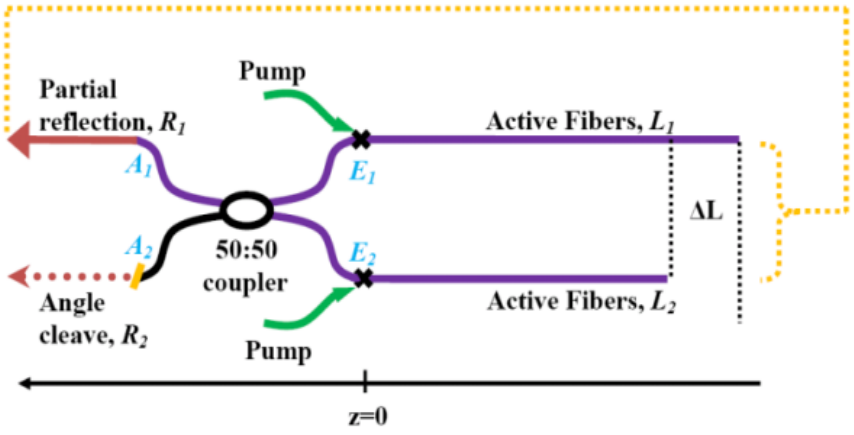

Figure 2.7: A two-channel fiber laser array in the unidirectional configuration.

Note that only forward propagating waves are considered in Figure 2.7. Because the reflectivity at the output port of fiber laser arrays is typically about 4%, the backward wave is always much weaker than the forward wave and hence standing wave effects as well as cross-saturation by backward waves can be neglected. The unidirectional model describes quite accurately the behavior of a ring fiber laser [47] and is expected to yield useful insight into the beam combining properties of fiber lasers under the high-output coupling condition. We note that unidirectional fiber laser arrays have also been demonstrated and their phase-locked operation is reported in Refs [48, 49].

The fields exiting the fibers at $z = 0$ pass through the 50:50 directional coupler, which connects the inputs E_1, E_2 and the outputs A_1, A_2 by the linear matrix

$$\begin{pmatrix} A_1 \\ A_2 \end{pmatrix} = \frac{1}{\sqrt{2}} \begin{pmatrix} 1 & -j \\ -j & 1 \end{pmatrix} \begin{pmatrix} E_1 \\ E_2 \end{pmatrix} \tag{2.7}$$

The field A_2 exits the cavity through the angle-cleaved end at the left while 4% of the power in A_1 is split equally and fed back to the fiber inputs at the right as indicated by the yellow dotted line in Figure 2.7. The remaining 96% serves as the output of that port.

2.4 Array simulation results: steady states

Before verifying the numerical scheme on a single fiber laser as described above, we make a further simplification of the rate equation. Typical roundtrip time for a fiber of tens of meters long is of order hundreds of nanoseconds, while the population relaxation constant is roughly ten milliseconds for Er-doped and one millisecond for Yb-doped fiber lasers. Another important time scale is the gain recovery time, which is also quite long and is of order milliseconds for Er-doped fibers [50-52]. The difference in time scales permits us to solve for the gain dynamics by setting the time derivative in the rate equation to zero. Assuming $P_{sat} = h\nu / \sigma\tau \times A_{eff}$, $g_j = 2\sigma\Delta N_j$ and $g_{0j} = 2\sigma R_p(t)\tau$, Eq. (2.6) becomes

$$g_j = \frac{g_{0j}}{(1 + \frac{\int_0^T |E_j|^2 dt}{TP_{sat}})} \tag{2.8}$$

where σ is the sum of absorption and emission cross sections and T is the computational time window. g_j becomes only position dependent (g_{0j} is a constant). Note since the electric field, which appears in Eq. (2.8), varies rapidly in time compared to the slow gain dynamics, we average it over the computational time window T. Eqs. (2.5) and (2.8) are integrated numerically and iteratively together with the coupling matrix to model the laser behavior of this composite cavity. In this thesis, we adopt standard split-step Fourier methods (SSFM), which has been used extensively for studying nonlinear pulse propagation in fibers, to handle the multi-longitudinal-mode nature of continuous-wave

fiber lasers. SSFM is a numerical algorithm for solving nonlinear partial differential equations, where the linear and the nonlinear terms are treated separately in the spectral and temporal domains. With the help of fast Fourier transformation (FFT), the complex field variable can be transformed back and forth between two domains rapidly and makes it an efficient computation method. See appendix for more details of SSFM.

2.4.1 **Benchmark for single fiber laser**

A single 24 m long unidirectional Er-doped fiber laser with 4% power feedback is simulated for the purpose of benchmarking. Table 2-1 lists the parameters and their corresponding values as taken from Ref. [47]. The contribution of spontaneous emission is represented by small, uniformly distributed complex numbers on the order of 10^{-14}, which are generated randomly for each spectral component and incorporated into each roundtrip for initiating the lasing process. The order of magnitude of these numbers is chosen such that when the laser is pumped below threshold, its output powers are smaller than femtowatt. To ensure the randomness of these noise sources, both signs of the real and imaginary parts of the field are also assigned stochastically to be positive or negative. Figure 2.8 shows the steady state output power distributions in both temporal (left) and spectral (right) domains for two cases: (a) with a Kerr nonlinearity $\gamma = 0.003$ W^1m^{-1} and (b) with $\gamma = 0$ W^1m^{-1}. The power spectra are computed by taking the absolute square of the Fourier transformation of the time domain fields. The time window T is chosen to be eight times the roundtrip duration to ensure dense discretization and higher resolution in the frequency domain. An average of approximately 28 mW power is obtained by $\int_0^T \left|E_j\right|^2 dt / T$ for either case. Because the large output coupling coefficient leads to significant amplitude changes along the fiber, the step size parameter of SSFM needs to

remain small in order to obtain accurate integrations. Here we choose six or more steps for each roundtrip. Growing out of incoherent random noise, the laser output is characterized by a time-varying output and its spectrum consists of irregular spikes. The irregular time series is the result of the complex beating between a large numbers of longitudinal modes with random phases. The steady states are therefore defined by measuring the average powers between consecutive roundtrips. The shape of the spectral envelope is determined by the loss dispersion. It is evident that the inclusion of the nonlinear refractive index broadens the power spectrum significantly, which was first verified and reported by *Roy et al* for fiber lasers [47]. This is a result of four-wave-mixing which can be approximately phase-matched because of the dense nature of the longitudinal modes. It is clear that this propagation model should be capable of describing the spectral properties of fiber laser arrays with multiple longitudinal modes.

Table 2-1: simulation parameters and values

Parameters	Description	Value
λ	wavelength	1.545 μm
n	refractive index	1.5
α	propagation loss	0.058 m^{-1}
g_0	unsaturated gain	2.67 m^{-1}
b	loss dispersion	0.13 ps^2/m
β_2	phase dispersion	-0.003 ps^2/m
τ	population relaxation time	10 ms
γ	nonlinear coefficient	0.003 $W^{-1}m^{-1}$

P_{sat}	saturation power	0.6 mW
RT	roundtrip number	2000
rtsteps	step number of one roundtrip	6

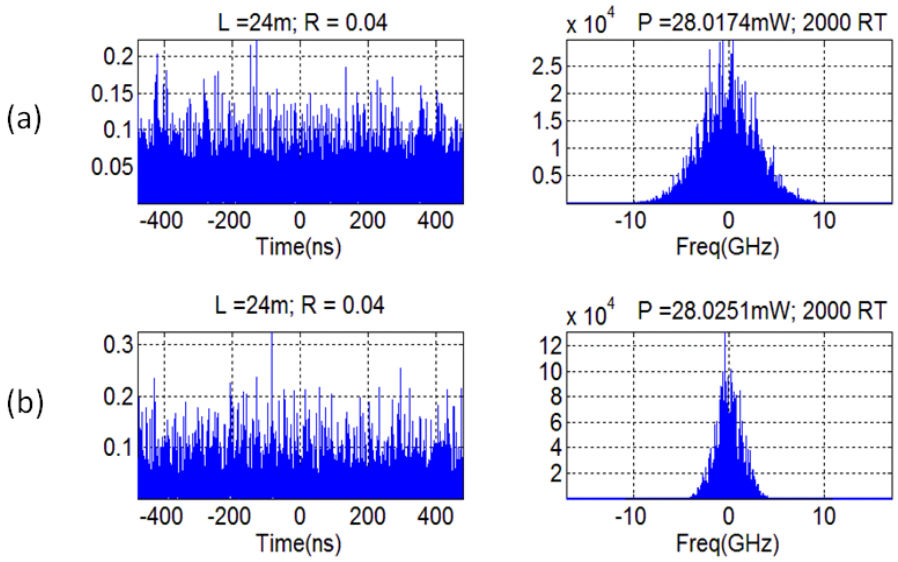

Figure 2.8: Output powers of single Er-doped fiber laser in the time (left) and spectral (right) domains for (a) γ = 0.003 $m^{-1}W^{-1}$ and (b) γ = 0 $m^{-1}W^{-1}$. The power reflectivity is 4% as indicated in the figure.

2.4.2 **Two fiber laser beam combining**

We begin with a two-channel fiber laser array by setting L_2 to 24.0 m and R_1, R_2 to 4%, and 0% respectively in Figure 2.7. The length difference ΔL is arbitrarily selected to be 30 cm and hence L_1 equals 24.3 m. Using parameters from Table 2-1, Figure 2.9 illustrates the simulation results for both temporal (left) and spectral (right) domains. It is interesting to see that essentially all the power, 56.26 mW, emerges from the first output port while very little (less than 0.05 mW) escapes from the other, angle-cleaved, one. (Note the orders-of-magnitude difference in the ordinate scales between Figure 2.9(a) and (b).) For the efficiency calculations, a simulation of individual fiber lasers of lengths L_1,

L_2 and equal 4% output coupling generated P_1 = 28.27, P_2 = 28.02 mW respectively. Their sum gives a total power of 56.29 mW and it is used, together with the array output power $P_{out,array}$ 56.26 mW, to define the combining efficiency $P_{out,array}/(P_1+P_2)$ in this paper. Here, the efficiency is high and close to 100%.

A rather striking feature of the array output is the discrete nature of the power spectra compared to the quasi-continuous spectrum displayed by the single fiber laser. While the spectrum of the single laser is made up of the densely packed axial modes of a long cavity, the array resonances in Figure 2.9 comprise a set of spikes equally separated by an interval of 0.667 GHz. This spectrum is the result of a Vernier effect involving the superposition of the frequency combs of the two coupled cavities with a length mismatch ΔL as illustrated in Figure 2.10.

For ring cavities it leads to a modulation of the comb spectrum with a beat frequency of $\Delta v = c/n/\Delta L$. Using a refractive index of n = 1.5 and 0.3 m for ΔL, we obtain 0.667 GHz which agrees exactly with the simulation result. For laser arrays with standing wave cavities, the optical path lengths double, so the mode separation becomes $\Delta v = c/2n/\Delta L$ [20]. The Vernier effect results in the suppression of certain longitudinal modes and has been utilized in the Vernier-Michelson cavity to achieve single-frequency operation for gas lasers [53].

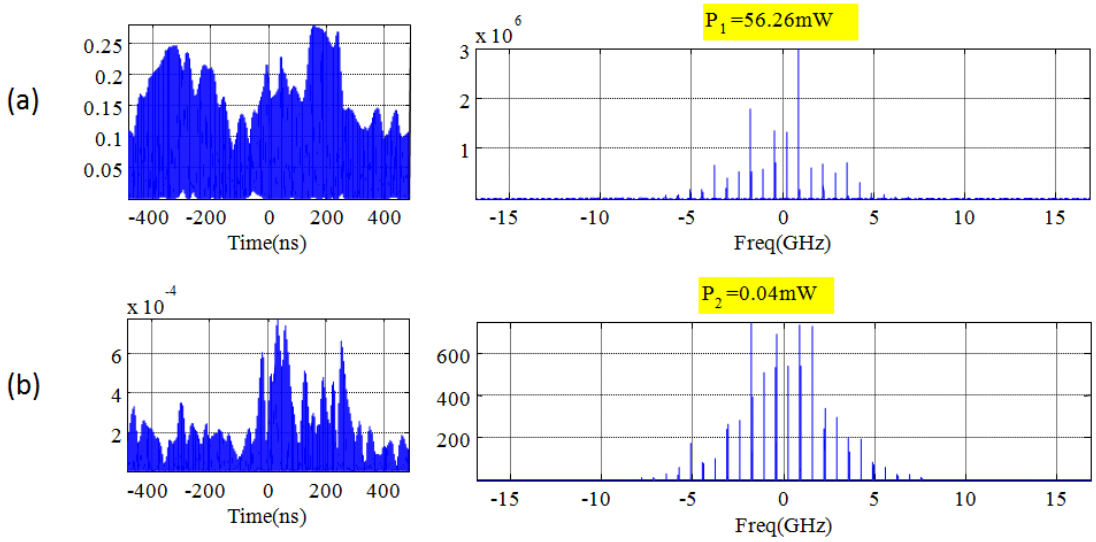

Figure 2.9: A unidirectional Er-doped fiber laser array with L_1 = 24.3 and L_2 = 24.0 m in Figure 2.7. The output powers from (a) upper port with partial reflectivity and (b) lower, angle-cleaved, port. The separation between spikes is measured to be 0.667 GHz.

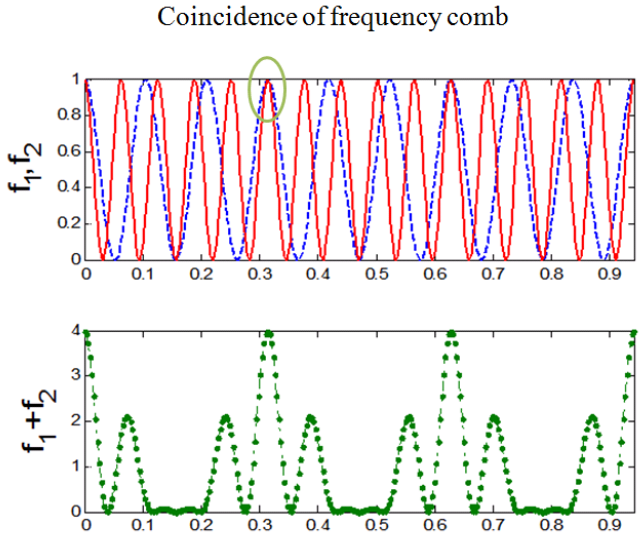

Figure 2.10: Illustration of Vernier effects. The upper plot shows two sets of individual periodic frequency combs and the lower one plots their superposition.

To further demonstrate the natural emergence of the array modes and the self-adjustment feature of our model regardless of the length differences, another simulation

result is given with all the coefficients fixed as before except that L_1 is changed to 24.08 m, so that ΔL = 8 cm. Since Δv is inversely proportional to ΔL, greater spacing is expected for a smaller length mismatch. Indeed the spectral intervals are measured to be 2.5 GHz in Figure 2.11(a) and (b), which is consistent with the theoretical calculations. Note also that the main peak in the spectrum has shifted from 0.9074 GHz in Figure 2.8(a) to -0.1848 GHz in Figure 2.11(a) as the laser self-adjusts its frequency. This dependence of the beat spectrum on ΔL is routinely seen in experiments [3-6, 16, 20]. Further details of the spectrum can be seen by zooming in on one of the spikes in Figure 2.9(a) (circled in green). It is seen that the spikes are actually the envelope of the individual cavity axial modes, which are equally spaced in the absence of the Kerr nonlinearity (Figure 2.11(c), γ = 0 $W^{-1}m^{-1}$) and somewhat broadened and shifted in the presence of nonlinearity (Figure 2.11(d), γ= 0.003 $W^{-1}m^{-1}$). The shift of the peak due to nonlinearity is only about 1 MHz at these power levels. We remark that some frequency pulling of the individual modes has been observed in experiments and attributed to nonlinearity [13]. Based on those results the authors suggested that the mechanism for spontaneous self-organization without cavity length control is a nonlinear process (in the sense of requiring an intensity-dependent refractive index). Our results however indicate that this spontaneous self-adjustment occurs even in the absence of nonlinearity as the laser seeks to operate on the lowest loss mode of the composite cavity. The presence of nonlinearity simply leads to a slight modification of the actual mode frequencies but cannot be seen as the fundamental mechanism leading to the coherent phasing of the two amplifying fibers.

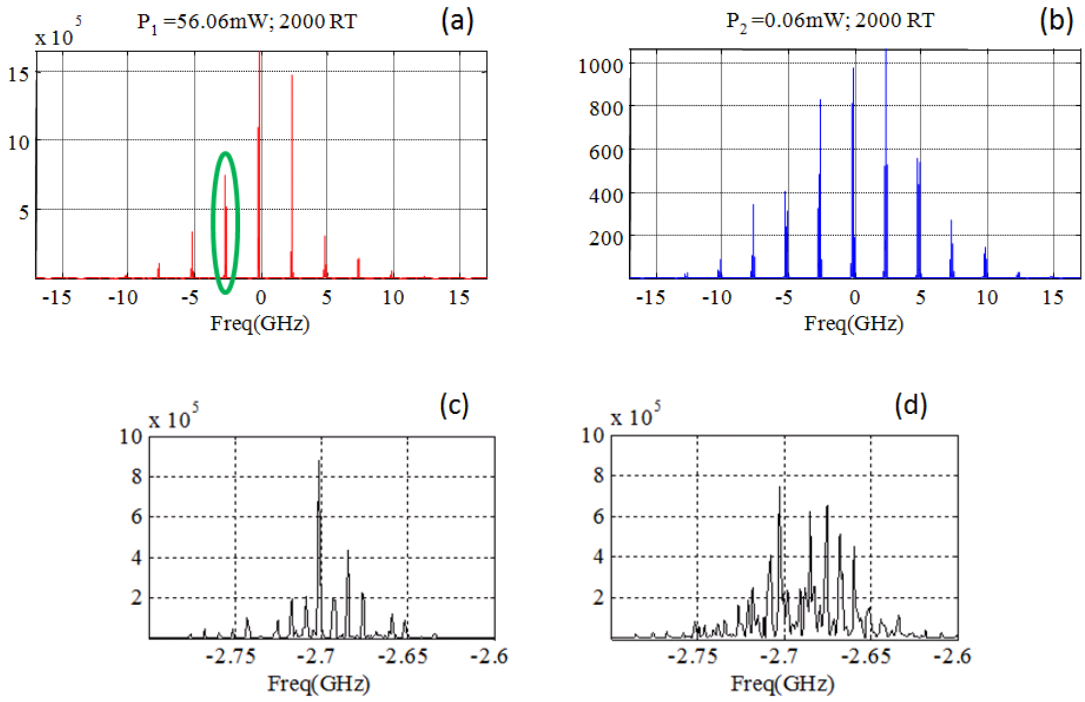

Figure 2.11: Power spectrum of a two-channel fiber laser array with L_1 = 24.08 m and L_2 = 24.0 m. P_1 in (a) refers to the output power from the port of 4% reflectivity, and P_2 in (b) is from the angle-cleaved one. The spikes are separated by 2.5 GHz. The spectrum of the green-circled spike of (a) is further zoomed in for (c) linear and (d) nonlinear arrays. The results of (a),(b) are simulated for nonlinear arrays, but its combining efficiency is the same as that of linear ones.

The ability of two lasers to combine efficiently regardless of their length difference is a feature that emerges naturally from our model. It is merely a reflection of the fact that in the presence of a large number of longitudinal modes, the fields self adjust to select a new oscillation that corresponds to a common resonance of the combined cavity [2]. This self-adjustment should be possible so long as there is sufficient bandwidth available to encompass at least one of these composite-cavity modes. In our model, the effect of bandwidth-limiting elements in the cavity is described by the parameter b. It represents a frequency-dependent quadratic loss term of the form $-b(\omega-\omega_0)^2$. To investigate the role of available bandwidth in beam-combining efficiency we consider a

case where ΔL is small enough that the frequency spans are greater than the limited bandwidth imposed by a filter. First we assume 1 mm for ΔL and set the loss dispersion coefficient to zero. The simulation results are illustrated in Figure 2.12(a). Note the modulation period is calculated to be 200 GHz. In the absence of bandwidth limiting the fiber lasers combine successfully with efficiency close to 100%. The first two peaks near the center, pointed out with arrows in Figure 2.12(a), are measured to be -117.9 GHz (left) and 82.02 GHz (right), the main peak. Again 200 GHz is verified by subtracting -117.9 from 82.02. Next the simulation is repeated with $b = 0.13$ ps^2m^{-1} and it corresponds to a filter with a bandwidth of roughly 60 GHz, which is calculated by evaluating the amount of parabolic losses $b\Delta\omega^2$ to be on the order of the linear losses of 0.1 m^{-1}. Since now higher frequencies experience more losses, only one peak with the least attenuation lases in Figure 2.12(c) and the sum of P_1 and P_2 is also reduced. The combining efficiency decreases to 76% since there is now only a single mode within the gain bandwidth.

Note that the location of the main peak is now measured to be 55.87 GHz as opposed to 82.02 GHz in Figure 2.12(b) without bandwidth limiting. In addition, a significant amount of power, 8.6 mW, appears at the lossy port. The occurrence of the frequency shift and the large output from the angle-cleaved port implies that the array, in the presence of frequency-dependent losses, does not necessarily lase at the cold cavity composite resonances but at frequencies that minimize the overall cavity losses. It shows that the model, just like actual fiber laser arrays, does adjust itself and select the suitable resonant frequencies.

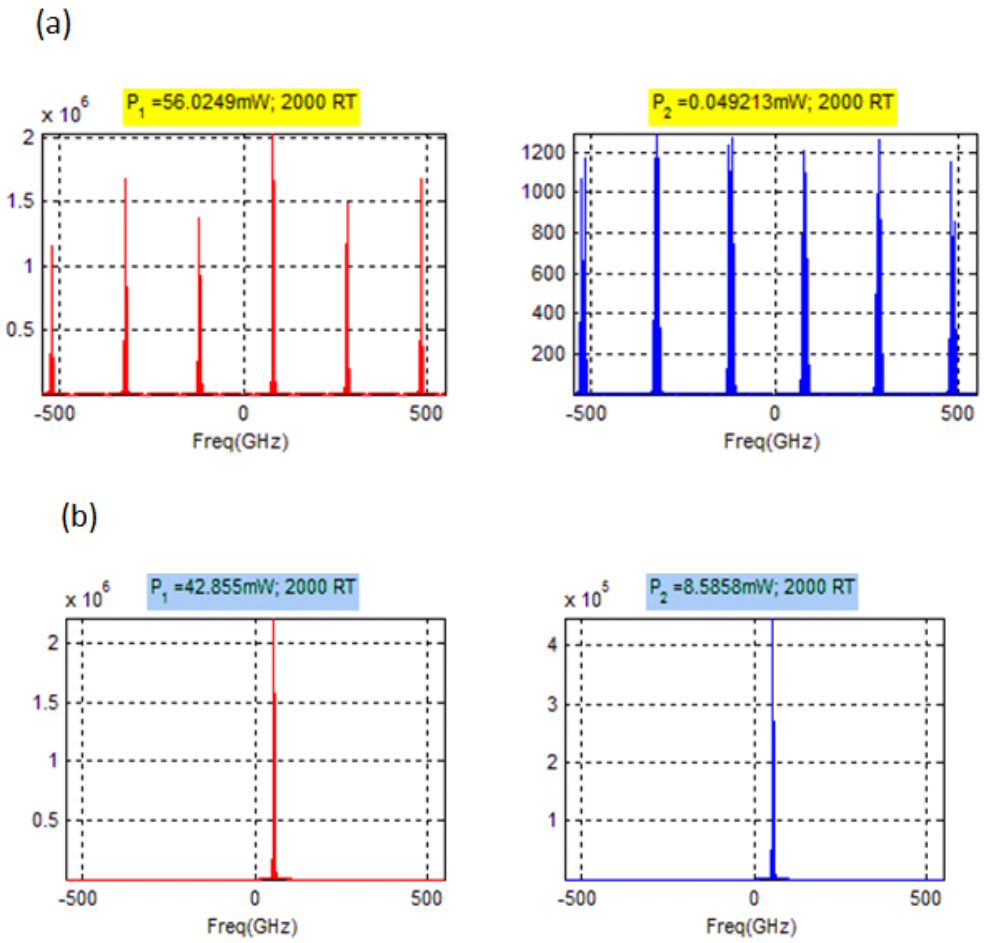

Figure 2.12: Er-doped fiber laser arrays configured in Figure 2.7 with L_1 = 24.001 and L_2 = 24.0 m. The computation window in frequency domain covers more than 1 THz. The left plots refer to the output powers from the port with partial reflectivity, while the right ones show the other, angle-cleaved, one. No frequency-dependent losses are applied for (a) and b equals 0.13 ps^2m^{-1} in (b).

In the extreme case of identical fiber lengths in a two-channel laser array, successful coherent combining is not possible since the modulation period becomes infinite with ΔL = 0. The simulation results in Figure 2.13 confirm this argument.

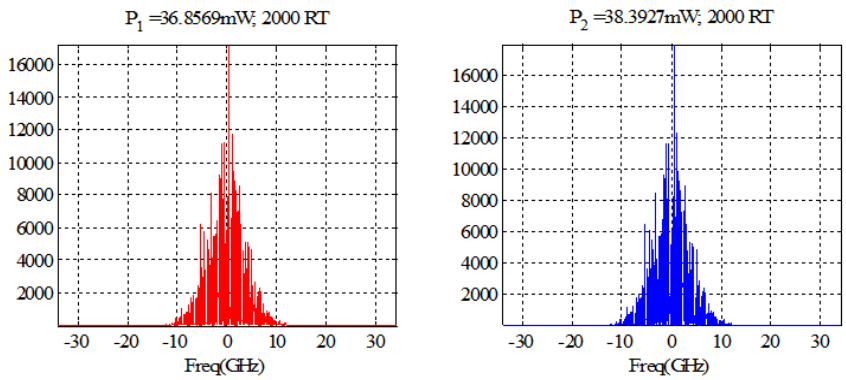

Figure 2.13: Simulation results for a two-channel fiber laser array with identical fiber lengths. Refer other simulation parameters to Figure 2.12(b): b = 0.13 ps^2m^{-1}, γ = 0.003 $W^{-1}m^{-1}$.

The final example given for two-channel fiber laser arrays is to examine the fine structure of the spectrum of amplified spontaneous emission for operation below threshold. Using realistic parameters from the experiment of Shirakawa, et al [34], the simulation results are illustrated in Figure 2.14(a) with 12.682, 12.0 m for L_1 and L_2 respectively. Note that we double the fiber lengths since our model is based on the ring cavity configuration. The carrier wavelength is kept at 1.545 μm and the refractive index n is 1.45. The lasing threshold $g_{th} = \alpha - \ln(R_1)/L$ is calculated to be 0.312 m^{-1}. We set g_0 to 0.31 m^{-1} and the amplified spontaneous emissions spectrum from the first port agrees qualitatively with that of the experimental results [34] shown in Figure 2.14(b). As in the experiment, the spectral packets are separated by about 302 MHz. Unlike the very narrow spectral packets (essentially spikes) in the previous plots where arrays are pumped above the threshold, they exhibit broader FWHMs here and are seen clearly to comprise small spikes separated by a free spectral range of 16.3 MHz. As for the second port, its spectrum is more complicated and features a split pattern around the peaks of the resonances. The spectra at the two ports are complementary in a manner similar to the

reflection and transmission spectra of a Fabry-Perot. (For the second port the experimental spectrum of Ref. [3] has some similarities to the theoretical one but is complicated by the presence of features attributed to the presence of an extraneous polarization component.) As the pump power increases the spectral packets are seen to narrow as shown in Figure 2.14(c). This is a result of gain narrowing due to our assumption of homogeneous broadening in which most longitudinal modes are suppressed as a result of serious competition between adjacent frequencies.

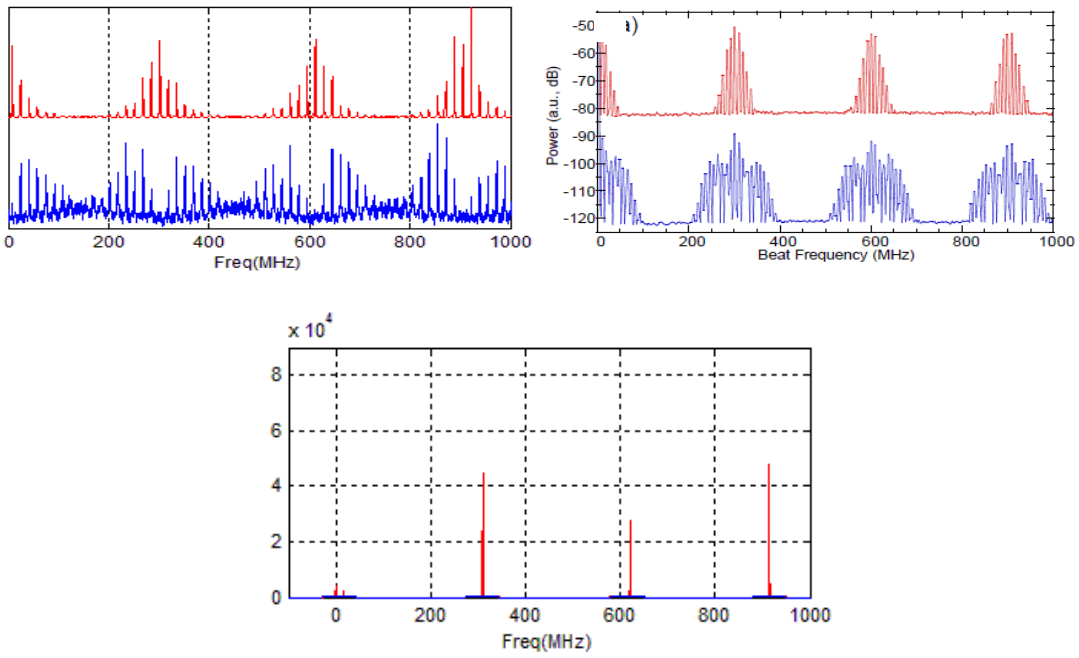

Figure 2.14: Beat spectra of amplified spontaneous emission for the higher reflectivity port (red curves) and the zero-reflectivity port (blue curves) an Er-doped fiber laser array with round-trip path length difference of 0.682 m. (a) Simulation result obtained by averaging the spectrum over 500 consecutive roundtrips (b) Experimental beat spectrum measurement from Ref. [34], used with permission. (c) Simulation of spectrum above threshold.

2.4.3 **Two fiber lasers beam combining: constant spontaneous emission**

As mentioned in Sec. 2.4.1, the lasing process is normally initiated with complex random numbers which represent the noisy spontaneous emissions in the active materials.

The amplified radiations of such quasi-continuous-waves usually feature a rapidly-changing phase relation between its multilongitudinal modes since in practice no apparent mechanism exists to regulate their ordering. In this case, the arrays growing from coherent seed waves are particularly interesting for it provides us additional perspectives in understanding the fiber laser array structures.

Adopting the same parameters and values as in Figure 2.11, the array simulation is carried out with artificial spontaneous emission as a small, fixed amplitude injected repeatedly into the cavity. Figure 2.15 shows the results for temporal and spectral domains when γ is set to 0 $W^{-1}m^{-1}$. Note the time domain outputs (Figure 2.15(a) and (b)) consist of complementary waveforms and both appear as periodic pulse trains, directly implying appearance of the mode-locked operation. Since their power spectrum looks qualitatively the same at zoom-out, only one, the upper-channel, is shown here (Figure 2.15(c).) The details of the green-circled peak are also magnified in Figure 2.15(d) illustrating band-pass and band-stop filtering effects of the structure. It is worth mentioning that sinusoidal waves and the corresponding Fourier transformations match up Figure 2.15(a) and (c) very well. This connection, suggesting again the phase-locked states of the array modes, could be readily understood based on the fact that the resonator is driven by a constant excitation. At last, the relative phase between two incident waves is also examined before they enter the coupler so as to fully understand the combining mechanism of individual fiber lasers. Because phase information only matters when it comes with significant amplitudes, $\Delta\phi$, defined as modulus of (ϕ_1 - ϕ_2) by 2π, is plotted, following Figure 2.15(d), over a small frequency range. The phase spectrum displays a straight line in Figure 2.15(e) due to our early assumption of linear cavities, i.e. $\Delta\phi$ is

linearly proportional to the frequency. The line is observed to cross $\Delta\phi$ at 1.5π for this particular phase difference leads to constructive interferences in the upper, partially reflected, output port. A simple calculation with an input field of equal amplitudes and a relative phase difference of 1.5π confirms such result as seen in Eq. (2.9).

$$\frac{1}{\sqrt{2}}\begin{pmatrix} 1 & -j \\ -j & 1 \end{pmatrix}\begin{pmatrix} -j \\ 1 \end{pmatrix}=\begin{pmatrix} -\sqrt{2}j \\ 0 \end{pmatrix} \tag{2.9}$$

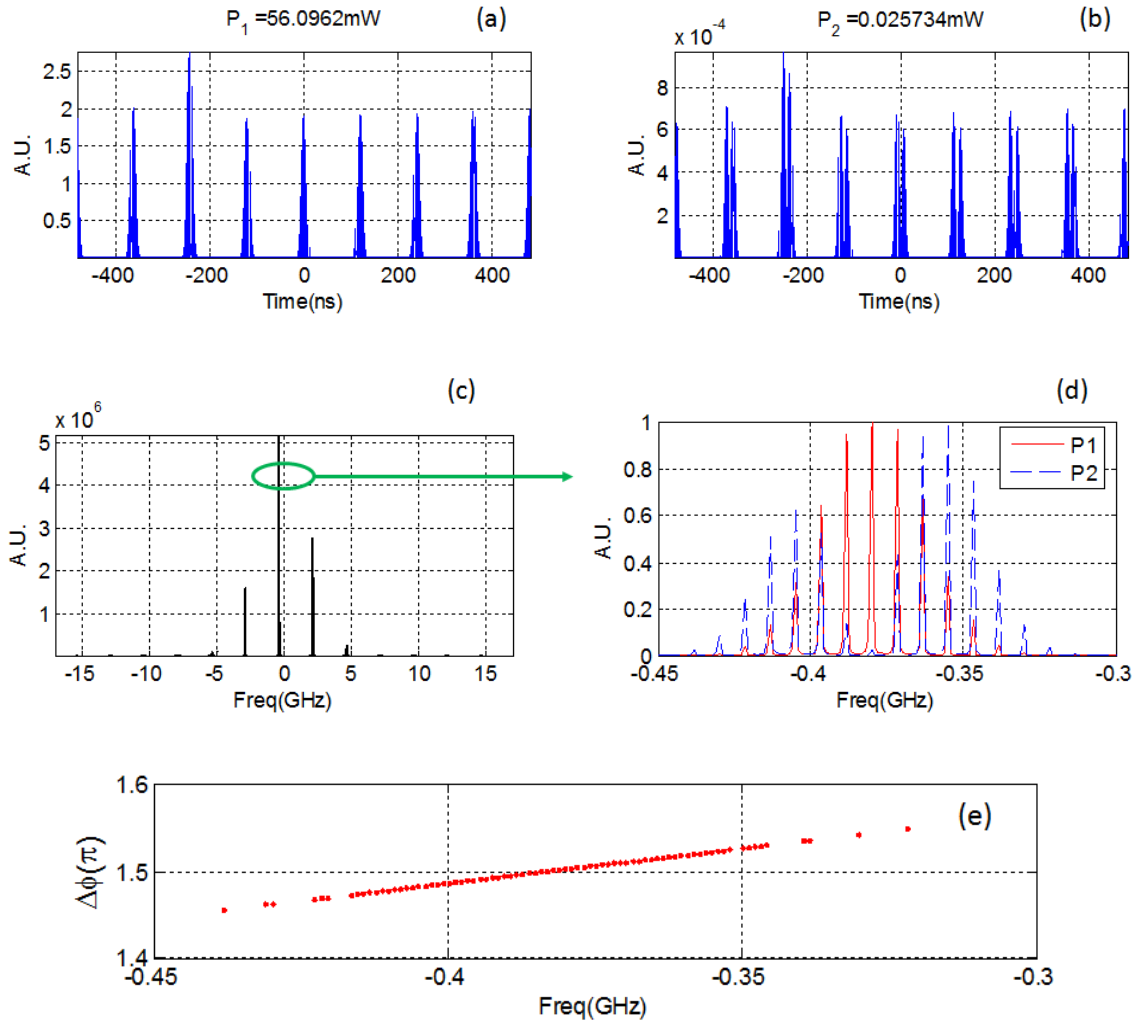

Figure 2.15: A two-channel fiber laser array configured as Figure 2.7 is simulated with artificial spontaneous emission (constant seeds). Assuming $\gamma = 0$ $W^{-1}m^{-1}$, two fiber lengths of 24.08 m and 24.0 m are used. Plots (a) and (b) show the time domain output powers from upper, partially reflected, and lower, angle-cleaved, port respectively. The overall power spectrum from main outlet (c) looks

qualitatively the same to the other one except for its large magnitudes. The spectrum details of green-circled region are further shown in (d). The phase spectrum in (e) shows the phase-locking of two lasers at $\Delta\phi = 1.5\pi$.

2.4.4 **Effects of nonlinearity**

Next we are interested in studying the fiber laser arrays in the presence of small electronic nonlinearity. The possibility that the nonlinear phase is beneficial for array combining or phase locking processes remains controversial. Some groups have claimed finding support for the enforcement of self locking through nonresonant n_2 [54-56], while at the same time opposing evidence is demonstrated experimentally with high power, > 50W, fiber laser arrays [23, 56]. In between, even neutral points of views are proposed toward nonlinearity [57]. Therefore, this confusing state of affairs must be clarified if anyone is trying to fully explain the combining mechanism. In this section, we are devoted to elucidate the role of nonlinear phases in coherent combining.

Using nominal n_2 of fused silica, $\gamma = 2\pi n_2 / \lambda / A_{eff}$ is calculated to be 0.003 $W^{-1}m^{-1}$ for a wavelength 1.545 μm and an effective mode area 43 μm^2. We repeat the simulation of Sec. 2.4.3 with γ turned on. In theory the Kerr nonlinearity makes contribution through the time domain intensities that $\Delta\phi_{NL} = \gamma |E(t)|^2 L,$ thus the phase spectrum is expected to deviate from straight lines because of self-phase modulation. The results, however, show that the nonlinear index n_2 has no observable effect at this power level. Specifically, there is no apparent difference between the nonlinear phase plot Figure 2.16 and Figure 2.15(e), moreover, the combining efficiency stays the same, close to 100%. This outcome is not surprising since the self-phase modulation is usually discussed in the context of picosecond pulses when the peak intensity is high [3] , yet here we deal with quasi-continuous waves of longer than hundreds of nanoseconds.

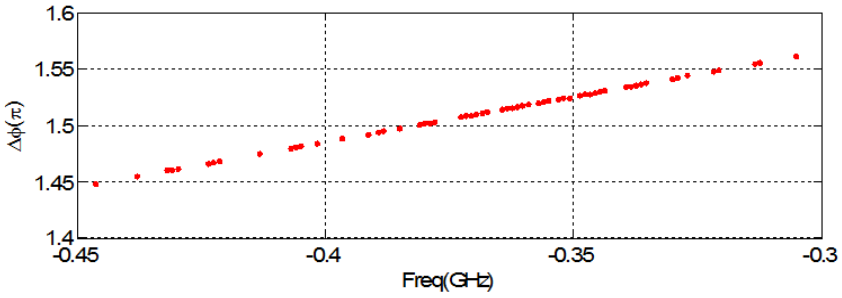

Figure 2.16: The phase spectrum with small nonlinearity $\gamma = 0.003$ $W^{-1}m^{-1}$.

In the attempt to recognize the effects of the nonlinearities, we raise γ by more than two orders of magnitudes and force the mechanism to come to play at current power level. Assuming γ equal to 0.9 $W^{-1}m^{-1}$, the simulation is repeated without changing the other parameters. Several apparent differences can be observed if we make one-on-one comparison between the linear and the nonlinear cases. Firstly, Figure 2.17(a), (b) exhibit dense irregular temporal pulsations as opposed to the clean periodic patterns in Figure 2.15(a) and (b). Secondly, not only does the power spectrum spread much (over ±30 GHz versus less than ±5 GHz for Figure 2.17(c),(d) and Figure 2.15(c),(d) respectively,) but the FWHMs of each spectral packet also broaden considerably. In the third, the previous straight-line of Figure 2.15(e), as predicted, now appears crooked and comprises of randomly scattered data in Figure 2.17(e) because of the nonlinear perturbations. In addition, the relative phase $\Delta\phi$ expands its distribution range from ±0.1π in Figure 2.15(e) to ±0.5π in Figure 2.17(e). Eventually, the combining efficiencies are calculated for both arrays and they differ appreciably by 30% (100% for linear and 70% for nonlinear.)

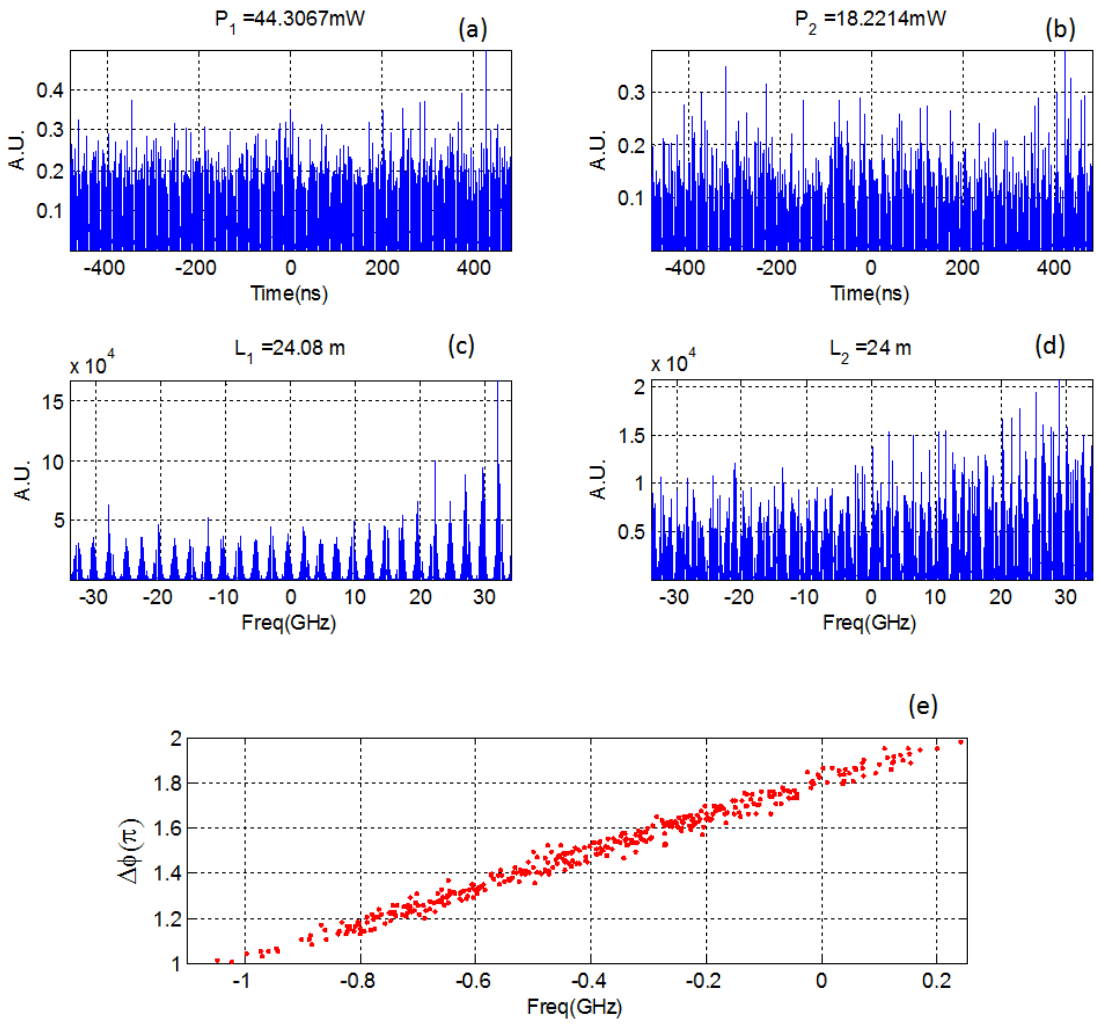

Figure 2.17: As a comparison to Figure 2.15, the two-channel fiber laser array is simulated with $\gamma = 0.9$ $W^{-1}m^{-1}$. The outputs in the temporal and spectral domains are shown in (a),(b) and (c),(d) respectively. The phase spectrum is displayed in (e).

The decreases of the combining efficiencies can be related to the nonlinear directional couplers [58] and ultrafast all-optical switching [59, 60], where short pulses are controlled and switched between output ports depending on their peak powers. To further account for the results in Figure 2.17(a), we calculated the output powers with Eq. (2.7) assuming equal amplitudes of the incident waves before the coupler. Their power ratio is expressed as a function of their phase difference by

$$\frac{P_1}{P_2} = \frac{1-\sin(\Delta\phi)}{1+\sin(\Delta\phi)} \tag{2.10}$$

The logarithmic scale of Eq. (2.10) is also plotted in Figure 2.18 for it gives a better visualization as for how rapidly the powers transfer between one port to the other when $\Delta\phi$ changes. It is clear that the singularities occur at 1.5π and 0.5π representing the two extremes of the power combining. Observe when $\Delta\phi$ is confined within 1.45π and 1.55π (in the case of the linear arrays), the power ratio is high and most powers reside in P_1. On the other hand, when $\Delta\phi$ deviates far from 1.5π and approaches π or 2π, P_1 decreases and more powers emerge out of the lower, angle-cleaved port as is evident in Figure 2.17(a). It thus, by Figure 2.18, explains the drops of the combining efficiency quite well that even though nonlinearity induces some randomized perturbations to the linear phases, the efficiency decreases mostly due to the increasing bandwidth of the power spectrum, in particular the broadening of each spectral packet under modulation.

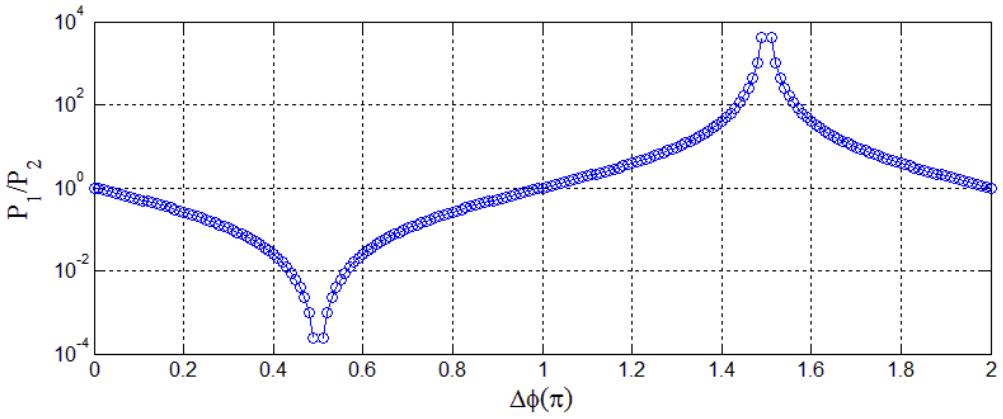

Figure 2.18: The logarithmic plot of the output power ratio in terms of relative phase $\Delta\phi$.

2.4.5 **Four fiber lasers beam combining**

To further demonstrate the capacity of this model, we apply the simulation to a four-channel fiber laser array with randomly chosen lengths of 24.0, 24.3, 23.73, and 24.63

meters. The results are shown in Figure 2.19. Unlike two-channel arrays where Δv is determined by the length differences, it is now determined by the greatest common divisor L_{gcd} of the four lengths [61]. In this case, L_{gcd} equals 3 cm and indeed the amplified spontaneous emission spectrum (Figure 2.19(a)) features a complicated interference pattern with a period of 6.67 GHz calculated from $\Delta v = c / n / L_{gcd}$ using 1.5 for the refractive index n. As the pumping is increased above threshold there is a narrowing of the beat packets. Each spike of the power spectrum in Figure 2.19(b) corresponds to the peak of the beat packets in Figure 2.19(a) and the red arrows in both figures indicate at -7.826 GHz. Most of the power, 107.44 mW, emerges from the second output port as seen in Figure 2.19(b). Since the four uncoupled fiber lasers produce a total of 112.63 mW, the combining efficiency is calculated to be 95.4%.

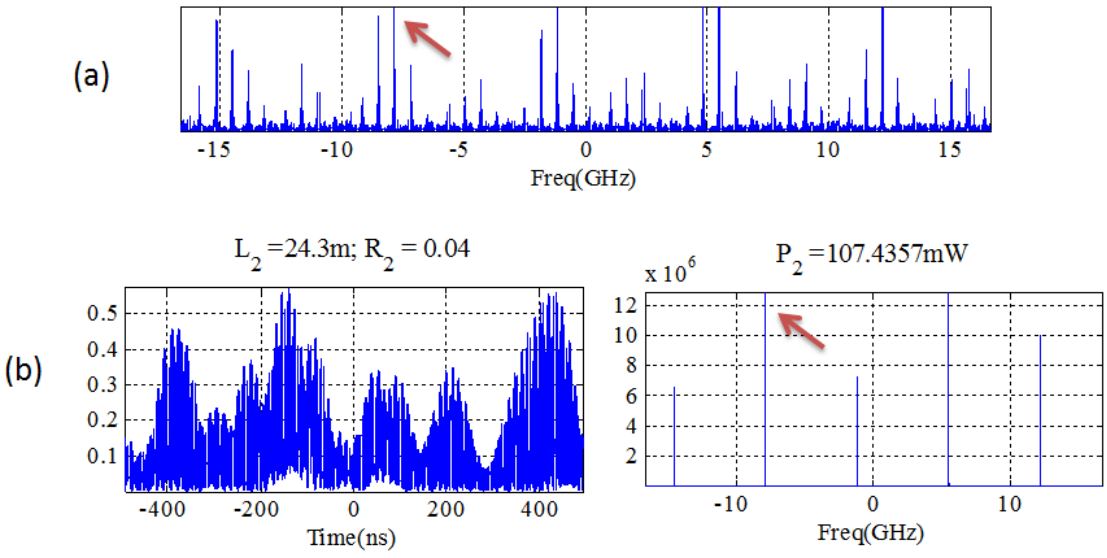

Figure 2.19: Four-channel fiber laser arrays (a) spectrum of amplified spontaneous emissions with pattern periods measured to be 6.67 GHz. (b) Major output powers in the temporal (left) and spectral (right) domains. The peaks pointed by both red arrows are measured to be -7.826 GHz.

The reason for the efficiency drop is the decrease in the probability of finding an accidental coincidence in the resonances of mismatched cavities as the number of such cavities increases [7-10]. The system, however, in a slightly different manner as proposed by Refs. [7-10], still finds the least lossy mode when the exact coincidence, which corresponds to the lossless array mode, is absent. When this happens, a significant portion of energy will generally couple out through the lossy, non-reflected, ports because of the residual phase mismatch at the couplers. It appears to us that combining N fiber lasers is analogous to solving a system of N-1 (linear or nonlinear) algebraic equations as laid out explicitly in the next paragraph. Increasing the array elements simply imposes more criteria (equations) to the system while the number of unknowns is kept fixed. In practice, there is only one unknown and it refers to the coincidental lasing frequency. For linear cavities, N equal to two is a special case that one variable and one linear equation guarantee the existence of exact solutions. For larger arrays, however, equations outnumber unknowns and they become over-determined systems that only approximate or optimal solutions could be obtained under general conditions. In the data analysis, one common technique to solve such problem is the least squares (LS) method in which the sum of squared distance between the given data and the modeled ones is minimized (pictured in Figure 2.20 [wiki].) Interestingly, our model, without needing any deliberate manipulations, shares the same working principle as the LS method and solves the coupled array by finding the mode with minimum overall losses.

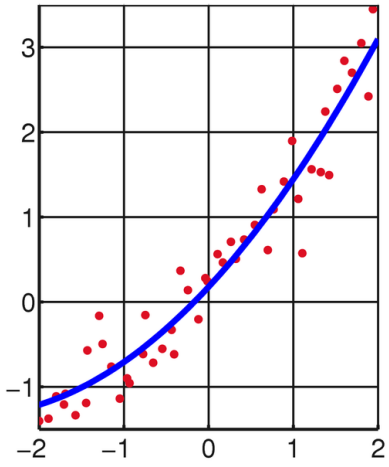

Figure 2.20: the least squares method for approximately solving the over-determined systems. [wiki: http://en.wikipedia.org/wiki/Least_squares]

To prove the point of the array lasing at the minimum losses, we derive the loss formulation for a simple two-channel fiber laser array as seen in Figure 2.7. Assuming the circulating power within each fiber laser just before the coupler is P, the coupler output powers, according to Eq. (2.10), are $P(1+\sin(\Delta\phi))$ and $P(1-\sin(\Delta\phi))$ when the lasing frequency has an accumulated phase difference of $\Delta\phi = \omega/c\, n_1(L_1 - L_2)$. Only one of the output powers is reflected and being feedback into the other end of the two fibers. Take $P(1+\sin(\Delta\phi))$ for example; the steady-state laser oscillation requires the power at the reference plane restored to P just before the coupler, so we can write

$$P(1+\sin(\Delta\phi))\times \mathrm{R}\times\frac{1}{2}\exp[(g-\alpha-b\omega^2)L] = P \tag{2.11}$$

where R is the power reflectivity, g is the saturated gain, α is the linear loss and b is the loss dispersion coefficient. We take the logarithm of Eq. (2.11) and it gives the loss formulation as the right hand side of Eq. (2.12).

$$g = \alpha + b\omega^2 - \frac{\log(R(1+\sin(\Delta\phi))/2)}{L} \tag{2.12}$$

The frequency dependent loss thus can be easily plotted by plugging in $\Delta\phi = \omega/c\, n_1(L_1 - L_2)$.

Consider an example of a two-channel fiber laser array of lengths 24.0005 m and 24.0 m, its simulated power spectra are shown in Figure 2.21 for (a) b = 0 ps^2m^{-1} and (b) b = 0.13 ps^2m^{-1} respectively. It is clear the combining efficiency drops considerably and the lasing frequency shifts from 126.5 GHz to 45.79 GHz with the presence of the loss dispersion. Their loss profiles can then be readily plotted utilizing Eq. (2.12) and are shown in Figure 2.22. In the case of zero b coefficient, the loss is seen to be minimum near -300 GHz and near 100 GHz corresponding the lasing peaks in Figure 2.21(a). Similarly, a loss dip is observed between 0 and 100 GHz in Figure 2.22(b) and is in consistent with Figure 2.21(b). For better visualization, the minimum losses are replotted in logarithm scale in Figure 2.23 and are overlapped with the lasing frequencies in Figure 2.24 with good agreement with each other. Therefore, by calculating the frequency dependent losses, we proved that our model solves the coupled array by finding the mode with minimum overall losses.

(a)

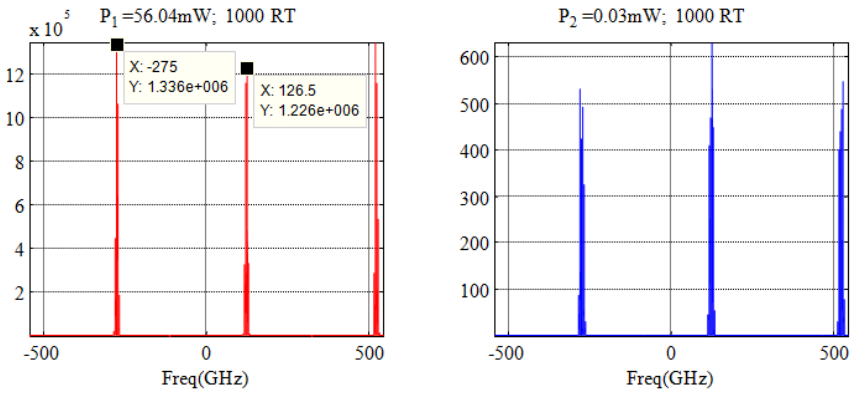

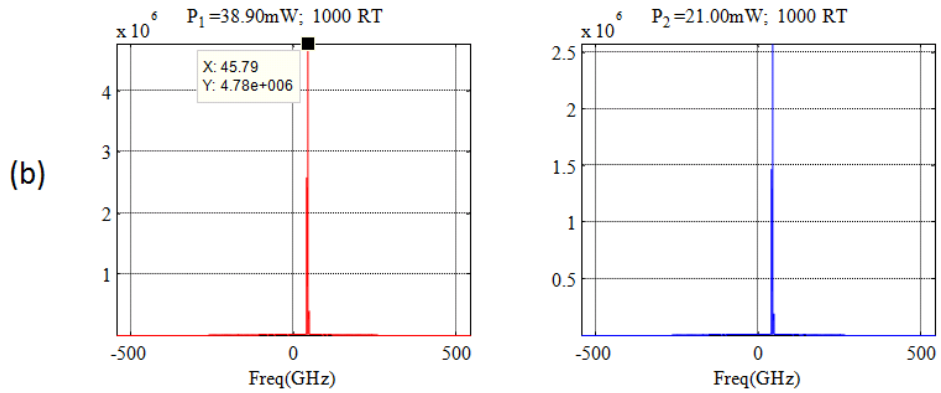

Figure 2.21: Power spectra of a two channel fiber laser array with fiber lengths 24.0005m and 24.0m for (a) $b = 0$ ps^{2}m^{-1} and (b) $b = 0.13$ ps^{2}m^{-1}.

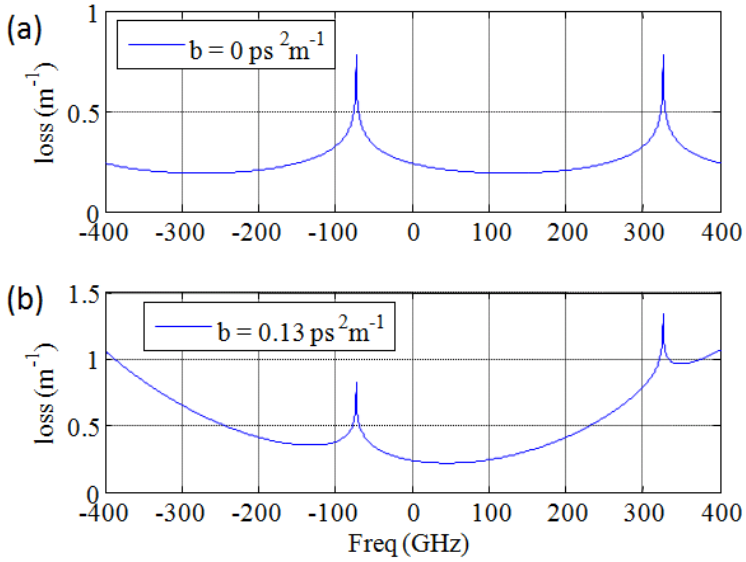

Figure 2.22: The frequency dependent loss (m^{-1}) of Figure 2.21 for (a) zero and (b) nonzero b coefficients.

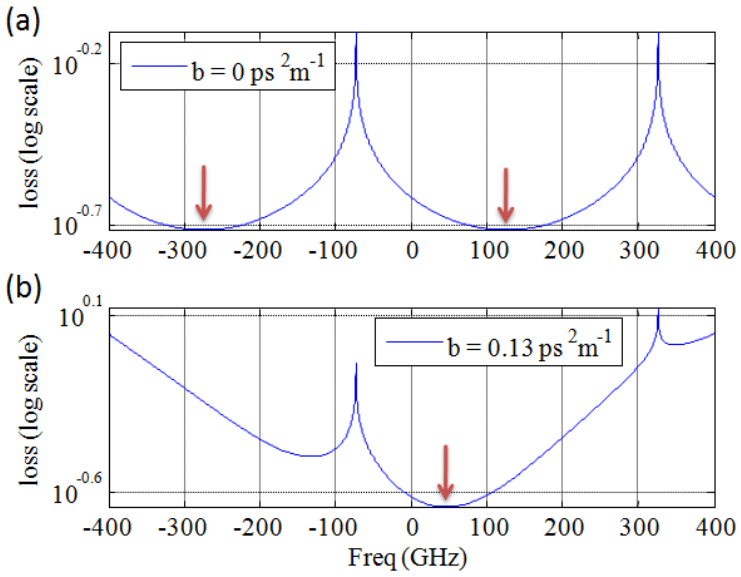

Figure 2.23: Figure 2.22 in logarithm scale for better visualization.

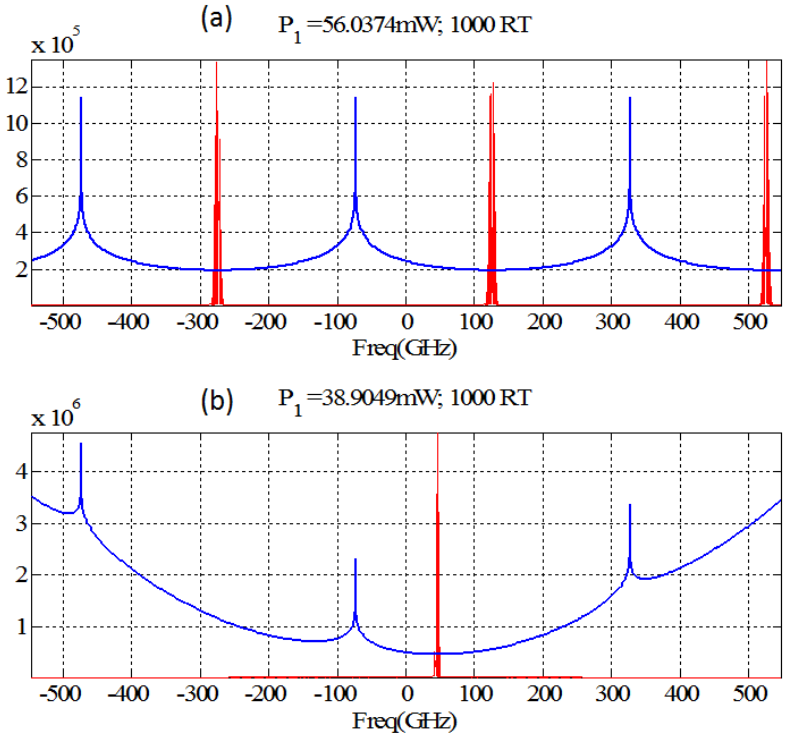

Figure 2.24: Overlapping the lasing frequencies with the loss profiles.

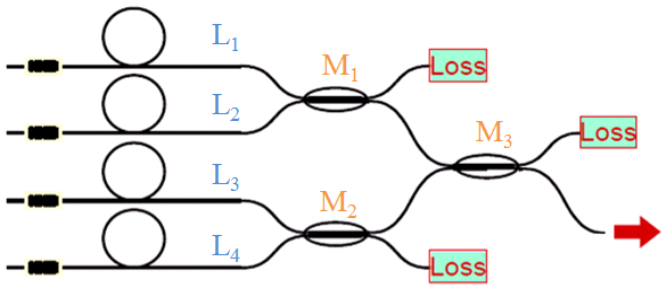

Figure 2.25: A four-channel fiber laser array. The figure is modified from Ref. [40].

Analytical proof can also be obtained by simple algebraic derivations. Consider, for example, a four-channel array in Figure 2.25, the combining is governed by the form chosen for the 50:50 directional coupler with Eq. (2.26). For any frequency f, constructive interferences occur at the lower, upper and lower output port of the couplers M_1, M_2 and M_3 in Figure 2.25 respectively when

$$\begin{aligned}
\frac{2\pi n_1 f}{c_0} 2(L_2 - L_1) &= \frac{\pi}{2} + m_1 2\pi \\
\frac{2\pi n_1 f}{c_0} 2(L_3 - L_4) &= \frac{3\pi}{2} + m_2 2\pi \\
\frac{2\pi n_1 f}{c_0} 2(L_3 - L_2) &= \frac{\pi}{2} + m_3 2\pi
\end{aligned} \tag{2.13}$$

where n_1 is refractive index of the fiber. We note the power additions in the coupler M_3 is entirely determined by the fiber length L_2 and L_3. This can be understood by calculating the phase of the output fields from the coupler M_1 that

$$\begin{bmatrix} 1 & -i \\ -i & 1 \end{bmatrix} \begin{bmatrix} e^{i2kL_1} \\ e^{i2kL_2} \end{bmatrix} = \begin{bmatrix} e^{i2kL_1} - ie^{i2kL_2} \\ -ie^{i2kL_1} + e^{i2kL_2} \end{bmatrix} \tag{2.14}$$

Assuming complete destructive interference occurs in the upper output port of M_1 such that $e^{i2kL_1} - ie^{i2kL_2} = 0$, the emerging field from the lower port $-ie^{i2kL_1} + e^{i2kL_2}$ then becomes $2e^{i2kL_2}$ with the substitution of e^{i2kL_1} by ie^{i2kL_2}. Similarly, the output of M_2 can be

calculated to depend on L_3 as well and so the phases of two inputs fields into M_3 are characterized simply by fiber length L_2 and L_3.

In general cases of random combinations of lengths L_1 to L_4, the exact common solutions of f do not exist for Eq. (2.13) even with the degrees of freedom given by integers m_1, m_2 and m_3, so only an optimal frequency $\overline{f}$ can be obtained. Let us assume $\overline{f}$ satisfies the following conditions.

$$\begin{aligned}
\frac{2\pi n_1 \overline{f}}{c_0} 2(L_2 - L_1) &= \frac{\pi}{2} + \Delta\phi_1 + m_1 2\pi \\
\frac{2\pi n_1 \overline{f}}{c_0} 2(L_3 - L_4) &= \frac{3\pi}{2} + \Delta\phi_2 + m_2 2\pi \\
\frac{2\pi n_1 \overline{f}}{c_0} 2(L_3 - L_2) &= \frac{\pi}{2} + \Delta\phi_3 + m_3 2\pi
\end{aligned} \tag{2.15}$$

$\Delta\phi_k, k = 1,2,3$ indicates the deviations of $\overline{f}$ away from the exact frequencies of each equation in Eq. (2.13) and is responsible for the imperfect power combining due to residual phase mismatch. The optimal $\overline{f}$ then corresponds to the array modes as observed in the previous spectral plots. We can calculate the period of these modes $\Delta\nu$ by replacing $\overline{f}$ with $\overline{f} + \Delta\nu$ in Eq. (2.15); at the same time, each length $L_k, k = 1\square 4$ can be expressed as some integer of their common divisor L_{gcd}. It is thus clear that $\Delta\nu$ needs to be

$$\begin{aligned}
\frac{2\pi n_1 \Delta\nu}{c_0} 2(\square_2 - \square_1) L_{\text{gcd}} &= m_1' 2\pi \\
\frac{2\pi n_1 \Delta\nu}{c_0} 2(\square_3 - \square_4) L_{\text{gcd}} &= m_2' 2\pi \\
\frac{2\pi n_1 \Delta\nu}{c_0} 2(\square_3 - \square_2) L_{\text{gcd}} &= m_3' 2\pi
\end{aligned} \tag{2.16}$$

where $\square_k, k = 1 \square 4$ and $m_k', k = 1 \square 3$ are all integers. Therefore the array mode period is obtained for all possibilities of $\square_k$ with

$$\Delta v = \frac{c_0}{2 n_1 L_{\text{gcd}}} \tag{2.17}$$

Extending the analysis to larger array size would produce the same results. Since the free spectral range of each laser element is given by $c_0 / 2 / n_1 / L_k = c_0 / 2 / n_1 / (\square_k L_{\text{gcd}})$, Δv can also be viewed as their least common multiple as reported in Ref. [62].

2.5 Discussions

As mentioned in the very beginning, the fact of the combining efficiency decreasing rapidly with increasing array size has been a major blockade in the path of pursuing high power fiber laser sources using the array approach. To overcome the limit, there have been some efforts in implementing the fiber laser array structure with broadband components [33] for it is commonly believed that enlarging the bandwidth would improve the combining efficiency [33, 39, 40]. Such an argument, although not incorrect, is incomplete and sometimes misleading. In fact, widening the spectrum does not necessarily boost the efficiency as desired. To clarify this point, two levels of combining limitations should be recognized. First, the finite bandwidth (appeared in Figure 2.12 as loss dispersion) leads to the shift of the lasing frequency away from the resonances of the composite cavity and generates output power from the lossy ports as a result of the inexact relative phase at the coupler inputs. Second, even if the array lases at the resonant frequencies, the combining may still be imperfect because the inexistence of the exact coincidental mode of the system sets the upper limit to the efficiency as exemplified and explained in Sec. 2.4.5. Therefore, increasing bandwidth can only mitigate the power

losses to a certain extent. The fundamental limitations which come from the incontrollable fiber lengths, and quickly cause the array to be ill-conditioned as the number of lasers increases, are inevitable.

While the simulations presented here involved following the progress of a unidirectional wave as it propagates around a composite cavity, the model is easily extended to include counterpropagating waves as well as different polarizations. Because the solution scheme is the highly efficient split-step Fourier method, the model can be used to simulate the dynamics of many coupled amplifiers.

2.6 Array simulation results: modes formation

Up to now, we have been focusing on the steady-state analysis of fiber laser arrays, ignoring their transient responses. In this section, we demonstrate the generality of our model by incorporating the population relaxation into the wave propagation and illustrate the build-up process of the array modes from noisy spontaneous emissions. Starting from the rate equation, Eq. (2.6) is reformulated through change of variables $P_{sat} = h\nu / \sigma\tau \times A_{eff}$, $g_j = 2\sigma\Delta N_j$ and $g_{0j} = 2\sigma R_p(t)\tau$ that

$$\tau \frac{dg_j(z,t)}{dt} = g_{0j} - g_j(z,t)(1 + \frac{\left|E_j(z,t)\right|^2}{P_{sat}}) \tag{2.18}$$

Instead of turning on g_j abruptly as of previous sections, we take the gain growth dynamics into account and retain the dependence on both time and position. Due to the discrete nature of numerical computation, the fiber length is partitioned into segments and we deal with integrated gain variable $g_j = \int_{z_0}^{z_0+\Delta} g_j dz$ eventually rather than $g_j(z,t)$ in Eq. (2.18). The multiplication of the gain variable and the intensity field on the right

hand side of Eq. (2.18), however, is difficult to integrate without losing any accuracy. We thus perform simple derivations replacing the multiplication following Ref. [21].

According to Beer's law $d\left|E\right|^2/dz = g\left|E\right|^2$ [27], Eq. (2.18) can be written as

$$\tau \frac{dg_j(z,t)}{dt} = g_{0j} - g_j(z,t) - \frac{1}{P_{sat}} \frac{d\left|E_j(z,t)\right|^2}{dz} \tag{2.19}$$

To simplify the computation steps, we integrate g_j along $z \in [z_0, z_0 + \Delta]$ and define $\bar{g}_j = \int_{z_0}^{z_0+\Delta} g_j dz$ that Eq. (2.19) becomes

$$\tau \frac{d\bar{g}_j}{dt} = \bar{g}_{0j} - \bar{g}_j - \frac{\left|E_j(z_0+\Delta,t)\right|^2 - \left|E_j(z_0,t)\right|^2}{P_{sat}} \tag{2.20}$$

Further approximation can be made with the relation $\left|E(z_0+\Delta)\right|^2 = e^{\bar{g}}\left|E(z_0)\right|^2$. Its substitution into Eq. (2.20) produces the final expression for the rate equation

$$\tau \frac{d\bar{g}_j}{dt} = \bar{g}_{0j} - \bar{g}_j - \frac{(e^{\bar{g}}-1)\left|E_j(z_0,t)\right|^2}{P_{sat}} \tag{2.21}$$

Finally the coupled equations (2.5) and (2.21) are solved together using SSFM and Euler method, where the latter connects the integrated gain variable at current and next time incidents, i.e. $\bar{g}_j$ and $\bar{g}_j'$, by

$$\bar{g}_j' = \bar{g}_j + \frac{d\bar{g}_j}{dt}\Delta t \tag{2.22}$$

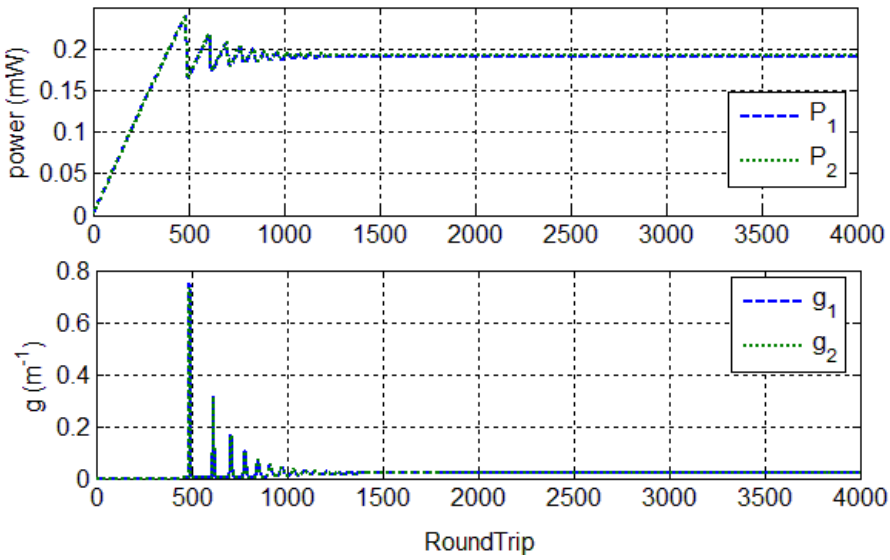

Figure 2.26: The transient response of a two-channel fiber laser array. Parameters used: γ = 0 $W^{-1}m^{-1}$, L_1 = 24.3 m, L_2 = 24.0 m and *rtstps* = 24. Refer other values to Table 2-1. The powers are taken before they enter the directional coupler and the gains are averaged throughout the cavity.

Since the gain fields are updated every roundtrip, the small interval Δt is set to the roundtrip time T in the simulation. To validate our derivation of the dynamical model, an example is given for a two-channel fiber laser array of fiber lengths 24.3 and 24.0 m. Provided 0 $W^{-1}m^{-1}$ for γ, each of the active fiber is partitioned into 24 segments (*rtstps* = 24 in Table 2-1.) The simulation results are shown from Figure 2.26 to Figure 2.29. Clearly, the transient oscillations are exhibited in the beginning of the excitation. The array damps after a number of roundtrips and settles down eventually to a constant number as seen in Figure 2.26. Intuitively, the steady states obtained here should match up to the static simulation under same parameter values; indeed, their comparison shows reasonable agreement with each other that the saturated gain variables are practically identical and the combined output powers from both methods are close to 40 mW. The model is then continued for studying the dynamical behavior of the power spectrum.

Figure 2.27 illustrates the formation process of the array modes growing out of uniform and noisy spontaneous emissions. It is seen that the modes build up rather quickly with spectral modulations developed within 500 roundtrips. Zooming in on the spectrum further shows the evolution of the longitudinal modes of the structure in Figure 2.28. This result is particularly appealing for the fundamental characteristic of the laser cavity manifest itself naturally out of the model as anticipated. In the end, the phase dynamics is examined and Figure 2.29 confirms the phase-locked operation of the fiber laser array.

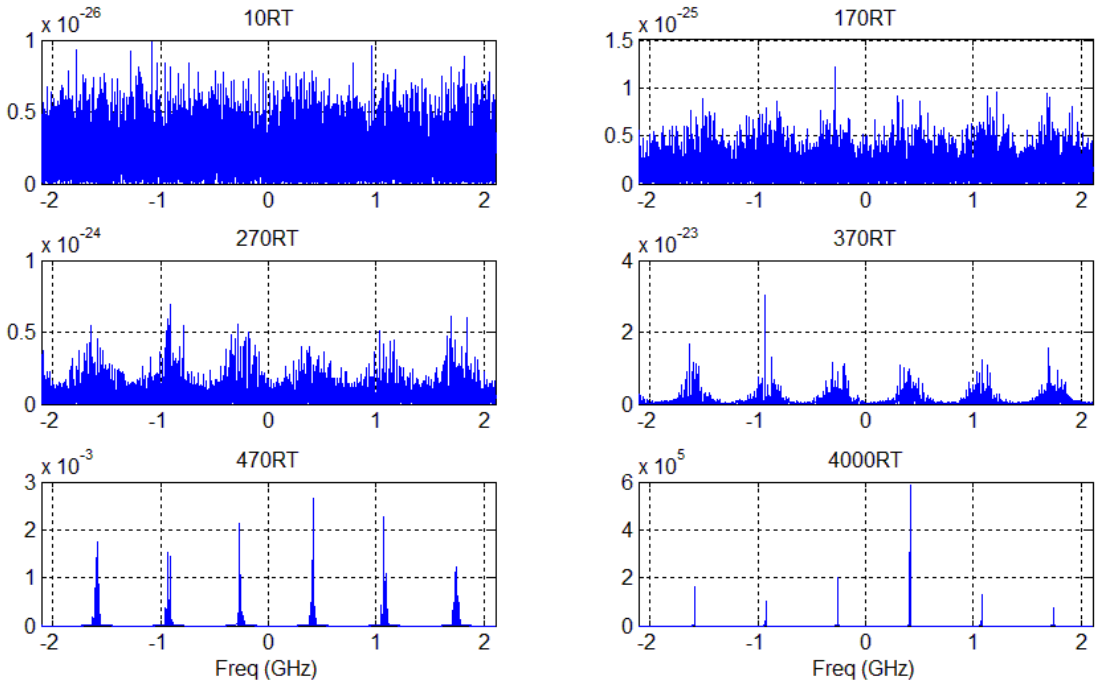

Figure 2.27: Following Figure 2.26, the power spectrum evolves from noisy and uniformly-distributed to clean and periodic spikes.

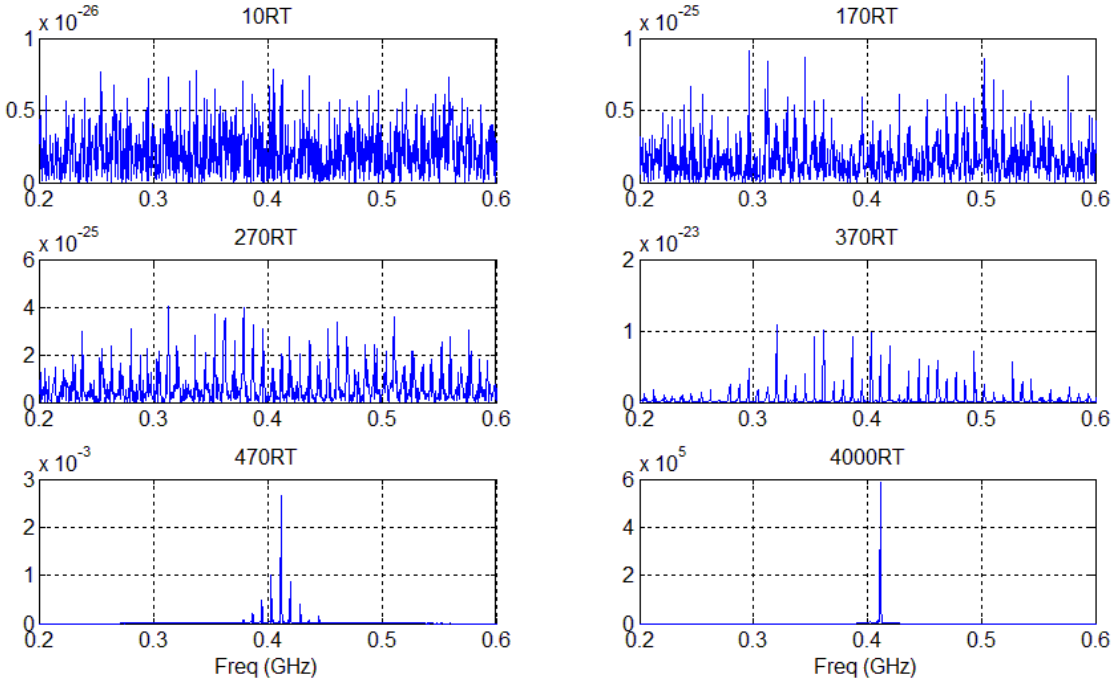

Figure 2.28: Figure 2.27 is zoomed in for emphasizing the development of the longitudinal modes.

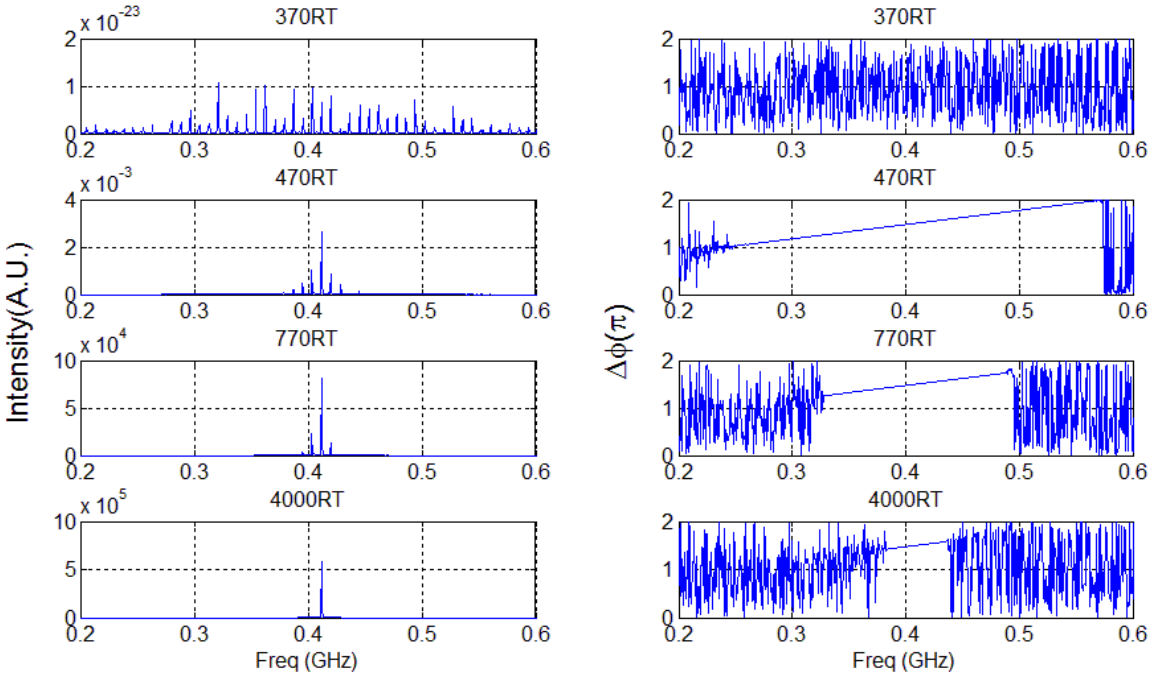

Figure 2.29: The array modes formation (left column) is accompanied by the evolution of the relative phase (right column.) The phase locking behavior is evident near 0.4 GHz, and $\Delta\phi$ exhibits irregular time-varying fluctuations for other non phase-locked frequencies.

In summary, we have derived the iterative difference maps for the rate equation and demonstrated the extended model by incorporating the gain evolution into the wave propagation. Although the relaxation process of the gain fields does not affect the steady-state results of beam combining at this point, its inclusion, even within single fiber lasers, may induce rich dynamics and is important to consider whenever stability issues are encountered. As a matter of fact, there have been a number of publications focusing on the gain dynamics of fiber laser arrays in the context of single longitudinal mode analysis [46]. The model presented here then serves as its continuation to the multi-mode regime and provides various possibilities for further investigations.

2.7 Bidirectional fiber laser arrays

Step by step, we have built an effective model for passive fiber laser arrays and explore the coherent combining in many different aspects based on the ring cavity configurations. Although the model is complete in a way that essentially all kinds of mechanisms are considered and great insights can be obtained out of this unidirectional model, it is not entirely clear to us to what extent the exclusion of backward waves and the associated phases changes affect power combining unless the full model of Fabry-perot cavities are solved unambiguously. At least two other models have been published with the consideration of bidirectional configurations [21, 36]; however, both are built on the basis of single-longitudinal-mode assumption while the multi-longitudinal-mode nature of fiber lasers is a key component for successful combining. In this section, we present an improved, the very most complete, model by solving mutually-coupled nonlinear Schrödinger equations for counterpropagating waves together with co-saturated rate equations in an effort to fully understand the array combining mechanisms. It is revealed that the presence of backward waves is insignificant to coherent combining as we suspected in the first place.

A two-channel fiber laser array is depicted in Figure 2.30 with two independent single mode fibers coupled discretely by a directional coupler. The coherent waves propagating in +z and −z directions in each fiber laser are governed by the (nonlinear) Schrodinger equation together with the rate equation.

$$\frac{\partial E_j^f}{\partial z} = \frac{1}{2}(g_j - \alpha)E_j^f - \beta_1 \frac{\partial E_j^f}{\partial t} + \frac{1}{2}(b - i\beta_2)\frac{\partial^2 E_j^f}{\partial t^2} + i\gamma(\left|E_j^f\right|^2 + 2\left|E_j^b\right|^2)E_j^f \qquad (2.23)$$

$$\frac{\partial E_j^b}{\partial z} = -\frac{1}{2}(g_j - \alpha)E_j^b + \beta_1 \frac{\partial E_j^b}{\partial t} - \frac{1}{2}(b - i\beta_2)\frac{\partial^2 E_j^b}{\partial t^2} - i\gamma(2\left|E_j^f\right|^2 + \left|E_j^b\right|^2)E_j^b \qquad (2.24)$$

$$\tau \frac{dg_j(z,t)}{dt} = g_{0j} - g_j(z,t) - \frac{\left|E_j^f\right|^2 + \left|E_j^b\right|^2}{P_{sat}} g_j(z,t) \tag{2.25}$$

E_j^f, E_j^b and g_j refer to the slowly varying envelope of the forward and backward electric waves and the gain field in the first and the second fiber for j = 1,2 respectively. Various effects including linear gain g_j, fiber losses α, the inverse of the group velocity β_1, the frequency-dependent losses b, the group velocity dispersions β_2, and the nonresonant Kerr nonlinearity γ are all incorporated in Eqs. (2.23) and (2.24). For gain dynamics, g_{0j} specifies the unsaturated gain in Eq. (2.25). Its second and third terms describe the process of excited population relaxation with upper-state lifetime τ and laser gain saturation at high intensity fields. We normalize the electric field amplitudes so $|E_j|^2$ corresponds to the power distributions. The 50:50 directional coupler connecting the inputs E_1^b, E_2^b to the outputs A_1, A_2 is represented by a linear matrix.

$$\begin{pmatrix} A_1 \\ A_2 \end{pmatrix} = \frac{1}{\sqrt{2}} \begin{pmatrix} 1 & -j \\ -j & 1 \end{pmatrix} \begin{pmatrix} E_1^b \\ E_2^b \end{pmatrix} \tag{2.26}$$

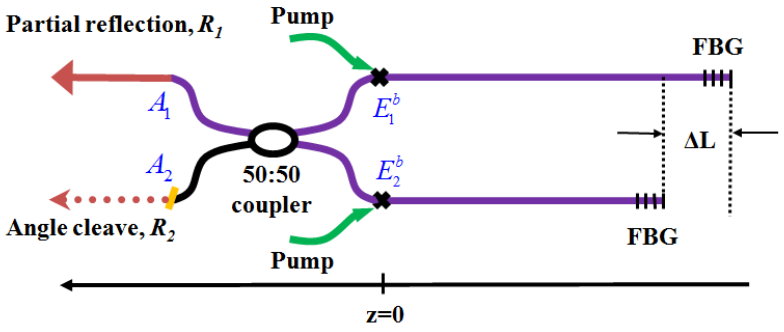

Figure 2.30: a two-channel fiber laser array

It is clear that the forward and backward waves are coupled through the cross-phase modulation and also the co-saturation of the gain fields. Unlike solving unidirectional

fiber laser arrays where straightforward integration of split step Fourier method (SSFM) is applied [47], here the nonlinearly-coupled differential Eqs. (2.23)-(2.25) require some self-consistent solutions of E_j^f and E_j^b existing for all $z \in [0, L]$ as well as all t within the computation window. We handle such simulation by iterative SSFM [63] that E_j^f, E_j^b are in turn integrated along +z and –z directions respectively while the information of the updated field is stored and used to compute the other one at a later time. The iteration continues until certain convergences are reached.

In the dynamical aspects of the array, rather than turning on g_j abruptly as assumed in many cases [47, 61], we take the gain growing transition into account and retain its dependence on both time and position. Eq. (2.25), however, is not readily used for integration due to the discretized nature of numerical computation that a preferable expression can be derived instead. Based on beer's law $d\,|E_j^f|^2/dz = +g_j\,|E_j^f|^2$ and $d\,|E_j^b|^2/dz = -g_j\,|E_j^b|^2$, the rate equation can be written as

$$\tau \frac{dg_j(z,t)}{dt} = g_{0j} - g_j(z,t) - \frac{1}{P_{sat}}\left(\frac{d\left|E_j^f\right|^2}{dz} - \frac{d\left|E_j^b\right|^2}{dz}\right) \tag{2.27}$$

Integrate g_j along $z \in [z_0, z_0 + \ell]$ and define $\bar{g}_j = \int_{z_0}^{z_0+\ell} g_j dz$, we find that Eq. (2.27) becomes

$$\tau \frac{d\bar{g}_j(t)}{dt} = \bar{g}_{0j} - \bar{g}_j(t) - \frac{1}{P_{sat}}\left(\left|E_j^f(z_0+\ell)\right|^2 - \left|E_j^f(z_0)\right|^2 - \left|E_j^b(z_0+\ell)\right|^2 + \left|E_j^b(z_0)\right|^2\right) \tag{2.28}$$

Further approximation can be applied with the relation $|E_j^f(z_0+\ell)|^2 = e^{\bar{g}_j(z_0)}\,|E_j^f(z_0)|^2$ and $|E_j^b(z_0)|^2 = e^{\bar{g}_j(z_0+\ell)}\,|E_j^b(z_0+\ell)|^2$ for sufficiently small length ℓ. Its substitution into Eq. (2.28) produces the final expression for the rate equation.

$$\tau \frac{dg_j(t)}{dt} = g_{0j} - g_j(t) - \frac{1}{P_{sat}}[\left|E_j^f(z_0)\right|^2 (e^{g_j(z_0)} - 1) + \left|E_j^b(z_0 + L_j)\right|^2 (e^{g_j(z_0+L_j)} - 1)] \quad (2.29)$$

Together Eqs. (2.23), (2.24) and (2.29) are solved by iterative SSFM and the Euler method, where the latter is adopted for connecting the integrated gain variable at current and next time incidents, i.e. g_j and g_j' by

$$g_j' = g_j + \frac{dg_j}{dt}\Delta t \quad (2.30)$$

We set the increment step Δt to be four times of roundtrip duration in the simulation because numerical accuracy is ensured when Δt (~1 μs) is much smaller than the population relaxation time constant τ (10 ms). To validate our derivation of the dynamical model, an example is given for a two-channel fiber laser array of fiber lengths 24.3 and 24.0 m. Although it has been shown that nonlinear phases do not come to play at small cw power level [61] in terms of combining, still we assume 0.003 $W^{-1}m^{-1}$ for γ and include the mechanism without losing any generality. Each of the active fiber is partitioned into 70 segments (*rtstps* = 70) and other parameter values used are $\lambda_0 = 1.545\mu m,\ \alpha = 0.058m^{-1},\ g_0 = 2.67m^{-1},\ n_1 = 1.5,\ \beta_2 = -0.003ps^2m^{-1},\ b = 0.13ps^2m^{-1}$ and $P_{sat} = 0.6mW$.

The simulation results are illustrated from Figure 2.31 to Figure 2.33. It is interesting to see that in addition to the standard SSFM outputs (temporal and spectral domain profiles), the spatial distributions and dynamical evolutions of the array can also be retrieved from our model. The distributions refer to the self-consistent solutions of the coupled equations and they are plotted with red circles in Figure 2.31 for (a) both propagating waves and (b) the gain field within one of the fiber laser (L_1 = 24.3 m). It is

clear that the backward signal dominates in this efficient backward pumping configuration [Upadhyaya BN] and the resulting gain field exhibits stronger saturations near the front end of the fiber. For verifying purposes, the time derivative and nonlinear terms of Eqs. (2.23)-(2.25) are to be ignored since in practice, they are not affecting the field distributions at steady states. We solve the simplified ODEs together with the boundary conditions using the built-in BVP (boundary value problems) solver of Matlab. The solid black line stands for such solutions in Figure 2.31(a),(b) and its agreement with that of red circles supports our simulation results. As for array dynamics, the time evolutions of (c) the output power, coming out of the partially-reflected port, and (d) the gain variable (averaged over z) in both fiber lasers are clearly observed in Figure 2.31. The array exhibits transient oscillations in the beginning of the excitation and settles eventually after a few milliseconds. At steady states, the averaged gain variables $\overline{g}_{1,2}$ amount to 0.1244 and 0.1251 m^{-1} that they, in compliance with the fundamental laser theory, match up to the roundtrip losses of $\alpha - \ln(R)/2/L_{1,2}$ as desired.

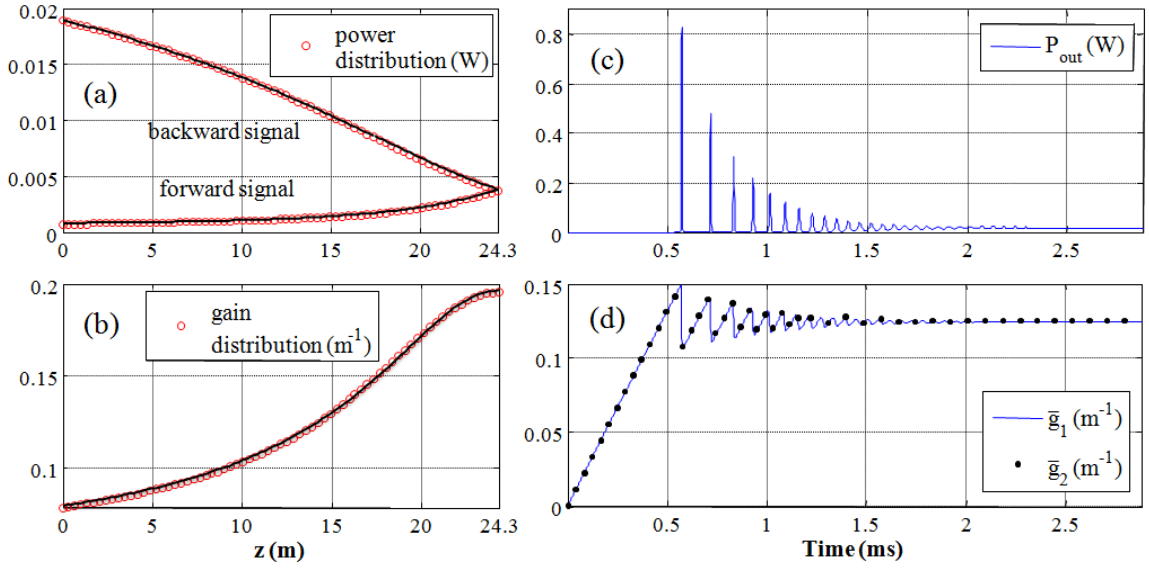

Figure 2.31: The spatial distributions of one of the fiber laser (L_1 = 24.3 m) are plotted as an example for (a) both propagating waves and (b) the gain field along the z axis. The three curves consisted of red circles present the self-consistent steady-state solutions obtained from our model, while that of solid black lines are calculated from Matlab with its built-in BVP solver. Their comparison shows good agreement and thus supports our simulation results. As for array dynamics, the time evolution of the output power and the averaged gain variable (over z) of each fiber are displayed in (c) and (d). The output power refers to the combined power coming out of the partially-reflected, R_1, port as seen in Figure 2.30.

We now turn to the beam combining properties of the array. The temporal (left) and spectral (right) domain outputs are shown in Figure 2.31. As expected, almost all powers come out of the upper, partially reflected R_1 port, while a negligible amount leaks through the lower, angle-cleaved R_2 one. The calculated combining efficiency is close to 100% and is consistent with experimental observations even in the presence of the backward waves. To fully understand the effect of counterpropagating waves for array combining, we examine the modulated power spectrum in which a series of equally-distant spikes appears as a result of Vernier effects. The modulation period, measured to be 0.333 GHz from Figure 2.32(a), is in agreement with the theoretical formulation of

$\Delta v = c/2/n_1/\Delta L$ [32]. Compared with that of 0.667 GHz obtained from unidirectional fiber laser arrays [61], the twice difference can be readily understood by the fact that the optical path lengths double in the bidirectional configurations and the period halves accordingly. Such simulation results suggest that, besides giving rise to additional phases through propagation, the backward waves merely serve to co-saturate the population inversion and do not seem to involve with the working mechanism of coherent beam combining, in which the key component is truly the multilongitudinal modes of fiber lasers.

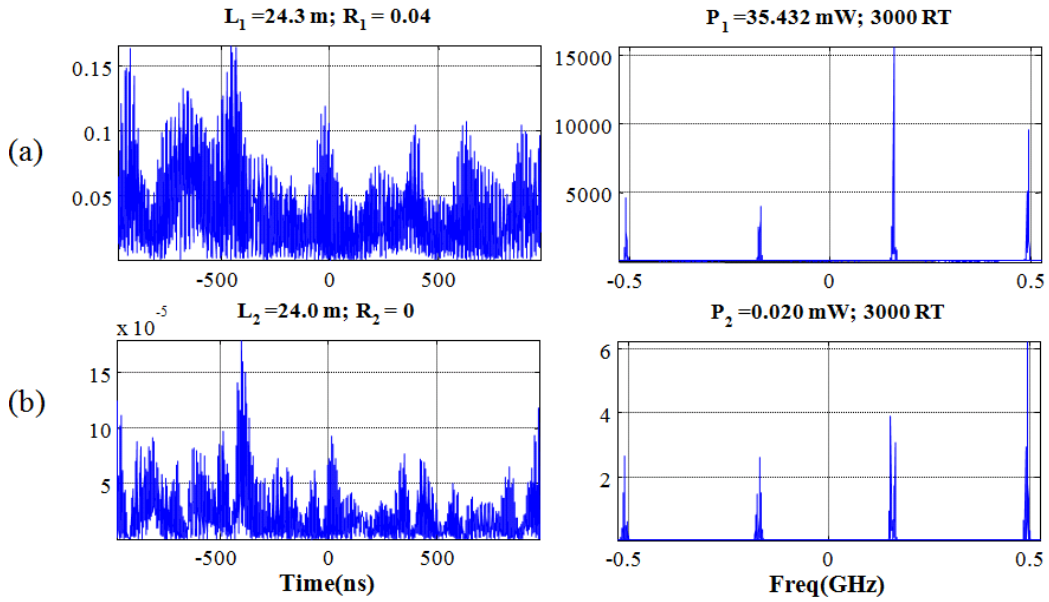

Figure 2.32: An Eb-doped fiber laser array in Fig. 1 with L1 24.3 and L2 24.0 m. The output powers from (a) upper port with partial reflectivity and (b) lower, angle-cleaved, port are plotted for time (left) and frequency (right) domains respectively. The separation between spikes is measured to be 0.333 GHz.

To fully characterize the array dynamics, the model is used continuously to study the formation process of the coincidental modes and also the associated phase-locked states. The evolutionary spectra are illustrated in Figure 2.33 for (a) the combined output

power and (b) the relative phase difference $\Delta\phi$ between two incident (backward) waves at $z = 0$ before the 50:50 coupler, where $\Delta\phi$ is defined as modulo of (ϕ_1 - ϕ_2) by 2π. The serial snapshots demonstrate the array grows out of noisy spontaneous emissions and is continually filtered due to the interferometric nature of the composite cavity. As time increases, the sinusoidal width shrinks considerably that gain narrowing effect is evident. Along the transition, the phase plots are also seen to develop interesting structures with slanted straight lines crossing the peaks of the corresponding modulation envelopes as indicated by red arrows in Figure 2.33. Note these oblique lines center around 1.5π in the vertical axes of Figure 2.33(b) for this particular phase difference yields constructive interferences in the upper output port of the directional coupler and destructive ones in the other. Finally, cross-referencing the time orders of Figure 2.31(c) and Figure 2.33 reveals that both modes formation and the phase-locking behavior establish very early before the oscillation begins.

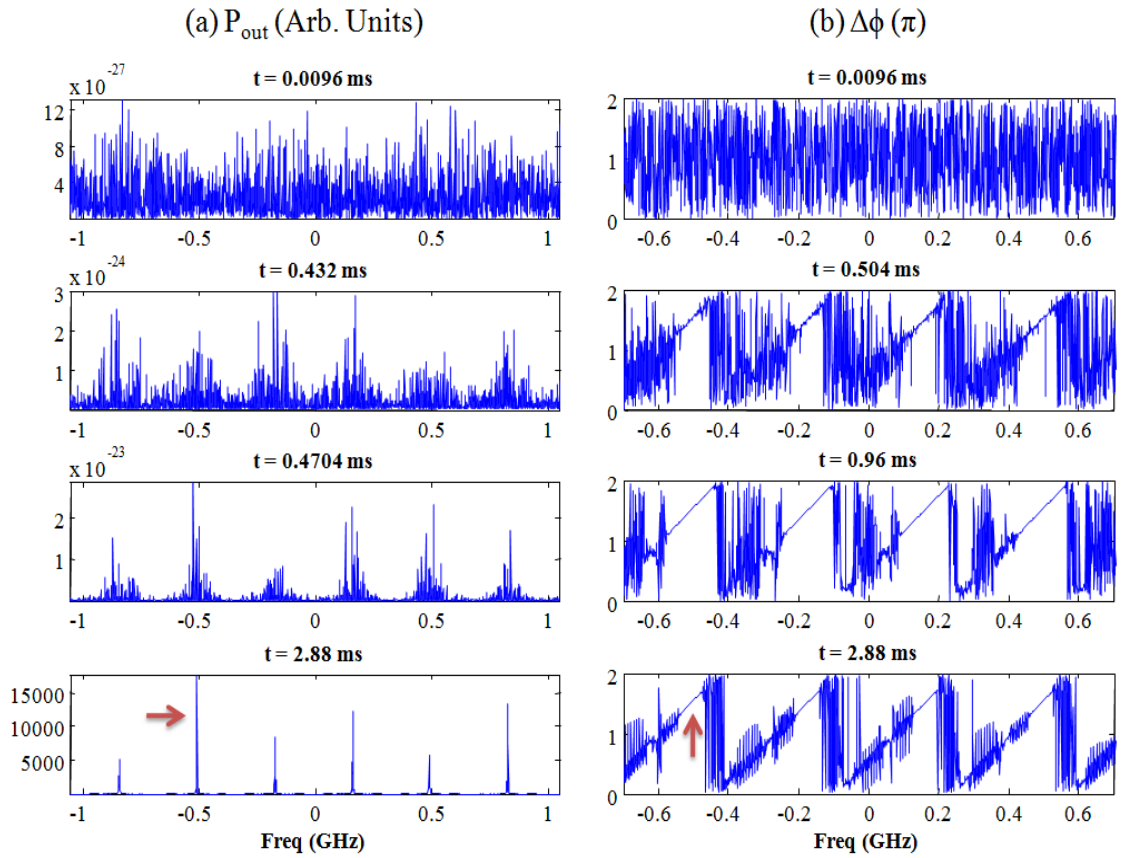

Figure 2.33: Evolution diagram of (a) the output power spectrum and (b) the relative phase difference $\Delta\phi$ between two incident (backward) waves at $z = 0$. Both start from random and noisy spontaneous emissions. Note the correlations between two spectra are pointed out by red arrows.

2.7.1 **Greatest common divisor**

As mentioned and proved in Sec. 2.4.5, the array mode spacing of a four channel fiber laser array is determined by the greatest common divisor of the four fiber lengths. Such information is important since the number of array modes within certain bandwidth is inversely proportional to the modal periods, and we usually relate the combining efficiency drop to the unavailability of these coincidental modes. The knowledge of the determinant of the periodicity is thus critical for large array size in the attempt to resolve the efficiency issues. Instead of relying on probability calculations of mode numbers as

proposed by Siegman [40], in this section we expand the newly developed bidirectional model for eight and sixteen channel fiber laser arrays and look for supporting evidence of the dependence of mode periodicity on the greatest common divisor of the consisting fiber lengths.

Consider firstly an eight-channel fiber laser array with designed array elements to be multiples of 5 cm as seen in the #1 row of Table 2-2. Other parameters are referred to Table 2-1 except β_2 and γ are set to zero since they have negligible effects. Also the loss dispersion coefficient b is turned off so as to relax bandwidth restrictions. Theoretical period Δv is calculated to be 2 GHz with refractive index of 1.5. The resulting power spectrum is shown in Figure 2.34(a), and indeed the pattern periodicity is measured to be 2 GHz as expected. These fiber lengths are, of course, not realistic and one may wonder if it is the smallest length difference, which happens to be 5 cm in this case, determines the mode periodicity. We perform the second trial of simulation using random number generator for length assignments. Eight random numbers are given within the range of 23.5m and 24.5m with a resolution of 1 cm as seen in the #2 row of Table 2-2. This time, the smallest length difference is 2 cm (24.18-24.16), but the simulated period in Figure 2.34(b) is 10 GHz and is corresponding to the greatest common divisor of 1 cm. The final verification is realized for a 16-channel fiber laser array in Figure 2.34(c) and again it confirms such results.

Table 2-2: Lengths parameters for three fiber laser arrays

#1 Eight-channel (m)	24.00	24.30	23.80	24.10	24.05	24.35	24.25	24.55
#2 Eight-channel (m)	24.21	23.77	24.16	23.62	24.26	24.18	23.66	24.00

#3 Sixteen-channel (m)	24.84	24.31	24.36	24.31	24.84	23.07	24.52	23.34
	24.59	24.70	24.49	24.41	24.92	24.87	23.78	23.06

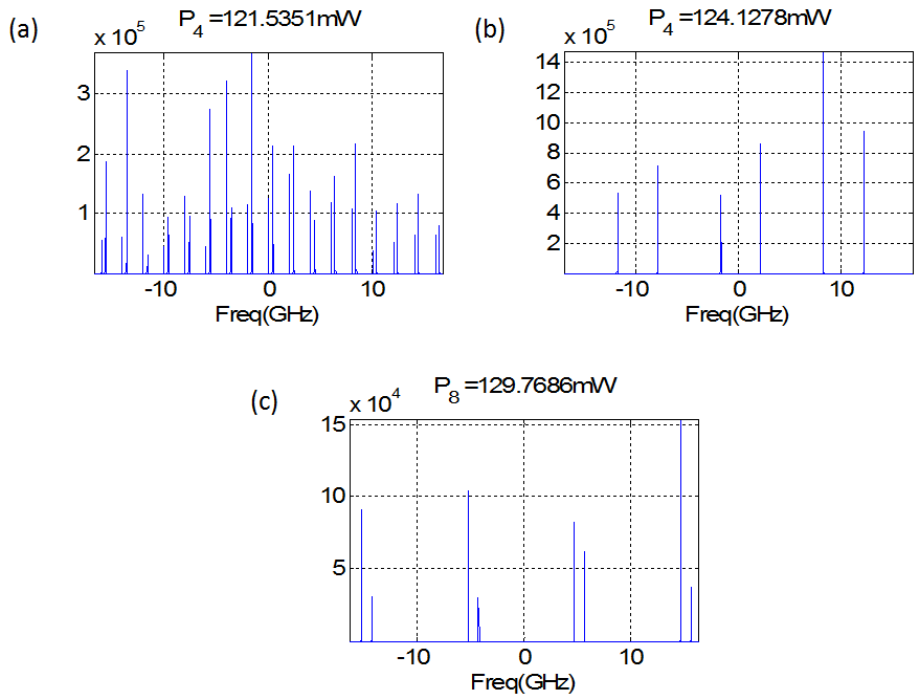

Figure 2.34: Simulated power spectrum (a) – (c) corresponds to three sets of arrays with lengths parameters #1 – 3 taken from Table 2-2. See Table 2-1 for other parameters with exceptions of β_2, γ and b.

2.8 Conclusion

The self-adjustment process that leads to the efficient and robust combining of fiber lasers depends on the existence of a dense set of longitudinal modes from which the laser can select those that satisfy the minimum loss condition at the coupler. In our model, changes in fiber length differences are automatically compensated by changes in the lasing wavelength and the spectral signature of the combined lasers. The spectral changes seen in our simulations agree with experimental observations. We find that at these power

levels the non-resonant nonlinear refractive index is not a significant factor in beam combining.

In conclusion, we have proposed a new model for studying discretely coupled fiber laser arrays. The model incorporates propagation effects, multiple longitudinal modes, unbalanced mirror reflectivities, uncontrolled fiber lengths, the intensity-dependent refractive index, and gain saturation. It lends support to the picture of coherent beam combining as simply the natural selection of the supermodes of a composite cavity that has the lowest loss. Moreover, the dynamical process of gain relaxation and its interaction with counterpropagating waves are also incorporated into the model and their effect on the coherent combining mechanism is shown to be negligible. Future investigation toward polarization effects or diverse combining configurations for array scalability [64] is entirely possible.

CHAPTER III

Modeling experimental results on array power scaling and fluctuations

3

3.1 Introduction

The possibilities of multi-kW power scaling by passive coherent phasing of fiber laser arrays have urged us to investigate further its combining performances for greater array sizes. It is clear now the passive beam combining of an *N*-channel fiber laser array can be regarded as an interferometric system of *N*-coupled amplifiers in a composite cavity. The multiple longitudinal modes of individual fiber lasers of varying lengths are superposed to form coherently-combined modes (or supermodes) of the composite cavity whenever there is a coincidence in the individual frequency combs. As the number of elements in the array increases, the probability of finding such an accidental coincidence in the resonances of the array system is decreased, and thus the combined-power efficiency drops.

Regardless of diverse combining methods or configurations proposed (discussed in Sec. 1.1), the most important question associated with this beam combining approach is how the coherent-combing efficiency scales with the array size. The initial experimental explorations using a fixed 8-channel array by Shirakawa et al [33], and, more recently, using a fixed 4-by-4 ring laser array configuration by Shakir et al, indicate that combining efficiency is expected to decrease with the increase of the array size. This

appears to be supported by theoretical estimates as well [37, 40, 57, 61]. However, due to the limited experimental data and the approximate character of the first theoretical estimates [37, 40, 57], this passively-phased array size scaling is still not sufficiently understood.

In this chapter we present a systematic experimental and simulation study of 2- to 16-channel fiber-laser array coherent phasing. The array size scalability of combined-power efficiency is explored by using a new simulation model and comparing its results with experimental data. Good agreement between simulation and experiments demonstrates for the first time the evolution of combined-power efficiency with array size up to 16-channel with a 2-laser array interval. We also explore for the first time the important question of the dependence of power fluctuations on array size. The beat spectra are studied as well to provide supportive evidence of the diminishing probability of finding supermodes in a larger array size. Finally, the simulation of highly efficient combining by the means of optical phase conjugation mirrors is performed and discussed.

3.2 Power fluctuation of fiber laser arrays

Being consistent with previous studies in CHAPTER II, an all-single-mode-fiber configuration, where the combining is accomplished using 50:50 single-mode fiber couplers, is chosen for exploring fiber-laser array passive-coherent phasing. This enables a simple and easily scalable experimental implementation, with unambiguous beam-combining interpretation. The experimental setup is shown in Figure 3.1 as an example for 16-channel combining. Each single-mode fiber laser channel consists of a 980/1064-nm WDM, connected to a 3.5-m long Yb-doped single-mode fiber with a 1064-nm faraday mirror at one end of the cavity. These laser channels are combined into various-

sized arrays using 50:50 single-mode couplers. The basic building block is a 2-laser array, thus all array sizes between 2 and 16 are explored as multiples of 2 (2, 4, 6, 8, 10, 12, 14, and 16). The individual configurations are arranged as in Figure 3.2 with the total lengths of the 2, 4, 8, 16-channel lasers being 8.5m, 10.5m, 12.5m, and 14.5m, respectively. The output-end of the cavity of this array is formed by a single straight-cleaved fiber-end, providing ~4% back reflection. All the other remaining output leads of 50:50 fiber couplers are angle-cleaved to prevent feedback from these ends. During experiments an optimized coherent combination has been attained by balancing pumping power for each 2-channel building block such that power equality of two inputs of each fused coupler is achieved. Due to the broad-band nature of Faraday mirrors, each laser channel was operating at ~8nm spectral bandwidth.

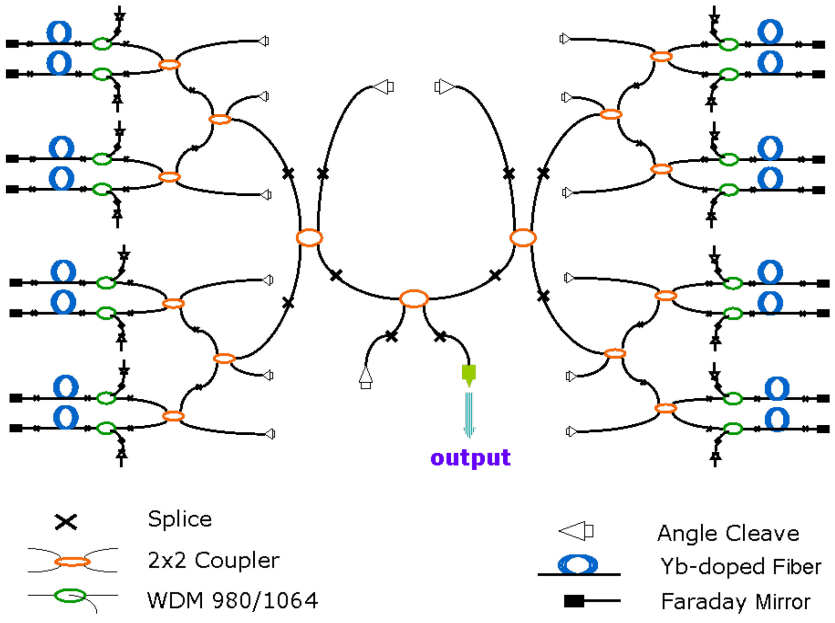

Figure 3.1: Experimental setup as an example of 16-channel combining [Chang].

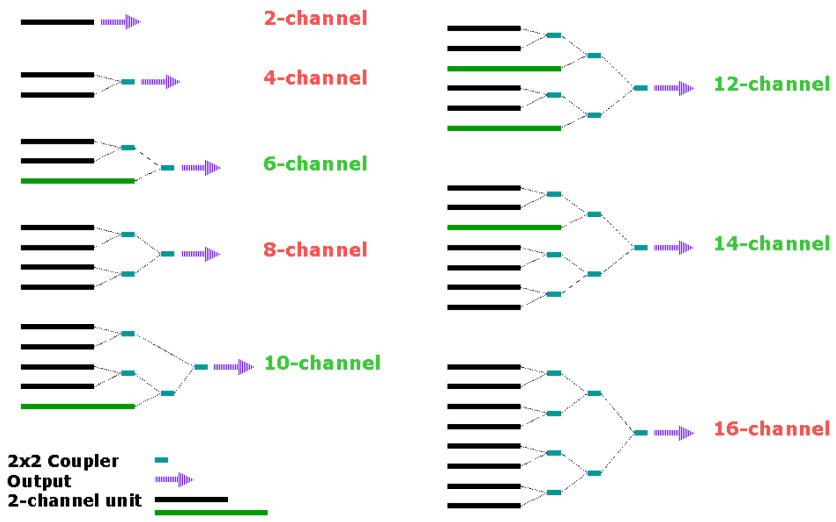

Figure 3.2: Configurations of 2 to 16-channel combining with a 2-laser array interval [Chang].

3.2.1 **Power scalability experiment**

Taking P_{out} as the output of the straight-cleaved end and P_i as the power from the i^{th} single laser if uncoupled, we define the power combining efficiency for an N-channel array as

$$N\text{-channel combined-power efficiency} = \frac{P_{out}}{\sum_{i}^{N} P_i} \qquad (3.1)$$

The power is measured with a typical power meter with a response time of millisecond. Because of power fluctuations on a time-scale of microsecond (round-trip time) we record the statistical mean over 5 minutes. The measured power combining efficiencies (blue solid dots) and their fluctuations (error bars) for 2, 4, 6, 8, 10, 12, 14, and 16-channel combining are shown in Figure 3.3 and listed in Table 3-1.

The calculated power combining efficiencies (green solid dots) are obtained from the newly developed model (CHAPTER II) with following parameters: λ (working

wavelength) = 1.064 μm, *b* (loss dispersion) = 0.013 ps^2/m, g_0 (unsaturated gain) = 2.67 m^{-1}, γ (nonlinear coefficient) = 0.003 $W^{-1}m^{-1}$, α (propagation loss) = 8 dB/km, and β_2 (phase dispersion) = 0.024 ps^2/m. Since it is based on the amplifying nonlinear Schrödinger equation, effects such as gain saturation, fiber nonlinearity, group velocity dispersion, and loss dispersion of bandwidth limiting elements in the cavity can be readily taken into account. It also exhibits self-adjustment process of beam combining suitable for describing the dynamic features such as power fluctuation and beat spectra. According to our study, nonlinearity has little effect on power efficiency, power fluctuation, and beat spectra.

In terms of numerical implementation, Fortran 90 is adopted for the split-step Fourier method (SSFM), where electric fields are transformed alternately between temporal and spectral domains. We use FFTW library [65] for fast evaluation of Fourier transform and the random number generators of AMD Core Math Library (ACML) for initiating the array with spontaneous emission noises of small complex random numbers. Although the combination of Fortran and SSFM is relatively fast compared with other programming languages or solving algorithms, the computation time is directly scaling with the number of array elements. The simulation of 16-channel arrays thus may be lengthy up to several hours not to mention it will be even longer if more points, i.e. broader bandwidth or higher resolution, are required. To effectively reduce computation durations, we implement parallel algorithm by Fortran Message Passing Interface (MPI) library since discretely coupled fiber laser arrays are perfect starting points in parallelized computing that each fiber laser can be solved simultaneously and individually before the coupling take place in one end after each roundtrip. This way, simulations of *N*-channel arrays can

be as short as that of single fiber laser and quick results can be obtained within 15 minutes in most cases. Finally, unidirectional model is utilized for data fitting in order to further reduce computation durations. (See Appendix for codes.)

Table 3-1: Comparison of experimental and simulation results for 2 to 16 channel arrays

Number of Channels	Measured Combining Efficiency	Calculated Efficiency
2	0.98±1.5%	0.997
4	0.963±2%,	0.974
6	0.913± 2.5%	0.94
8	0.831±10%,	0.89
10	0.816±8%	0.81
12	0.752±12%	0.74
14	0.665±16.75%	0.662
16	0.542±27.5%	0.527

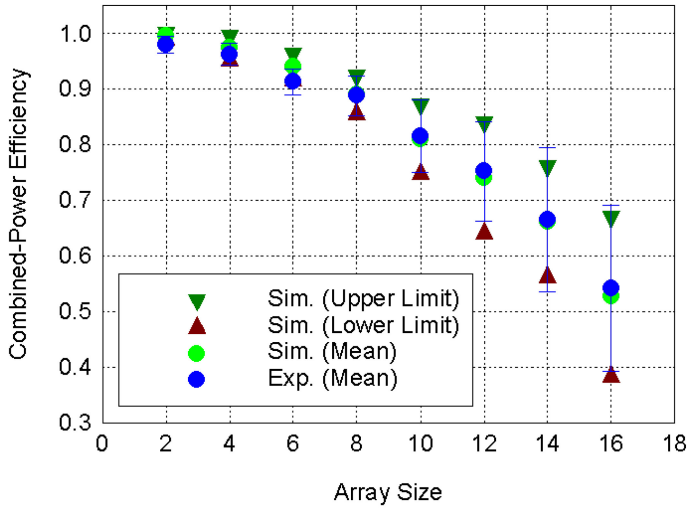

Figure 3.3: Combined-power efficiency and power fluctuation (error bars for experimental results) versus fiber array size.

In fitting the theoretical calculations to the experiment, we had to account for the fact that the individual fiber lengths are not precisely known, as a result of occasional fiber

breakage during assembly and splicing and connector uncertainties. We estimate an uncertainty of about 2% in the nominal lengths of the individual fiber amplifier channels. In the simulation, for a given number *N* of amplifying channels, a set of lengths *N* were randomly generated that varied within 2% of the nominal length. The simulated combining efficiency is the mean of several realizations of length distributions. From Figure 3.3, the simulated and experimental results agree very well and both of them indicate a clear evolution of combined-power efficiency with array size: power combining efficiency decreases monotonically with array size. The drop of combining efficiency means that the power of individual fiber lasers is not always coherently combined at the straight-cleaved end with a null at the angle-cleaved end. The decrease in combining efficiency reflects the difficulty in finding congruencies among the frequency combs of the individual resonators that make up the overall interferometric cavity laser. Angle-cleaved ends, even if they have large loss at first, may have chance to exhibit resonant modes with the minimum loss. From Figure 3.3 it can be seen that the practically useful maximum number of laser channels that can be coherently combined in this manner is approximately 10-12 [57].

3.2.2 **Power fluctuation**

The output of the coherently combined fiber laser array exhibits significant power fluctuations on a time scale of microsecond. These fluctuations are due to environmental factors such as temperature and pressure changes, the interferometric nature of the fiber array resulting in an efficient sensor for these changes. In Figure 3.3, the measured power fluctuation, indicated by the experimental error bars, is seen to increase with array size. Here,

$$\text{Relative power fluctuation (\%)} = \frac{3\sigma}{P_{out}} \qquad (3.2)$$

where σ denotes the statistical standard deviation. The extent of ±3σ includes approximately the maximum range of power fluctuation.

To simulate the power fluctuations we assume that environmental factors lead to length changes on the order of a wavelength for each channel, or, equivalently, a phase shift of 2π. Given the microsecond time scale of the experimental fluctuations, we let the length of each fiber increase by 0.8nm per round trip so that after about 1250 roundtrips a length change of about one wavelength has accumulated. The power value per round trip is recorded until several thousand round trips later the overall accumulation of phase shift has reached 2π (~1μm), then all recorded power values are statistically analyzed to attain the aforementioned definition of power fluctuation range (±3σ). From Figure 3.3, the statistical simulation results, using the upper (downward triangles) and lower (upward triangles) limits to represent the maximum and minimum of calculated power combining efficiency, indicate that the fluctuation ranges increase with the increasing array size and they agree well with similar power fluctuation values in experiments. The results indicate that small fluctuations in fiber length can result in substantial power instabilities and fluctuations, especially for arrays with a large number of elements.

To further explore how the rate of fluctuation relates to array size, we plot in Figure 3.4 the experimental (blue dots) and simulation (red squares) fluctuations versus number of channels in the array, *N*. We find that the power fluctuations scale with array size as N^3 (green fitting line). This scaling behavior of power fluctuations in coherent beam combining has never been reported. We do not yet have a simple explanation for this cubic dependence on array size but we note that N^3 seems to describe the product of a

coherent process (scaling as N^2) and an incoherent process (scaling as N). This rapid growth of fluctuations with arrays size is one of the factors that may limit the scalability of beam combining by passive coherent phasing.

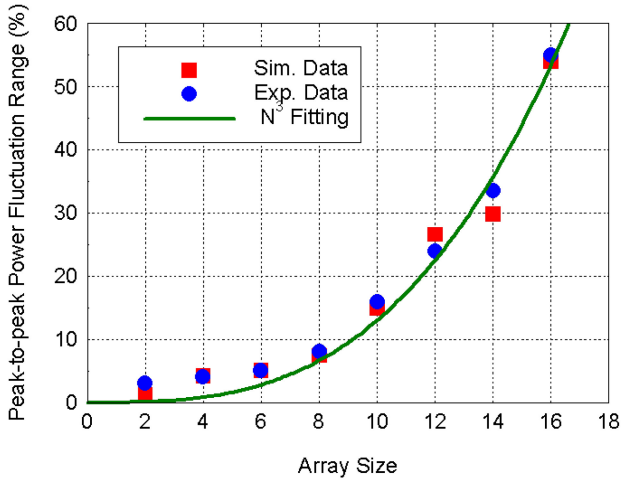

Figure 3.4: Peak-to-peak power fluctuation ranges versus array size from experiments, simulation, and N^3 fitting [42].

3.2.3 **Beat spectra**

The decline of power combining efficiency with array size believed to be a consequence of the increasing scarcity of coherently combined modes within the laser gain bandwidth. We investigate this scarcity by measuring and calculating beat spectra in fiber-laser arrays. To make it easier to observe beat spectra within the limited spectral bandwidth of an RF spectrometer, an additional 37.5-m single-mode fiber is inserted at the output-end and a 2-m single-mode fiber added to one arm of the fiber-laser array. The greater optical in-fiber length leads to a smaller mode separation of longitudinal modes, and thus more longitudinal modes are expected to exist and beat with each other in this composite cavity. The schematic is shown in Figure 3.5 as an example of 4-channel

combining. During measurements, a fast photodetector and a 1-GHz RF Spectrum Analyzer are used to detect beat spectra.

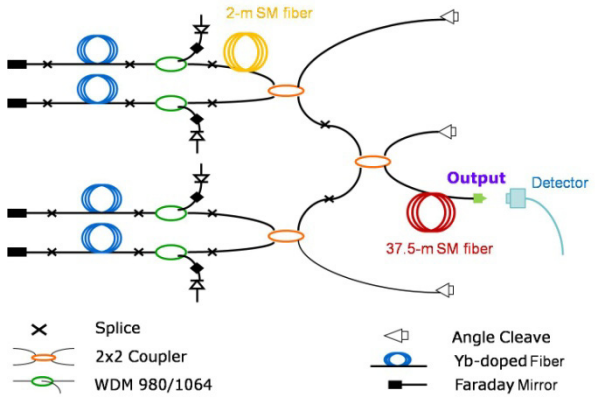

Figure 3.5: Experimental setup for beat spectrum measurements as an example of 4-channel combining.

According to 2-channel laser array theory, the free spectral range (FSR) of adjacent beat packets and mode separation (MS) of adjacent longitudinal modes are defined as $c/2/n/\Delta L$ and $c/2/n/L$. ΔL and L are the length difference and average length of laser array, respectively. In 2-channel beat spectra, the roughly 56 MHz FSR in Figure 3.6(a) and 2MHz MS in Figure 3.6(b) correspond very well to the theoretical calculations based on actual ~1.78-m in-fiber length difference and 46-m average length. In 4-channel spectra, ~2MHz MS in Fig. 6(d) is still observed but FSR is greatly increased up to 475-MHz in Fig. 6(c). The suppression of multiple beat packets in 2-channel to only one extra packet in 4-channel and zero extra packet in 8-channel or beyond within 1-GHz window directly indicates the number of the coherently-combined modes (supermodes) in the cavity is greatly reduced as array size multiplies, resulting in the drop of combined-power efficiency. In simulation, by selecting 2-channel in-fiber lengths as 47.82m and 46m; and 4-channel as 47.89m, 46m, 46.42m, and 46.21m, the calculated 2-channel beat spectrum

in Figure 3.7(a) exhibits multiple peaks whereas the 4-channel in Figure 3.7(b) has only one extra peak. These length parameters used for simulation here are quite arbitrarily assigned since the suppression of supermodes from 2-channel to larger channels always holds. Therefore, the simulation result supports the experimental conclusion that the increase in the number of elements in the array leads to a greater suppression of supermodes, resulting in the decrease of power combining efficiency with larger array number.

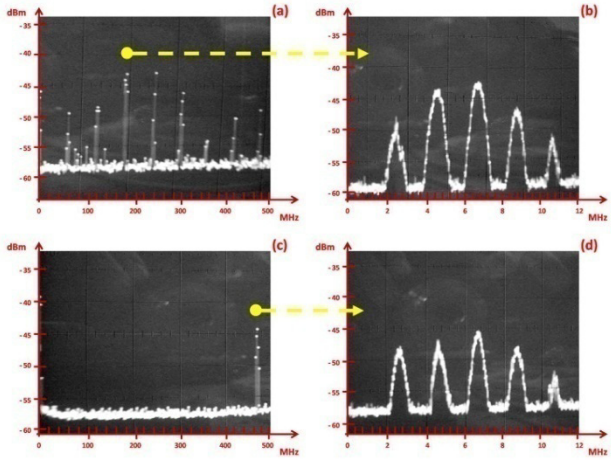

Figure 3.6: Beat spectra of 2-channel (a) and the zoom-in of designated envelope (b); and those of 4-channel (c) and the zoom-in of designated packet (d) [42].

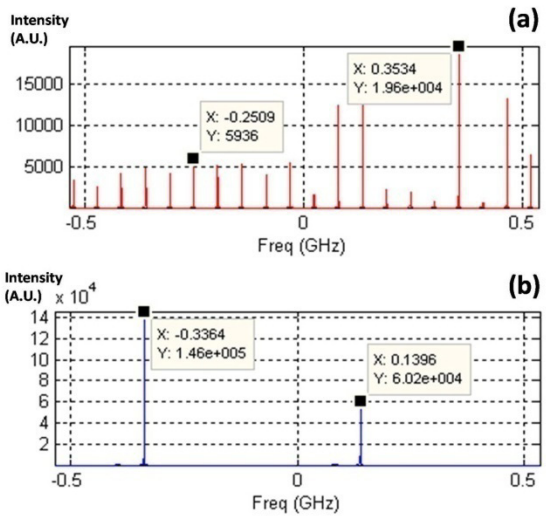

Figure 3.7: Simulation of beat spectra for 2-channel (a) with 47.82 and 46-m in-fiber lengths; and that of 4-channel (b) with 47.89, 46, 46.42, and 46.21-m in-fiber lengths.

3.3 Optical phase conjugation and combining efficiency

Drastic declines of combining efficiency in fiber laser arrays have been demonstrated both experimentally and theoretically up to 16 channels in the previous sections. Although not unexpected, in view of the earlier discussion of the array combining mechanism (CHAPTER II), the power scalability limitation still poses a serious problem in the development of high-power fiber coherent sources. The origin of the efficiency reduction is owing to incontrollable optical phase variations, therefore we turn our attentions to optical phase conjugation (OPC) in this section in an effort to bypass this obstruction.

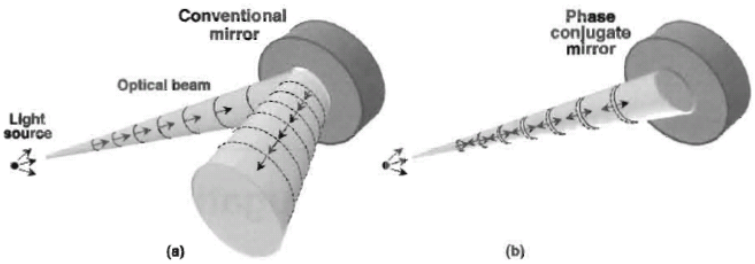

Figure 3.8: Illustration of difference between conventional mirrors and phase conjugate mirrors [Brignon, book].

Optical phase conjugation was discovered by Zel'dovich *et al* [66], Upatnieks and Leith [67] is a coherent nonlinear process with phase conjugate replicas of complex incident waves generated through holographic gratings. The well known distinction of the conventional mirror and OPC mirror is illustrated in Figure 3.8, where the reflected beam deflects away from incident waves under normal reflection law, while it retraces the incident optical path in the case of OPC mirrors. Based on its unique property, OPC has been utilized in many different areas including aberration correction for coherent-light transmission and reflection through disturbing media [68], dispersion compensation of long distance optical fiber communication links [69-71], wavefront correction in lasers/amplifiers for beam qualities improvement [72-75]. The technique also reaches the field of beam combining and phase locking of fiber laser arrays with diffractive combining configurations [6]. In this section, we investigate theoretically the application of OPC to coherent combining in passive fiber laser arrays and show its phase reversion property can fundamentally resolve the efficiency issue as array size increases.

We start with a fiber laser array of eight elements of lengths taken from #2 row of Table 2-2 because two and four channels have comparatively good combining efficiencies and the effects of OPC mirror is not discernible. To be clear, the OPC mirror

is taken to replace the fiber Bragg grating (FBG) in Figure 2.30 and it is realized mathematically by simply taking the backward propagating wave as complex conjugating the incident ones. The simulation results are shown in Figure 3.9 for (a) FBG, which works as conventional mirrors and (b) the OPC mirror. Total output powers of individual eight fiber lasers are 146.4 mW and the combining efficiencies are calculated to be 84.8% and ~ 100% respectively. Note in addition to the apparent raise of the combined output powers, two kinds of mirrors give rise to very different power spectrum. Figure 3.9(a) is well understood due to the interfereometric nature of the composite cavity, while the continuous and dense spectrum of Figure 3.9(b) resembles very much that of single fiber lasers in Figure 2.8. Since the length-dependent phase variations are canceled out during the roundtrip by the means of OPC mirrors, the collective fiber lasers act as a single oscillator and so combine indifferently. This simple simulation thus demonstrates the ultimate solution of OPC to coherent combining in passive fiber laser arrays.

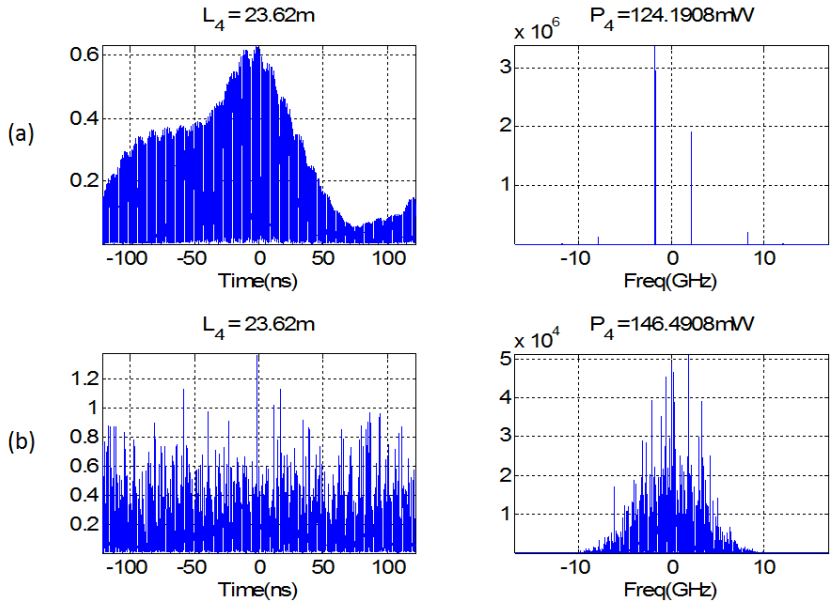

Figure 3.9: The simulation results for combined output power with (a) conventional mirrors (FBG) and (b) the OPC mirrors. The combining efficiencies are 84.8% and ~ 100% respectively.

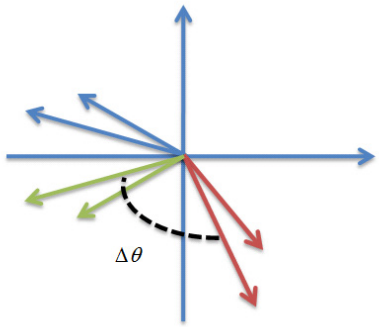

Figure 3.10: Phase diagram of absolute (green arrows) and relative (red arrows) phase conjugation.

In more general conditions, the phase conjugation may be relative in a sense that the relative phase difference between each fiber channel is preserved while their absolute values are not as shown in Figure 3.10. The blue rays indicate incident waves of each laser in front of OPC mirrors, and the green and red arrows illustrate absolute and relative phase conjugate waves. We are particularly curious if relative OPC could combine array and maintain its output stabilities since the phase variations introduced by relative OPC ($\Delta\theta$ in Figure 3.10) may disrupts the roundtrip phase integrity of 2π. However, the simulation results suggest that highly efficient combining is still obtained with relative OPC and realization of phase conjugation in fiber laser arrays is a promising direction for future investigations.

3.4 Discussion and conclusion

The most important question associated with passive coherent phasing of fiber-laser array is how the coherent-combing efficiency is scaling with the array size. In this paper,

we have studied the detailed evolution of combined-power efficiency and the issue of power fluctuation versus array size from 2 to 16-channel passively coherently combined fiber-laser arrays.

For power combining efficiency, good agreement between our new simulation model and experiments is demonstrated for arrays containing up to 16 channels. Small phase shifts resulting from wavelength-scale length variations are verified numerically to be an important factor resulting in fluctuations and instability in output power. The power fluctuations scale with array size as N^3. Investigation of array beat spectra supports the notion that the decrease of power combining efficiency with array size is a result of increasing scarcity of composite-cavity supermodes.

We also numerically verify the highly efficient combining of fiber laser arrays independent of array sizes or fiber length variations when optical phase conjugation mirrors are applied. We found that even for relaxed phase conjugation reflections, the array combines definitely and OPC is a promising technique for further investigations.

CHAPTER IV

Raman fiber laser arrays

4

4.1 Introduction

The increasing demands for high-power coherent sources with single-mode beam quality have given rise to intensive investigations of fiber laser arrays. Several groups have demonstrated highly efficient coherent combing up to 200 W with discretely coupled laser arrays, but in all these studies, the gain required for laser action has been provided by an inverted population of pumped erbium or ytterbium ions. Other types of rare-earth doping materials such as Nd [76], Sr [77], Pr [78], Tm [79] are available for emitting broader range of radiation from 1064nm (Yb) to 2μm (Tm), however, the working wavelengths of these fiber lasers strongly depend on the electronic transition level of specific atoms and the tunability is very limited.

Stimulated Raman scattering (SRS), on the other hand, is a well-known nonlinear process that is capable of amplifying optical signals or generating new wavelengths, especially for those not accessible from rare-earth doped fiber lasers. Although single Raman fiber lasers have no problems producing large Stokes output powers, they may suffer from serious spectral broadening for high pump powers [80]. The broadening depends on pump power level and the spectral width only remains narrow at low pump or near threshold [81]. The demands of narrow-linewidth or single-frequency fiber lasers,

primarily used for sensing and frequency doubling, have led to extensive studies on intracavity spectral filtering methods involving fiber Bragg gratings and nonlinear loop mirrors [82-84]. Another problem associated with high power single Raman lasers is the cascade process of wavelength conversions, i.e. higher order Stokes lines can appear at high pump powers when the first order Stokes power becomes large enough to pump the next-order Stokes line. Therefore, in this chapter we propose fiber laser arrays based on Raman gain as high-power coherent sources with good beam quality at wavelengths inaccessible by rare-earth doped fiber lasers. The hope is that by operating each Raman laser in the array at a relatively low power, undesirable spectral broadening may be reduced while yielding a high combined output power. Furthermore, the spectral filtering effect that accompanies interferometric beam combining might result in a Raman laser array with reduced linewidth. We find that under single-longitudinal-mode operation, the intrinsic nonlinear coefficient n_2 that comes with SRS directly accounts for the transition of the array output to a phase-locked state. As the pump power is increased, the output changes from anti-phase or bi-stable states to in-phase states, depending on the coupling strength. More realistic condition of Raman fiber laser arrays under multi-mode operation is also analyzed and discussed.

4.2 Single mode Raman fiber laser arrays

Figure 4.1 depicts two independent single mode fibers coupled discretely by a directional coupler. Individual cw pump beams are launched into each fiber by a wavelength division multiplexer (WDM) at $z = 0$ and give rise to gain at a longer (Stokes) wavelength in the fused silica fiber. The mirrors at the far right end are wavelength-selective and provide feedback only for the Stokes waves. Since the two

Raman fiber lasers are essentially separated from each other (no distributed coupling), the equations governing the stimulated Raman scattering process in one laser are:

$$\frac{\partial A_p}{\partial z} = -\frac{g_p}{2}(|A_f|^2 + |A_b|^2)A_p + i\gamma_p(|A_p|^2 + 2|A_f|^2 + 2|A_b|^2)A_p - \frac{\alpha}{2}A_p \tag{3.3}$$

$$\frac{\partial A_f}{\partial z} = \frac{g_s}{2}|A_p|^2 A_f + i\gamma_s(2|A_p|^2 + |A_f|^2 + 2|A_b|^2)A_f - \frac{\alpha}{2}A_f \tag{3.4}$$

$$\frac{\partial A_b}{\partial z} = -\frac{g_s}{2}|A_p|^2 A_b - i\gamma_s(2|A_p|^2 + 2|A_f|^2 + |A_b|^2)A_b + \frac{\alpha}{2}A_b \tag{3.5}$$

A_p, A_f and A_b refer to the amplitudes of the pump wave, forward Stokes wave and the backward Stokes wave. The first terms on the right side of the equations describe the nonlinear stimulated process that couples three waves together in magnitude. The second terms describe the self- and cross-phase modulation effects due to the nonlinear index. The constants g_s and γ_s are Raman gain coefficients and nonlinear phase coefficients with $g_p = g_s \lambda_s / \lambda_p$ and $\gamma_p = \gamma_s \lambda_s / \lambda_p$. The third terms are linear absorption in the fiber medium, and we have assumed absorption coefficient α to be identical for the three waves. The amplitudes are normalized such that that $|A_p|^2$, $|A_f|^2$ and $|A_b|^2$ represent pump, forward and backward Stokes power distributions.

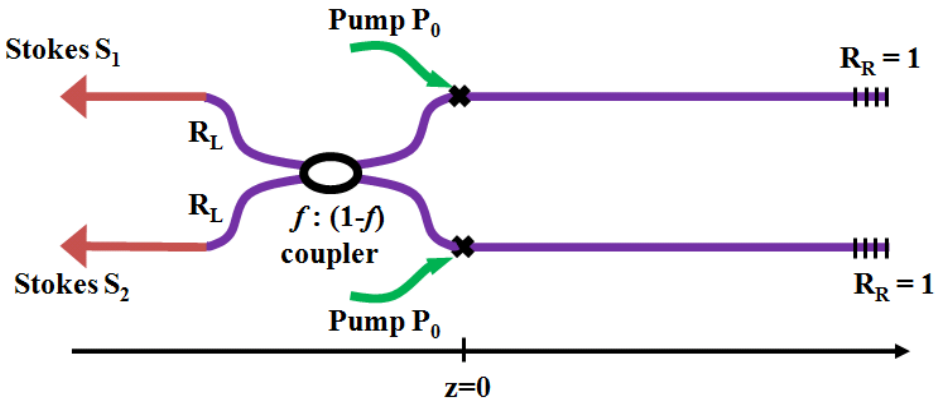

Figure 4.1: a Raman fiber laser array structure

Eq. (3.3)-(3.5) can be separated into amplitude and phase equations by setting $P_p = A_p A_p^*$, $A_f = F\exp(i\phi_f)$ and $A_b = B\exp(i\phi_b)$. The resulting equations are:

$$\frac{\partial P_p}{\partial z} = -g_p(F^2 + B^2)P_p - \alpha P_p \tag{3.6}$$

$$\frac{\partial F}{\partial z} = \frac{g_s}{2}P_p F - \frac{\alpha}{2}F \tag{3.7}$$

$$\frac{\partial B}{\partial z} = -\frac{g_s}{2}P_p B + \frac{\alpha}{2}B \tag{3.8}$$

and

$$\frac{\partial \phi_f}{\partial z} = \gamma_s(2P_p + F^2 + 2B^2) \tag{3.9}$$

$$\frac{\partial \phi_b}{\partial z} = -\gamma_s(2P_p + 2F^2 + B^2) \tag{3.10}$$

For a single Raman fiber laser, the equations for pump power P_p and Stokes wave magnitudes F, B are decoupled from phase terms ϕ_f and ϕ_b. Eqs. (3.6)-(3.8) can then

be readily solved for the backward Stokes wave B at $z=0$ with given boundary conditions $P_p(z=0)=P_0$, $B(z=L)=F(z=L)$ and known $F(z=0)$. L is the length of the fiber and P_0 is the amount of power coupled into the fiber as indicated in Figure 4.1. Once the distribution of three waves are obtained, the phase of the returning stokes wave $\phi_b(z=0)$ is calculated numerically by integrating Eqs. (3.9) and (3.10). We get

$$\phi_b(z=0)=\phi_f(z=0)+\int_0^L[4P_p(z)+3B^2(z)+3F^2(z)]dz+\pi \tag{3.11}$$

where the π phase shift is due to the perfect reflection at the right end mirrors.

To complete one roundtrip, the backward Stokes waves at $z=0$ with acquired phase ϕ_b pass through the directional coupler, undergo reflection at the left end mirror and then pass through the directional coupler again. The equation connecting the inputs E_1, E_2 and outputs E_3, E_4 of a $f:(1-f)$ coupler is

$$\begin{aligned} E_3 &= \sqrt{f}E_1 - i\sqrt{1-f}E_2 \\ E_4 &= -i\sqrt{1-f}E_1 + \sqrt{f}E_2 \end{aligned} \tag{3.12}$$

Eqs. (3.6)-(3.12) are solved numerically and iteratively [85] to model the laser behaviors of this composite cavity with phase evolutions included. A similar scheme has been used previously to study rare-earth doped fiber laser arrays [22]. After a number of roundtrips, the steady-state is reached when there are no differences between longitudinal field distributions obtained in consecutive roundtrips.

We first verify the buildup of a single Raman fiber laser. Taking parameters appropriate for standard SMFs, Raman fiber lasers are simulated with $L=1000m$ for two cases: left end mirror $R_L=0.16$ and $R_L=0.04$. The right ends of both single lasers is

chosen to have perfect reflection $R_R = 1$. The pump wavelength are $\lambda_p = 1.45\mu m$ and the Stokes wavelength is $\lambda_s = 1.55\mu m$. We assume small $\alpha = 0.2dB/m$ since λ_s and λ_p lie within the low loss bandwidth. The Raman gain constant is defined by $g_s = g_R / A_{eff}$ and $g_R = 0.7\times10^{-13} m/W$. The effective mode area is $A_{eff} = 50\mu m^2$, nonlinear index constant is $n_2 = 3.2\times10^{-20} m^2/W$, and γ_s in Eqs. (3.3)-(3.5) is related to n_2 by $\gamma_s = 2\pi \times n_2 / \lambda_s / A_{eff}$. The output stokes power versus pump power P_0 is shown in Figure 4.2(a). The lasing threshold can be calculated by $P_{th} = (\alpha / g_s)(\alpha L - (1/2)\ln(R_1 R_2))/(1-\exp(-\alpha L))$ [86]. Figure 4.2(b) shows the output power versus roundtrip (time) as the pump powers are fixed at 0.8W and 1.3W respectively. Note that small random numbers representing spontaneous Raman scattering noise on the order of nanowatt are included for each roundtrip to initialize the lasing process.

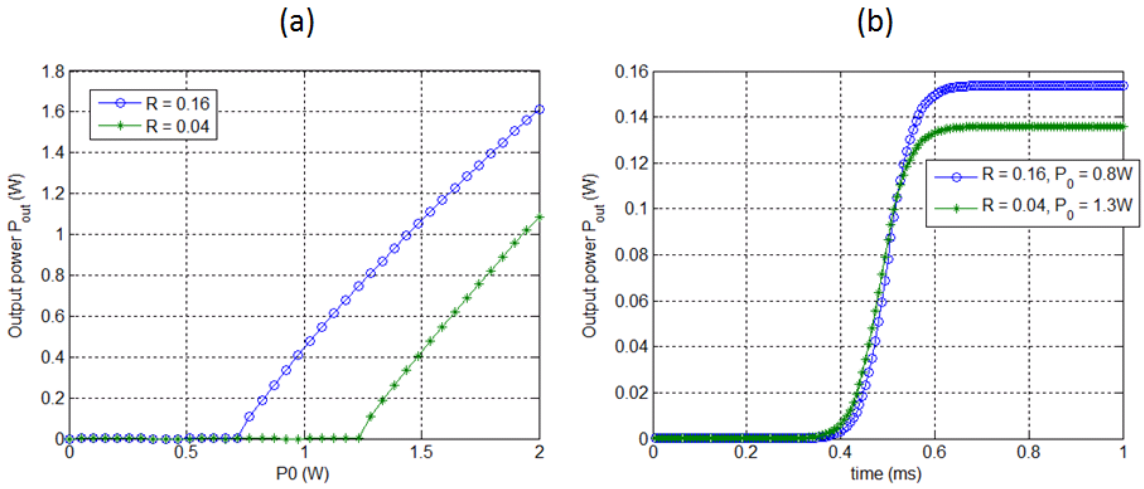

Figure 4.2: (a) Output Stokes power v.s. input pump power and (b) Output Stokes power v.s time in milliseconds

For array simulations, two fibers of equal lengths are assumed in Figure 4.1. The pump powers P_0 are also taken to be identical in the ideal case. Extensive studies of the structures containing feedback and nonlinearities have shown that they tend to be unstable and reach steady states only for weak coupling between forward and backward waves and at low input intensities [87]. In strong coupling regime, very rich dynamics could be exhibited including periodic pulsation, aperiodic pulsation, and chaos [88, 89]. In this section, we assume small coupling coefficients for the coupler and emphasize the phase-locking behavior of the Raman fiber laser arrays.

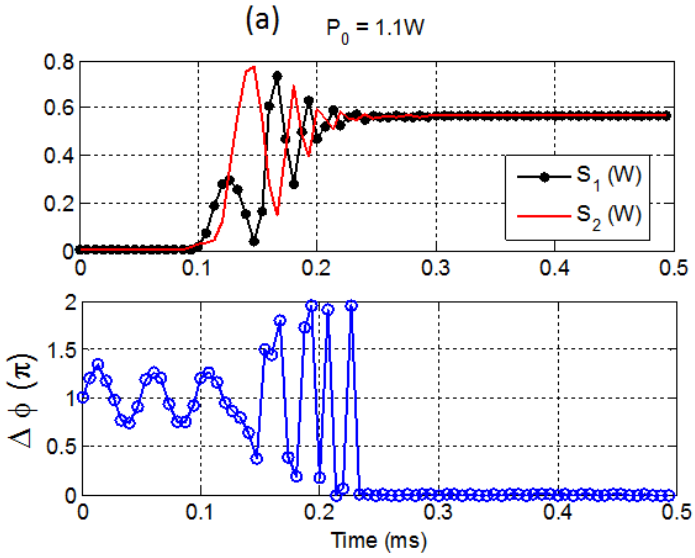

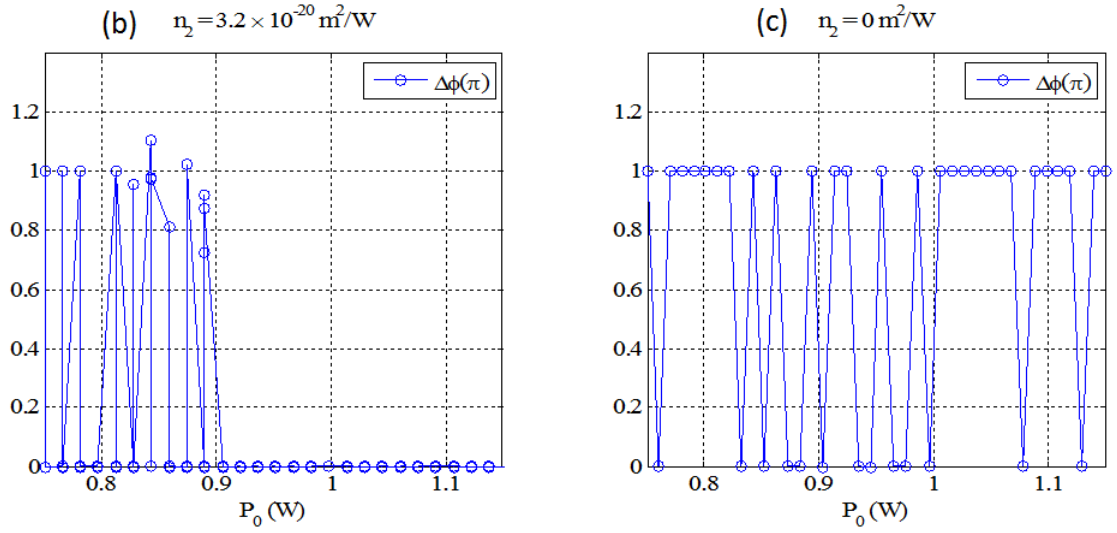

Figure 4.3: f = 0.95, R = 0.16, L = 1000m. (a) Stokes powers and $\Delta\varphi$ (π) evolution v.s. time as P_0 = 1.1W for n_2 = 3.2 × 10^{-20} m^2/W. Steady states $\Delta\varphi$ (π) v.s. pump power P_0 (W) are plotted in (b) for n_2 = 3.2 × 10^{-20} m^2/W and in (c) for n_2 = 0 m^2/W.

Figure 4.3(a) shows the Raman laser array output (Stokes) power and phase evolution versus time when pump power is fixed at 1.1W for $f = 0.95$, $R = 0.16$ and $L = 1000m$. The desired in-phase array mode is obtained at steady state. In order to investigate the stability of this phase-locked phenomenon, numerous simulations have been performed for different initial conditions with noise perturbations included in every roundtrip. At extreme cases, $\Delta\varphi_0 = \pi$ was given to start the array as seen in lower plot of Figure 4.3(a). The results show that the in-phase operation is robust and insensitive to initial conditions. In addition, $\Delta\varphi$ is observed to associate with the amount of pump power coupled into the fiber. For low power levels close to threshold P_{th}, $\Delta\varphi$ can be either 0 or π at steady state. Higher pump powers alter $\Delta\varphi$ and lead to in-phase array modes eventually. Figure 4.3(b) shows such results.

The origin of the connection between powers and phases is the Kerr nonlinearity that is intrinsic in stimulated Raman amplification. For arrays with $n_2 = 0$ or sufficiently small, we find that the output phase is not predictable and depends on random initial conditions as illustrated in Figure 4.3(c). If, on the other hand, n_2 is taken to be the nominal value of SMFs, it is found there is some range over which $\Delta\varphi$ can be regulated by the pump power as described before. The relation between controlling range and coupling strength is further investigated in Figure 4.4 which shows laser array behavior for extremely weak coupling conditions: $f = 0.999$, $R = 0.04$ and $L = 1000m$. As P_0 is increased from its threshold value, the array $\Delta\varphi$ changes from anti-phase to bi-stable and in-phase states. Hence weak coupling and low power lead to anti-phase states while weak coupling and high power lead to in-phase states. The role of intensity-dependent refractive index is apparent by setting n_2 to zero in Figure 4.4(b). Here it is seen that the phase becomes sensitively dependent on initial conditions.

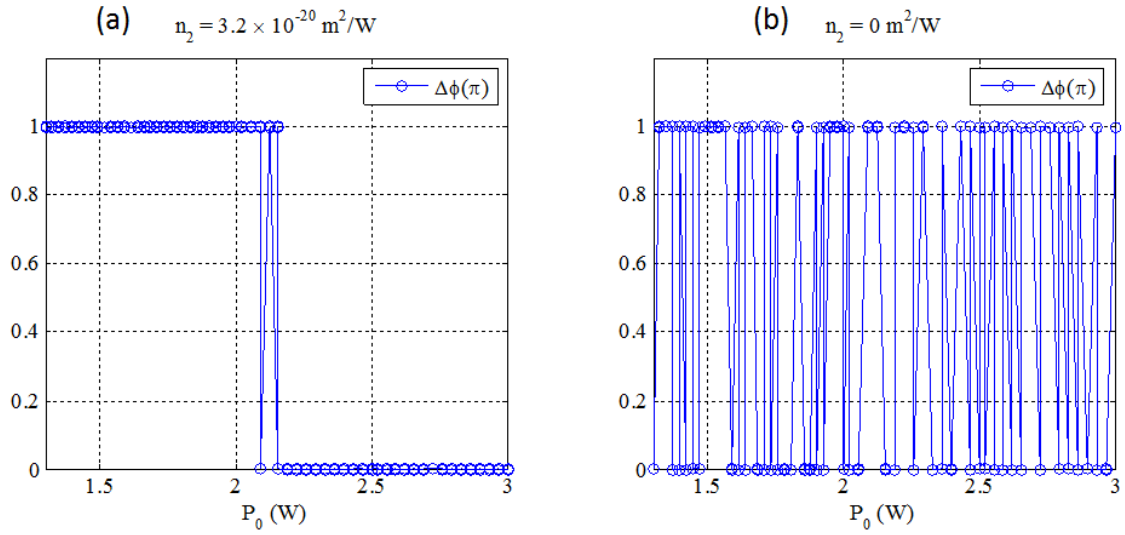

Figure 4.4: $f = 0.999$, $R = 0.04$ and $L = 1000$m, (a) $n_2 = 3.2 \times 10^{-20}$ m^2/W, (b) $n_2 = 0$ m^2/W

The transition region, where both anti-phase and in-phase states exist, is proportional to the coupling strength. Larger coupling coefficient will lead to broader transition regions. For even larger coupling strength and high input powers, steady states disappear and chaotic pulsations are observed. Figure 4.5 shows array outputs for a 90:10 directional coupler ($f = 0.9$), $R = 0.04$ and high pump power $P_0 = 4.5W$ as $L = 1000m$. Random and irregular pulsations with large fluctuations are observed. With higher cavity reflectivity chaos is seen at even lower values of pump power. For example, only $P_0 = 500\,mW$ is needed to initiate chaos for a Raman fiber laser array using the same parameters as Figure 4.5 but with reflectivity $R = 0.64$.

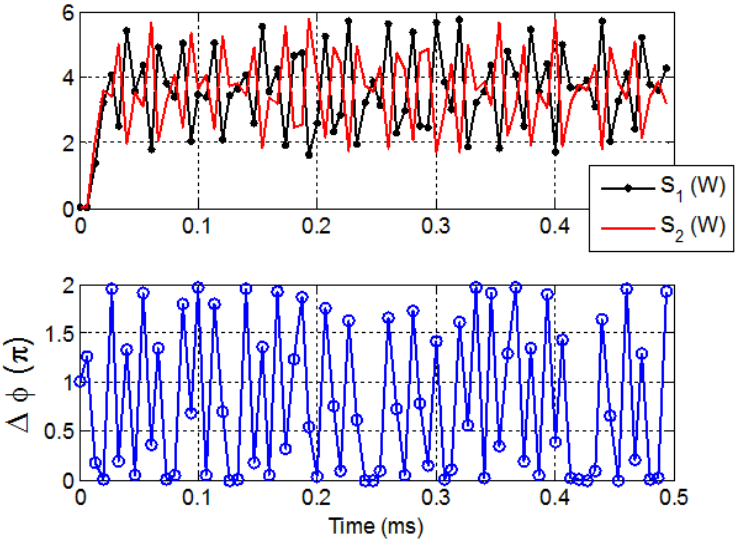

Figure 4.5: chaotic array outputs due to large coupling strength and high pump power. Simulation parameters: $f = 0.9$, $R = 0.04$, $L = 1000$m and $P_0 = 4.5$W.

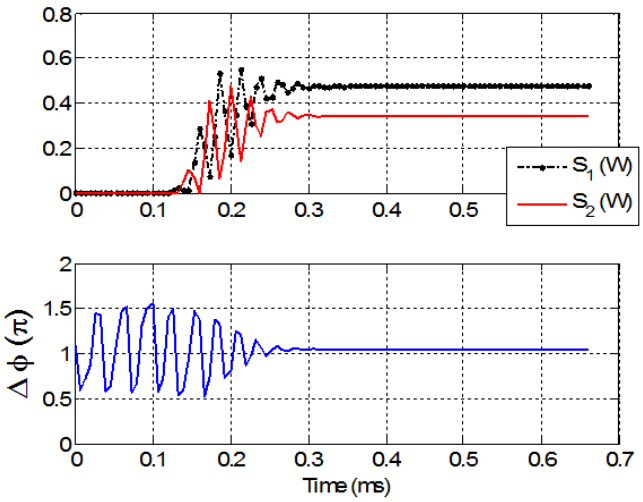

Figure 4.6: A Raman fiber laser array with uneven fiber lengths such that $L_1 = 1000$m, $L_2 = 1001$m and $P_0 = 1.5$W. Refer other parameters to that of Figure 4.4(a).

In more general conditions of uneven fiber lengths, the Raman fiber laser array is also simulated with a fiber length mismatch of 1m, i.e. $L_1 = 1000$m and $L_2 = 1001$m. Refer other parameters to Figure 4.4(a). Figure 4.6 shows such simulation results at $P_0 =$

1.5W. Note the phase locking is still obtained in spite of the length mismatch, however, the steady state $\Delta\phi$ deviates from π slightly and the Stokes output powers are unbalanced due to the asymmetry of the array structure.

It is interesting to further examine the array performance for even larger coupling strengths. Considering the same parameters as specified in Figure 4.5, we simulate the Raman fiber laser arrays with the 50:50 directional coupler (f = 0.5.) The simulation results are shown in Figure 4.7 for (a) P_0 = 1.5 W and (b) P_0 = 4.5 W. In contrast to the steady states or chaotic behaviors, the array now exhibits periodic oscillations on two Stokes outputs as well as their relative phase difference.

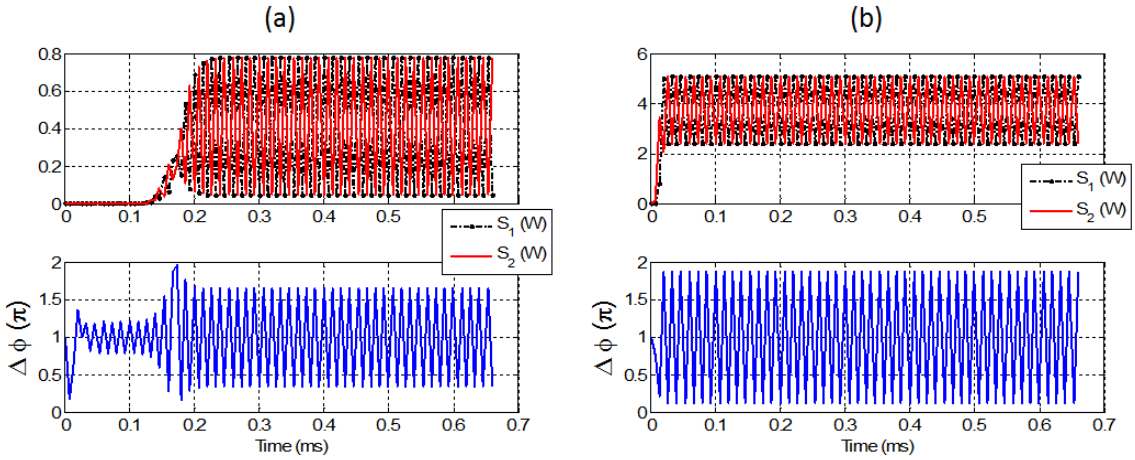

Figure 4.7: The performance of a Raman fiber laser array with L = 1000 m, R = 0.04 and 50:50 coupler (f = 0.5) for (a) P_0 = 1.5 W and (b) P_0 = 4.5W.

4.2.1 **Switching**

Based on Figure 4.4(a), we also study the switching property of the Raman fiber laser array by adjusting the pump power level below or above the transition range. Using same parameters as that of Figure 4.4(a), the array is designed to be pumped with P_0 = 1.8 W for the first 500 roundtrips and higher P_0 = 2.4 W for the rest. The simulation

results are shown in Figure 4.8 and it is interesting to see that the relative phase difference $\Delta\phi$ changes from π to 0 according to different pump power level as desired. Note although Stokes output powers increase instantly at the 500th roundtrip, the phase transition is delayed for about 200 roundtrips. The non-instantaneous response is sometimes limiting the switching speed and thus we increase the pumping power from 2.4 W to 2.8 W for the second half of the 1000 roundtrips in Figure 4.9. In this case, a shorter delay of ~100 roundtrips is exhibited.

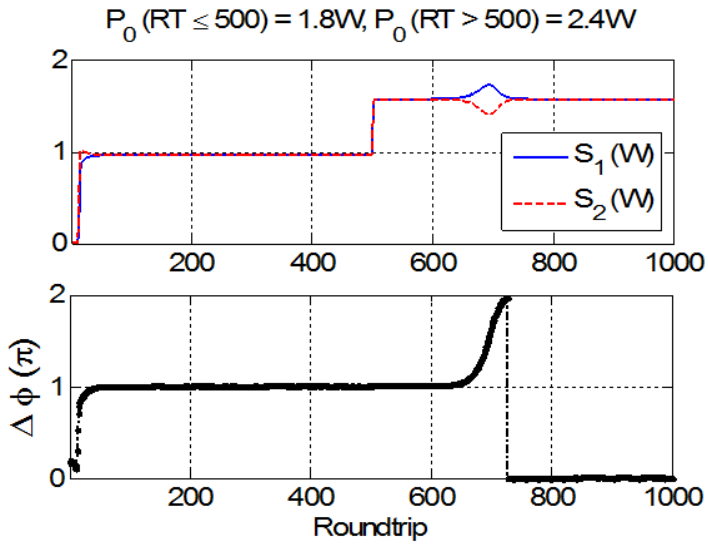

Figure 4.8: Switching of a Raman fiber laser array. Refer simulation parameters to Figure 4.4(a).

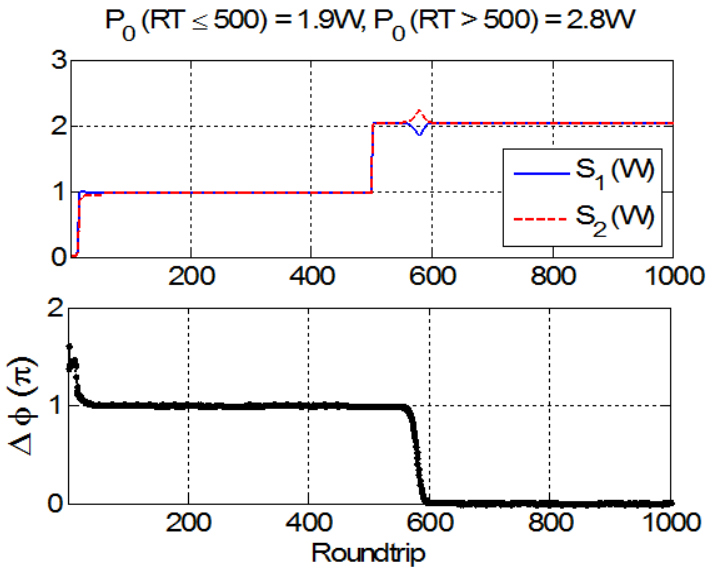

Figure 4.9: Shorter switching response is presented when the switching pump power is increased to 2.8W.

4.3 Multi mode Raman fiber laser arrays

As briefly mentioned in Sec. 4.1, Raman fiber lasers usually suffer from spectral broadening even in the presence of small bandwidth filtering components such as fiber Bragg gratings. The difficulties to maintain narrow-linewidth or single-mode operation of Raman fiber lasers urged us to conduct multi-longitudinal-mode analysis of Raman fiber laser arrays. In this section, we utilize the newly developed model of rare-earth doped fiber laser arrays from CHAPTER II for Raman counterparts in the unidirectional configurations. Since the presence of the backward propagating waves is not expected to affect the array performance (as demonstrated in Sec. 2.7), the ring cavity is adopted here for computation simplicity. Specifically, the coupled differential equations we solved for stimulated Raman scattering in each single-mode fiber are

$$\frac{\partial A_p}{\partial z} = -\frac{g_p}{2}\left|A_f\right|^2 A_p$$
$$\frac{\partial A_f}{\partial z} = \frac{g_s}{2}\left|A_p\right|^2 A_f + \frac{1}{2}b\frac{\partial^2 A_f}{\partial t^2} + i\gamma_s(2\left|A_p\right|^2 + \left|A_f\right|^2)A_f - \frac{\alpha}{2}A_f \quad (3.13)$$

A_p and A_f are the pump and stokes waves. We assume single mode pump but retain the time derivative term of the Stokes variable. Except the loss dispersion b ($1.3\text{ps}^2\text{m}^{-1}$), other parameters are the same as that of single mode analysis in Sec. 4.2. We firstly benchmark for the single Raman fiber laser. Instead of 1000 m, a fiber length of 100 m is considered in this case to reduce computation time and an output coupling coefficient of R = 0.64 is used for lowering the pump power level. The roundtrip evolutions of the pump and stokes intensities are plotted in Figure 4.10(a) (solid blue and dotted dash green lines) against the curves of the Matlab results obtained by the ODE solver (red circle and yellow asterisk) for P_0 = 3.7 W and they show reasonable agreement with each other. The temporal domain and power spectrum of the Stokes output are also shown in Figure 4.10(b). Note we use Matlab for obtaining steady states solutions of Eq. (3.13) (no time derivative terms), so the loss dispersion coefficient b is set to zero in Figure 4.10(a) and (b). By turning on b, outer spectral components experience higher losses and the total output power reduces from 2.2 W to 2.0 W as seen in Figure 4.10(c). In the presence of nonlinearity, the spectral width does not seem to be confined by the loss profile while the linear case with zero n_2 shows apparent parabolic shape in Figure 4.10(d) and an output power of 2.2 W.

We then continue to study such Raman fiber lasers arrays under weak coupling coefficient with f = 0.9 (See Eq. (3.12)). The temporal and spectral domains of one output field are exhibited in Figure 4.12(a) featuring random and irregular pulsations while the

relative phase difference spectrum of Figure 4.12(b) has no appearance of phase locking behaviors even with higher coupling strengths up to $f = 0.5$.

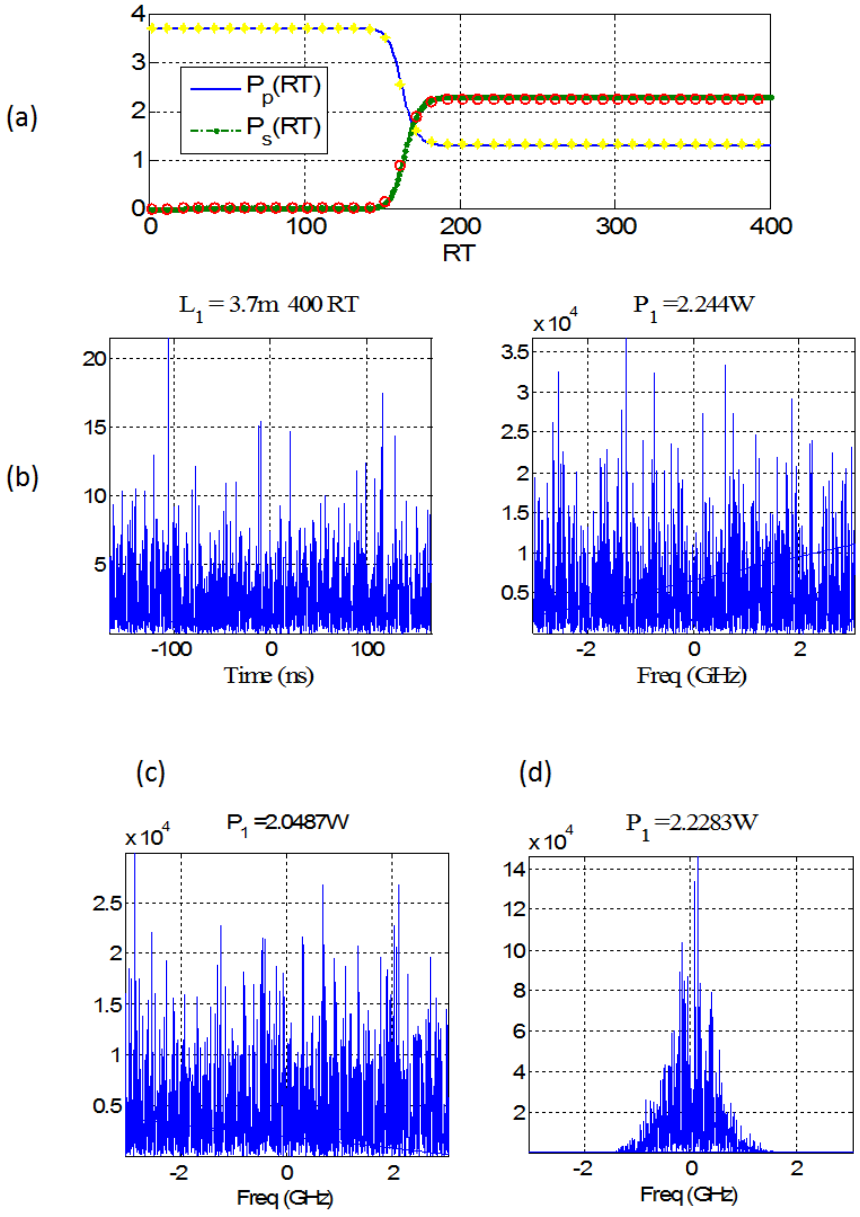

Figure 4.10: Benchmark of single Raman fiber laser with L = 100 m, P_0 = 3.7 W. Refer other parameters to Sec. 4.2. The roundtrip evolution of the pump and the Stokes power are shown in (a) and the temporal and spectral domain of the Stokes field in (b) with loss dispersion coefficient b set to zero. The power spectrum with b turned on is shown in (c) for nonlinear and in (d) for linear conditions.

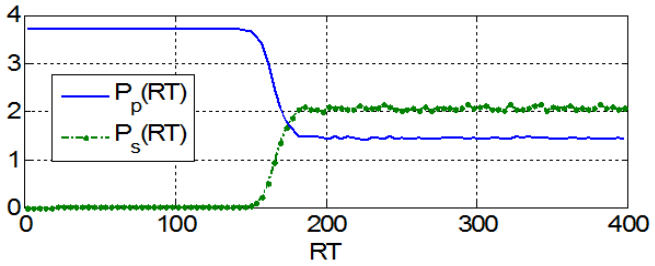

Figure 4.11: Raman fiber laser arrays with small coupling coefficient $f = 0.9$. Simulation parameters are used according to Figure 4.10.

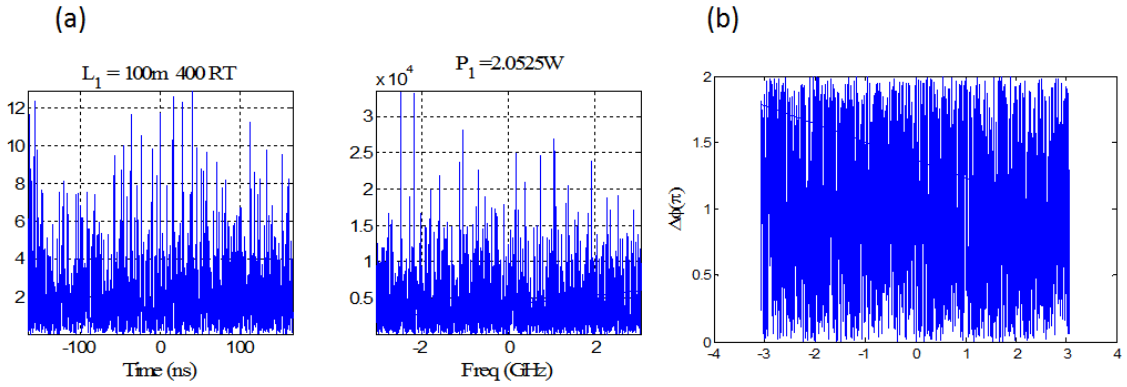

Figure 4.12: (a) Temporal and spectral domains of one output field from Raman fiber laser array with $f = 0.9$. (b) The relative phase $\Delta\phi$ spectrum between two outputs.

We also investigate the Raman fiber laser arrays in the coherent combining configurations with 50:50 directional couplers. Consider two single mode fibers of lengths 100 m and 101 m, their combining simulation results are shown in Figure 4.13. According to Figure 4.10, each fiber laser should produce a Stokes output power of around 2.2 W. However, with the presence of intrinsic nonlinearity the array gives about 0.9W and 0.5W for its two output ports and the combining efficiency is very low. The modulated power spectrum appears again due to the interferometric nature of the composite structure. The roundtrip evolution of both pump and the output Stokes powers

in Figure 4.14 further exhibits the fluctuation property of system. It is interesting to examine the role of n_2 by setting it to zero. In this case, highly effective combining is obtained in Figure 4.15, where a total output power of 4.4W emerges from the partially reflected port. The electronic Kerr nonlinearity is thus detrimental to coherent combining in discretely coupled fiber laser arrays and this conclusion is consistent with the results of Sec. 2.4.4.

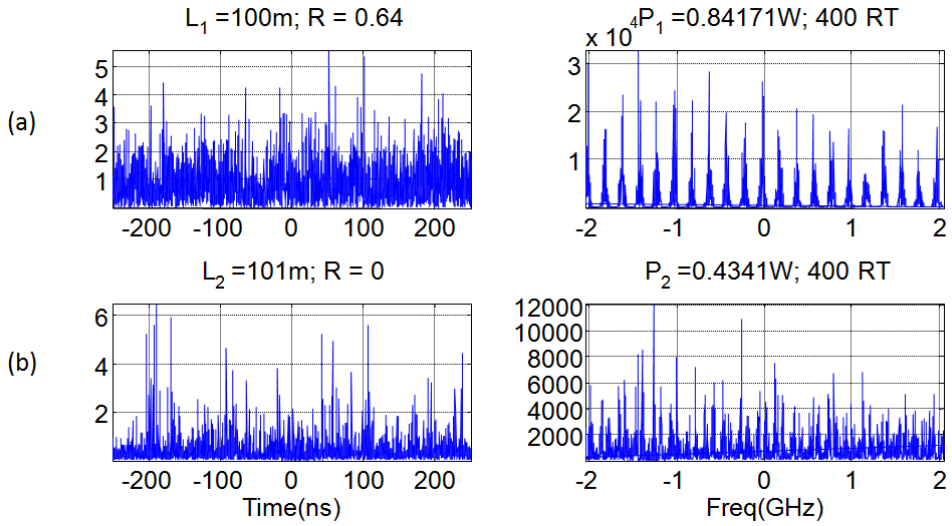

Figure 4.13: Coherent combining with Raman fiber laser arrays of (a) L_1 = 100m and (b) L_2 = 101m, Refer other simulation parameters to Figure 4.10.

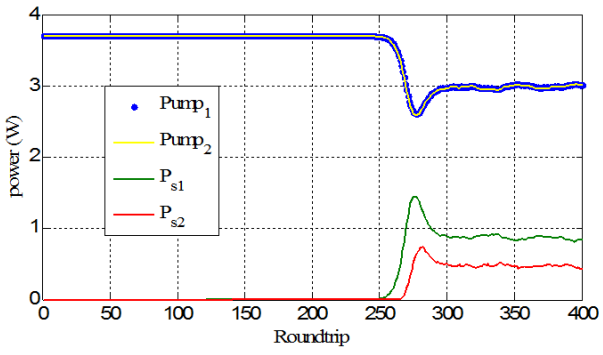

Figure 4.14: Roundtrip evolutions of the coherent combining in Figure 4.13.

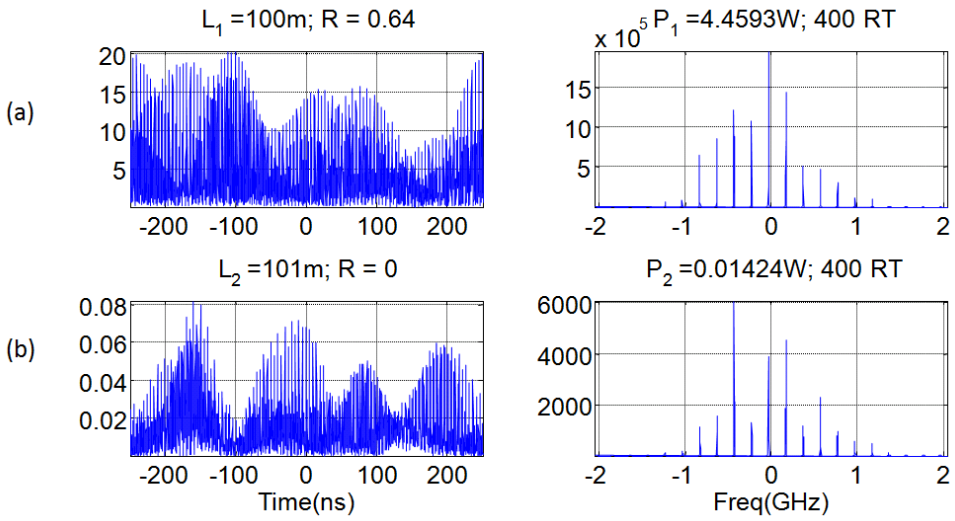

Figure 4.15: Repeat Figure 4.13 with n_2 set to zero

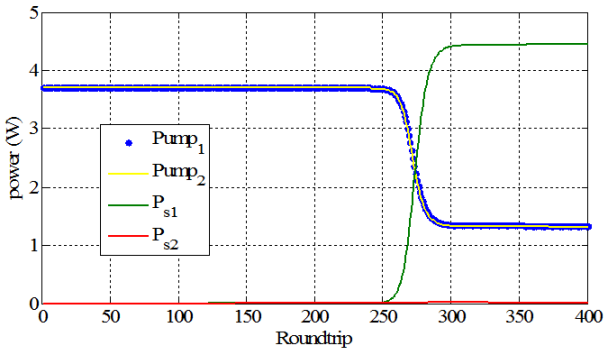

Figure 4.16: Roundtrip evolutions of the coherent combining in Figure 4.15.

4.4 Conclusion

In conclusion, we have proposed and analyzed Raman fiber laser arrays as high-power coherent sources with good beam quality, especially at wavelengths inaccessible by rare-earth doped fiber lasers. We find that under single-mode analysis small nonlinear phases from the Kerr nonlinearity are crucial to the phase-locking mechanism and aid in the steady-state selection by pump power level under the weak coupling regime. The multi-longitudinal-mode analysis of Raman fiber laser arrays is also carried out and the

phase-locking behavior is found to be disrupted due to the energy transfer between spectral components and is independent of coupling strengths.

CHAPTER V

Bend performance of leakage channel fibers

5

5.1 Introduction

Up to this point, the theoretical investigations of high power fiber laser sources with diffraction-limited beam qualities have been confined to discretely coupled fiber laser array structures for either beam combining (CHAPTER II and CHAPTER III) or diffractive combining (CHAPTER IV) configurations. Although initial power scaling can be obtained with some success using such scheme, the problem of reducing combining efficiencies, increasing instabilities and the fundamental limit of the absence of the coincidence modes with increasing array sizes remain inevitably as described in depth in the previous chapters. Toward this end, it is thus worthwhile taking different routes in the attempt to achieve high-power, high-brightness fiber sources. For this chapter, we are devoted to study the power scalability of microstructured large mode area (LMA) fibers, its complication of degrading beam qualities (introduced in Sec. 1.1) and also the coping strategy. Alongside the goal of achieving high power fiber laser sources, the development of large mode area fibers is important in a way that it can be incorporated into the passive coherent combining scheme as reported by Wang *et al* that an all-fiber passive laser array with large mode area polarization-maintaining fibers has been demonstrated successfully [56].

In this chapter, we introduce leakage channel fibers (LCF), a novel microstructured LMA fiber designed to exhibit additional propagation losses for higher order modes aiming to push the core size limit to 50 μm and beyond. We investigate the performance of LCF with different design parameters and further accurately analyze its bending losses at various bend radii. The implications of theoretical calculations are discussed and they are compared to experimental results with very good agreement with each other.

5.2 Leakage channel fibers

The cross section of a leakage channel fiber (LCF) and its relevant geometrical parameters are illustrated in Figure 5.1(a). A LCF consists of a ring of six circular inclusions embedded in a glass background with center-to-center hole spacing denoted by Λ, hole diameter by d and the core diameter by 2ρ. Simple calculation gives the relation $2\rho = 2\Lambda - d$. In general, the round holes can be filled with any dielectric as long as its refractive index is lower than that of the surrounding glass so as to ensure wave guiding property. One of the apparent features of LCFs is the broken boundary conditions of cores instead of the enclosed ones in the case of conventional step-index LMA fibers. Unlike fibers with intact contours where lossless propagation is supported for all eigenmodes, the leaky nature of LCFs enables the designs of a low confinement loss for fundamental mode while providing a high confinement loss for all higher order modes. Considering a LCF of 50 μm core diameter ($2\rho = 50$), the performances of first three groups of modes are evaluated at 1.05 μm wavelength in terms of the normalized hole diameter d/Λ. Their complex effective indices are plotted in Figure 5.1(b) indicating leakage loss (imaginary parts) and effective propagation constants (real parts) on the left and right ordinates respectively. Evidently, these modes are seen to experience an

increasing level of confinement loss starting from the fundamental mode with apparent mode filtering effects for all d/Λ that the desired SM operation may be achieved in LCFs even without any coiling or bends.

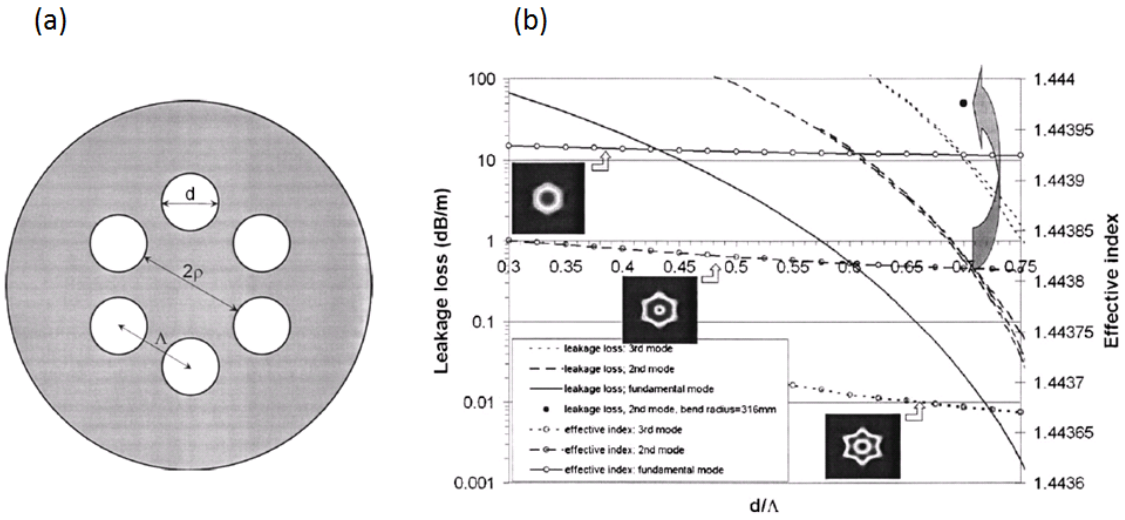

Figure 5.1: (a) Cross section of a LCF with its defining parameters. (b) The leakage losses of first three groups of modes are plotted in solid, dashed and dotted lines for a straight LCF of 50 μm core diameter at various d/Λ values. The wavelength is 1.05 μm.

One major advantage of LCFs is that large propagation loss of higher order modes originates from the fiber geometry and does not depend on any resonant effects as approached previously [90, 91]. This built-in mechanism is distributed along the fiber and makes the mode filtering of LCFs more robust and tolerant of process variations during manufacturing and use. Alongside the robust fundamental mode propagation, another unique feature of LCFs is that it can further provide much improved bend loss performance at comparable core diameters than that provided by photonic crystal fibers [92]. In a first demonstration few years ago, a passive LCF was shown to robustly propagate fundamental mode with an effective area of 1417 μm^2 [93]. Moreover it can be bent down to 6.7 cm bend radius without significant loss. Since then, robust singe mode

operation in ytterbium-doped leakage channel fibers with an effective area of 3160 μm^2 has been demonstrated [94]. Even at such large effective mode area, the leakage channel fiber can be coiled to a radius of 15 cm without significant excessive loss. Although mode analysis of straight LCFs has been studied in details within previous works [93, 94], there have been no systematic research on the bend performance of differential mode losses in LCFs which are only best fitted with an approximate bend loss formula [94] and its accuracy should be further verified. Therefore, considering the practical needs of LCFs for their abilities to expand peak power limit in developing fiber sources, it becomes critical and essential to understand differential bend loss of LCFs for performance optimization.

5.3 Theory: mode analysis in general curvilinear coordinate system

As discussed in length in the previous sections, the demand for stronger filtering effects between modes lands us on LCFs. The ideal situation would be the secure confinement of fundamental mode, while much larger leakage losses are introduced to high order ones. Along this direction, bending tolerance of fundamental mode propagation is also an important quality. We choose to study air-hole LCFs since large contrast of refractive index supports improved bend-resistant performances as mentioned in Sec. 1.1.2.

The problem in this analysis is how to accurately calculate bending losses of waveguide modes especially for those in the strongly guiding conditions. There are many theories in the literature existing to predict the curvature loss of optical waveguides [95-98]. However, all of them involve some approximations and assumptions to the scalar wave equations which limit the approach to either single mode or weakly guiding

waveguides. In order to accurately calculate the bend loss of LMA air-core LCFs, the full vectorial Maxwell equations must be solved without any simplifications. In regard to the complicated correlations between three-dimensional electrical and magnetic fields in vectorial equations, analytical results are sparse and we need to resort to the numerical computations.

One straightforward approach would be the beam propagation method or finite difference time domain method (FDTD) [99, 100], where monochromatic waves are launched into curved waveguides and, after certain distances, extracted at the output end for post-analysis. This type of method, however, directly solves three dimensional space that it is time consuming and inefficient, especially for LMA fibers since these optical waveguides usually span tens of wavelengths in the transverse directions and thus demand significant amounts of memory for discretization. In this case, the modal approach seems to be more reasonable and effective since it converts three-dimensional problems into two-dimensional ones through proper coordinate transformations. The propagation losses thus can be easily identified from the imaginary part of the complex effective refractive index if suitable absorbing boundary conditions, e.g. perfectly matched layers (PML), are incorporated into the computation domain. In this section, we derive and formulate the modal equations as well as that of PMLs in general curvilinear coordinate systems and apply them to study leaky modes of curved air-core LCFs through local cylindrical coordinate system (CCS) [101-103] for accurate and efficient bend analysis.

Under Cartesian coordinate system, the Maxwell equation in the $e^{j(\omega t - kz')}$ convention is well known as

$$\begin{aligned} \nabla \times \mathbf{E} &= -j\omega\mu_0\mu_r(x', y', z')\mathbf{H} \\ \nabla \times \mathbf{H} &= j\omega\varepsilon_0\varepsilon_r(x', y', z')\mathbf{E} \end{aligned} \tag{4.1}$$

where $\mathbf{E}$, $\mathbf{H}$ are electrical and magnetic fields in space, ε_0 and μ_0 refer to permittivity and permeability in vacuum. The relative permittivity $\varepsilon_r(x', y', z')$ and permeability $\mu_r(x', y', z')$ specify the waveguide geometry that for mode propagating along the z' direction $\varepsilon_r(x', y', z') = \varepsilon_r(x', y')$ and $\mu_r(x', y', z') = 1$ in general nonmagnetic materials. In theory, modes exist whenever it is a linear, time-invariant (frequency ω conserved) and z-invariant (wavenumber k conserved) system [MIT]. Therefore, here curved waveguides are mapped into local cylindrical coordinate system (CCS) since the transverse index profile of the waveguide does not change along the z direction as illustrated in Figure 5.2(a). A three-dimensional plot is also shown in Figure 5.2(b) for better visualization. We relate the Cartesian coordinate variables x', y', z' and the local cylindrical ones x, y, z through Eq. (4.2) for a bending radius of R.

$$\begin{cases} x' = x\cos(z/R) + R\cos(z/R) \\ y' = y \\ z' = x\sin(z/R) + R\sin(z/R) \end{cases} \tag{4.2}$$

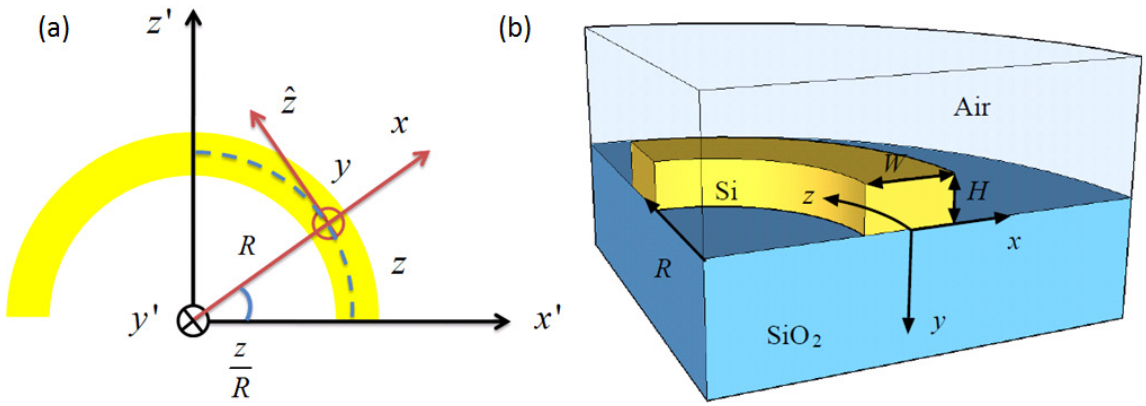

Figure 5.2: The local cylindrical coordinate and the Cartesian coordinate are specified in (a) for red and black lines with a bending radius of *R*. (b) Three-dimensional view from Ref. [102]

Utilizing the fact that the form of any Maxwell equation is preserved through coordinate transformation [Pendry], we can formulate the curl equations in local CCS as

$$\begin{aligned} \nabla \times \hat{\hat{\mathbf{E}}} &= -\mathrm{j}\omega\mu_0\mu_r \overline{\overline{\Lambda}}\mathbf{H} \\ \nabla \times \hat{\hat{\mathbf{H}}} &= \mathrm{j}\omega\varepsilon_0\varepsilon_r \overline{\overline{\Lambda}}\mathbf{E} \end{aligned} \tag{4.3}$$

with $\overline{\overline{\Lambda}}$ denoting a 3 × 3 matrix of spatial dependent components. Note that the differential operators in Eq. (4.3) exhibit same fashions to that of Eq. (4.1) except they now work on new coordinate variables and the definition of waveguide geometry changes simultaneously by $\overline{\overline{\Lambda}}$ on the right hand side. To proceed, we firstly calculate Jacobian and define its three columns as covariant basis vectors [Riley, book] with

$$J = \frac{\partial(x', y', z')}{\partial(x, y, z)} = (Q_1\hat{\mathbf{u}}_1\hat{}, Q_2\mathbf{u}_2, Q_3\mathbf{u}_3) \tag{4.4}$$

The basis vectors are used to compute $\overline{\overline{\Lambda}}$ according to Ref. [Pendry]

$$\overline{\overline{\Lambda}} = Q_1 Q_2 Q_3 \begin{pmatrix} \frac{g^{11}}{Q_1^2} & \frac{g^{12}}{Q_1 Q_2} & \frac{g^{13}}{Q_1 Q_3} \\ \frac{g^{21}}{Q_2 Q_1} & \frac{g^{22}}{Q_2^2} & \frac{g^{23}}{Q_2 Q_3} \\ \frac{g^{31}}{Q_3 Q_1} & \frac{g^{32}}{Q_3 Q_2} & \frac{g^{33}}{Q_3^2} \end{pmatrix} \tag{4.5}$$

by defining g as

$$g^{-1} = \begin{pmatrix} \hat{\mathbf{u}}_1 \hat{} \bullet \hat{\mathbf{u}}_1 \hat{} & \mathbf{u}_1 \bullet \mathbf{u}_2 & \mathbf{u}_1 \bullet \mathbf{u}_3 \\ \hat{\mathbf{u}}_2 \hat{} \bullet \hat{\mathbf{u}}_1 \hat{} & \mathbf{u}_2 \bullet \mathbf{u}_2 & \mathbf{u}_2 \bullet \mathbf{u}_3 \\ \hat{\mathbf{u}}_3 \hat{} \bullet \hat{\mathbf{u}}_1 \hat{} & \mathbf{u}_3 \bullet \mathbf{u}_2 & \mathbf{u}_3 \bullet \mathbf{u}_3 \end{pmatrix} \tag{4.6}$$

and new field vectors $\hat{\mathbf{\Phi}} = \hat{x} Q_1 \Phi_x + y Q_2 \Phi_y + \hat{z} Q_3 \Phi_z$ in which Φ represents E or H.

Plugging Eq. (4.2) into Eqs. (4.4)-(4.6), we get $Q_1 = Q_2 = 1$ and $Q_3(x) = 1 + x/R$. The Maxwell equation in local CCS then results to

$$\begin{bmatrix} \hat{x} \hat{} & y & \hat{z} \\ \frac{\partial}{\partial x} & \frac{\partial}{\partial y} & \frac{\partial}{\partial z} \\ E_x & E_y & Q_3 E_z \end{bmatrix} = -j\omega\mu_0\mu_r \begin{bmatrix} Q_3 & 0 & 0 \\ 0 & Q_3 & 0 \\ 0 & 0 & Q_3^{-1} \end{bmatrix} \begin{bmatrix} H_x \\ H_y \\ Q_3 H_z \end{bmatrix} \tag{4.7}$$

$$\begin{bmatrix} \hat{x} \hat{} & y & \hat{z} \\ \frac{\partial}{\partial x} & \frac{\partial}{\partial y} & \frac{\partial}{\partial z} \\ H_x & H_y & Q_3 H_z \end{bmatrix} = j\omega\varepsilon_0\varepsilon_r \begin{bmatrix} Q_3 & 0 & 0 \\ 0 & Q_3 & 0 \\ 0 & 0 & Q_3^{-1} \end{bmatrix} \begin{bmatrix} E_x \\ E_y \\ Q_3 E_z \end{bmatrix} \tag{4.8}$$

with $\hat{\mathbf{\Phi}} = \hat{x} \Phi_x + y \Phi_y + \hat{z} Q_3 \Phi_z$ for E or H. Note after transformation the material becomes highly inhomogeneous and even magnetically responsive. The problem of solving eigenmodes in curved waveguides thus can be considered as dealing with a waveguide of renormalized relative permittivity and permeability tensors by new position dependent variable $Q_3(x)$. This result makes huge simplification for numerical computations in a

sense that bending and moving to new coordinate systems are equivalent to simply reshaping the electric and magnetic properties of the waveguide materials and the same programming code under the Cartesian coordinate system can be applied without any modifications.

Next, since curved waveguides are essentially leaky, perfectly matched layers (PMLs) under local CCS are also critical in terms of truncating the open boundaries of computation region in order to accurately calculate the radiation loss. Here we briefly explain the derivation of PMLs by starting from the Maxwell equation in complex space through analytical continuation and then transforming it back into real space local CCS following the procedure described by Eqs. (4.4) to (4.6). Take the example of Eq. (4.7), in complex space it becomes

$$\begin{bmatrix} \hat{\tilde{x}} & \tilde{y} & \hat{\tilde{z}} \\ \dfrac{\partial}{\partial \tilde{x}} & \dfrac{\partial}{\partial \tilde{y}} & \dfrac{\partial}{\partial \tilde{z}} \\ E_x^c & E_y^c & \tilde{Q}_3 E_z^c \end{bmatrix} = -j\omega\mu_0\mu_r \begin{bmatrix} \tilde{Q}_3 & 0 & 0 \\ 0 & \tilde{Q}_3 & 0 \\ 0 & 0 & \tilde{Q}_3^{-1} \end{bmatrix} \begin{bmatrix} H_x^c \\ H_y^c \\ \tilde{Q}_3 H_z^c \end{bmatrix} \tag{4.9}$$

New coordinate variables $\tilde{x}, \tilde{y}, \tilde{z}$ are introduced by

$$\begin{cases} \tilde{x} = \int_{\zeta_0}^{x} s_x(\zeta)\, d\zeta \\ \tilde{y} = \int_{\zeta_0}^{y} s_y(\zeta)\, d\zeta \\ \tilde{z} = z \end{cases} \tag{4.10}$$

and

$$s_\kappa(\zeta) = 1 - j\sigma \frac{(\zeta - \zeta_0)^2}{L_{pml}^{\kappa}} \tag{4.11}$$

The notation κ can be x or y. L_{pml}^{κ} is the depth of the PML region, σ is the absorbing coefficient and ζ_0 is the PML interface in $\check{x}$ or $\check{y}$ directions respectively [101, 102]. Again the vector fields read as $\hat{\mathbf{\Phi}}^c = \hat{\tilde{x}}\hat{\Phi}_x^c + \tilde{y}\Phi_y^c + \hat{\tilde{z}}\tilde{Q}_3\Phi_z^c$. Recasting Eq. (4.9) into real space local CCS, the Jacobian is calculated to be [Kakihara]

$$J = \frac{\partial(\tilde{x}, \tilde{y}, \tilde{z})}{\partial(x, y, z)} = diag(s_x, s_y, 1) \tag{4.12}$$

based on Eq. (4.10) and so

$$\overline{\overline{\Lambda}} = diag(s_y / s_x, s_x / s_y, s_x s_y) \tag{4.13}$$

Finally PML formulation can be obtained for electric fields as

$$\begin{bmatrix} \hat{x} & y & \hat{z} \\ \dfrac{\partial}{\partial x} & \dfrac{\partial}{\partial y} & \dfrac{\partial}{\partial z} \\ s_x E_x^c & s_y E_y^c & \tilde{Q}_3 E_z^c \end{bmatrix} = -j\omega\mu_0\mu_r \begin{bmatrix} \tilde{Q}_3 & 0 & 0 \\ 0 & \tilde{Q}_3 & 0 \\ 0 & 0 & \tilde{Q}_3^{-1} \end{bmatrix} \begin{bmatrix} s_y / s_x & 0 & 0 \\ 0 & s_y / s_x & 0 \\ 0 & 0 & s_x s_y \end{bmatrix} \begin{bmatrix} s_x H_x^c \\ s_y H_y^c \\ \tilde{Q}_3 H_z^c \end{bmatrix} \tag{4.14}$$

Similarly, Eq. (4.8) turns into

$$\begin{bmatrix} \hat{x} & y & \hat{z} \\ \dfrac{\partial}{\partial x} & \dfrac{\partial}{\partial y} & \dfrac{\partial}{\partial z} \\ s_x H_x^c & s_y H_y^c & \tilde{Q}_3 H_z^c \end{bmatrix} = j\omega\varepsilon_0\varepsilon_r \begin{bmatrix} \tilde{Q}_3 & 0 & 0 \\ 0 & \tilde{Q}_3 & 0 \\ 0 & 0 & \tilde{Q}_3^{-1} \end{bmatrix} \begin{bmatrix} s_y / s_x & 0 & 0 \\ 0 & s_y / s_x & 0 \\ 0 & 0 & s_x s_y \end{bmatrix} \begin{bmatrix} s_x E_x^c \\ s_y E_y^c \\ \tilde{Q}_3 E_z^c \end{bmatrix} \tag{4.15}$$

in which $\tilde{Q}_3 = 1 + \tilde{x}/R = 1 + x/R - j\sigma(x - \zeta_0)^3 / (3RL_{pml}^{\kappa})$. For verifying purposes, Eq. (4.14) is expanded and compared to Eq. (11a) in Ref. [102] and after lengthy mathematical manipulations, they are demonstrated to be identical with each other. Not only in local CCS, we further apply the transformation theory to cylindrical and spherical coordinate systems and indeed their equivalence is obtained with existing formulations [Kowalczyk] that our results are validated.

In summary, we have successfully obtained full vectorial Maxwell equations in local CCS and also the corresponding PML formulations through rigorous mathematical derivations that preserve the integrity of the equations with no paraxial or any sort approximations assumed. In the following sections, Eq. (4.7)-(4.8) and (4.14)-(4.15) are solved together with appropriate numerical implementations for studying the bend losses of strongly-guiding LMA LCFs.

5.4 Simulation benchmark

There are several numerical techniques available for mode solving in waveguides including multipole method (MPM) [104], finite difference frequency domain method (FDFD) [105], transfer matrix method (TMM) [106, 107] and finite element method (FEM) [108]. Among them, MPM is limited to the inhomogenity induced through bending for it can only handle straight waveguides with simple step-index profiles consisting of circular contours. Finite difference method, on the other hand, can treat more general problems and is probably the most popular one primarily because it is relatively easy to understand and implement. One disadvantage of FDFD, however, lies on its discretization method which may cause accuracy limitations when curved interfaces are encountered [109]. Taking these factors into account, we choose FEM over TMM because although both fit in with simulation requirements in our case, FEM can be utilized immediately with the availability of commercialized software COMSOL Multiphysics.

Finite element method (FEM) has been used in a number of previous work for analysis of straight or bent optical waveguides and holey fibers [101, 110]. However, before rushing to bend loss calculations for LCFs, we start with benchmarking straight

LCFs and determining appropriate PML parameters to use. Figure 5.3 shows the domain deployed for simulation with gray areas indicating PML regions. Only half of the geometry is needed due to the mirror symmetry in the vertical direction. Note we keep the entire domain in the x axis because horizontal mirror symmetry is only valid for straight fibers and is not preserved in the case of bent waveguides due to bending induced inhomogenity across x axis. Λ, d are defined as hole spacing and hole diameter respectively in Figure 5.3 with core diameter calculated to be $2\rho = 2\Lambda - d$. The computation domain has an area of width L_x, height L_y and is truncated by PML regions of thickness L_{pml}^x and L_{pml}^y.

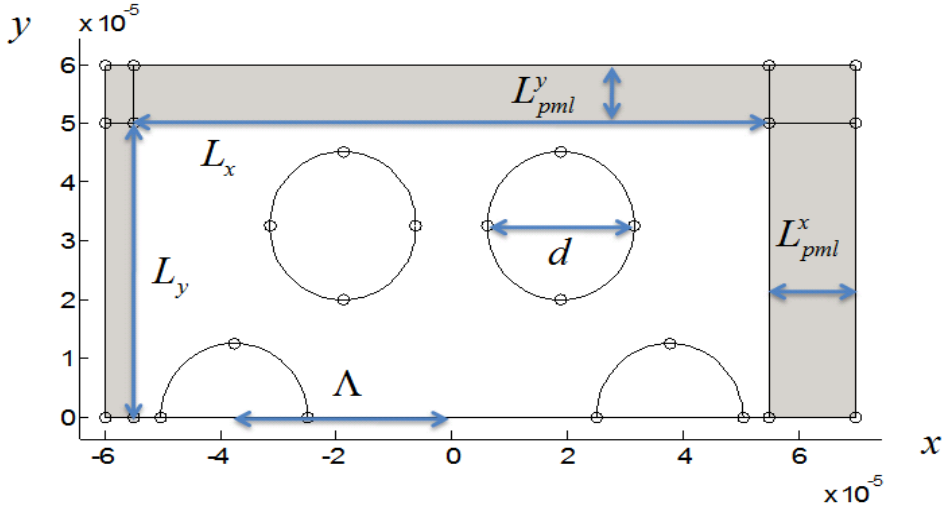

Figure 5.3: The geometry used for simulation. Note only half of the domain is used for the analysis due to the mirror symmetry in vertical axis. Dimensional unit is in meters. Colored areas are PML regions.

For material parameters, since we are interested in designing a LCF for high power ytterbium lasers and amplifiers, a device length of 2-3 m is assumed. Refractive index of air is taken to be 1 and silica glass index 1.444 at the desired operational wavelength of

1.05 μm. We analyzed a structure with d = 12.68 μm and Λ = 37.68 μm. This corresponds to a core diameter 2ρ of 50 μm and d/Λ of 0.673. Given these parameter values, first three groups of modes are calculated by Multipole method to be $1.443926 - i1.167\times10^{-9}$, $1.443815 - i3.076\times10^{-8}$ and $1.443815 - i3.355\times10^{-8}$ and they are considered as exact solutions against FEM simulation results.

The formulation for PML in straight fibers has been studied extensively [Berenger]. Although we did not lay out explicitly these equations, they can be retrieved from Eqs. (4.14) and (4.15) by viewing straight fibers as a special case to bent ones when R is large $\sim \infty$. It is then straightforward to implement the simulation with the Mode analysis module of COMSOL. Inside PML the artificial materials are set to be uniaxial or biaxial depending on its positions with complex dielectric components for absorbing outgoing radiations and avoiding any reflections at the boundaries. Since the real parts of the FEM results converge quickly to the exact numbers, we focus on optimization of the imaginary parts of the complex refractive index. According to Eq. (4.11), the PML thickness L_{pml}^{κ} and absorption coefficient σ are to be determined. Starting with a maximum mesh size of 1 μm, it is tested that L_{pml}^{κ} needs to be at least 15, 10 and 5 μm with corresponding σ of 9.8, 15 and 20 so the relative errors of the imaginary parts are small and stable. We further verified that a mesh size of 1 μm is sufficient for a relative error of less than 1% for the imaginary part of the fundamental mode and 2% for that of the 2nd and 3rd modes. In the end, the sizes of L_x and L_x are also checked that their variations do not make much differences as anticipated.

PML optimization for bent fibers is performed as well. We use a LCF of $d/\Lambda = 0.65$ and $2\rho = 50$ μm. Simulation was done for $\sigma = 20$ and a maximum mesh size of 1 μm at bent radii of R = 1 m and 0.2 m. Since there are no exact solutions in these cases (Multipole method cannot handle bent fibers), we increase L_{pml}^{κ} and monitor the fluctuations of imaginary part of mode refractive index until it is stable within certain range. It is decided that L_{pml}^{κ} needs to be larger than 5 μm and 10 μm for R = 1 m and 0.2 m respectively. In the following analysis, we use $\sigma = 20$, mesh size of 1 μm, wavelength 1.0482 μm and refractive indices for core and air to be 1.444 and 1 respectively. Note the modes of bent fibers radiate away from the center of bend, so different widths of PML are used with left L_{pml}^{x} = 10 μm and right L_{pml}^{x} = 20 μm as illustrated in Figure 5.3. L_{pml}^{y} is also set to be 20 μm.

5.5 Bend loss analysis for leakage channel fiber lasers

Simulated first three modes are shown in Figure 5.4 for a bent LCF of $d/\Lambda = 0.65$ and 2ρ = 50 μm at a bending radius R = 11 cm. The intensity profiles of the fundamental, second and third order mode are given from left to right in Figure 5.4 for bending in (a) AA, i.e. bend plane intersecting two holes, and (b) for BB, i.e. bend plane intersecting center of glass regions between holes, directions. The bending orientations are illustrated in Figure 5.5 for better visualization.

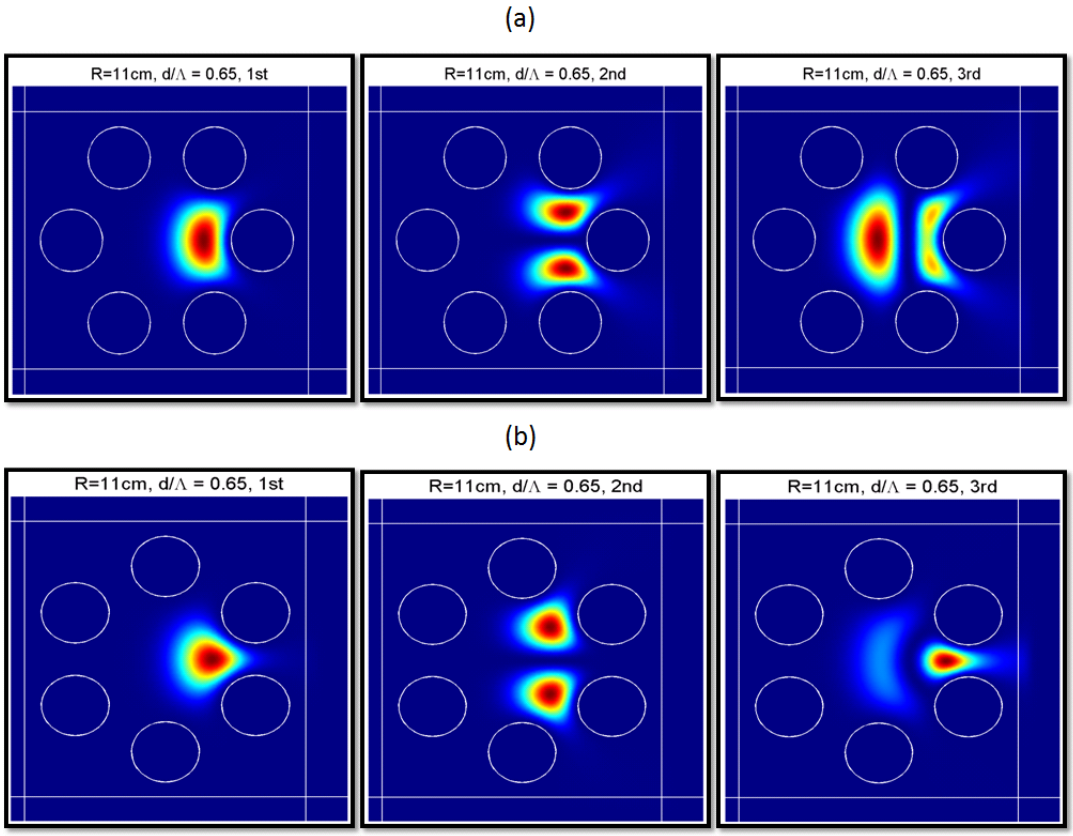

Figure 5.4: Intensity profiles of first three modes within a LCF fiber at a bend radius of 11 cm for (a) AA and (b) BB bending orientations [111].

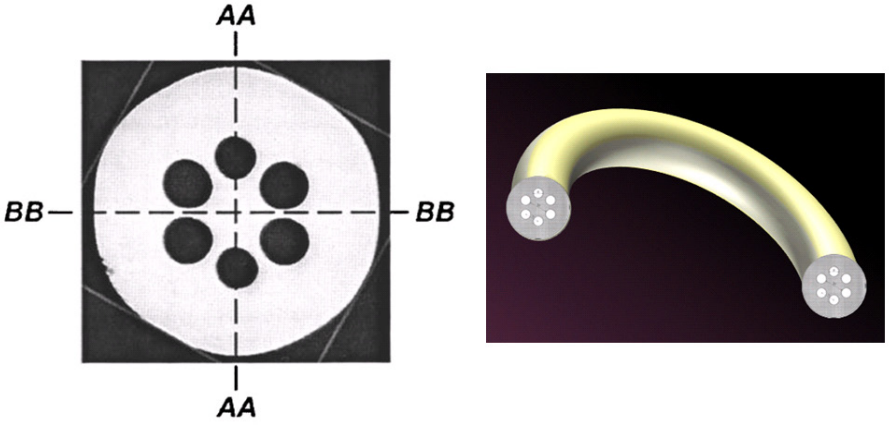

Figure 5.5: A fabricated LCF (left) [112] illustrating two bend planes and such LCF at bends for better visualizations (right)

One common feature is that all mode profiles move away from the center of the bend (located to the left of the plot) as a result of monotonic increments of refractive index in the x axis. The propagation constants, i.e. real parts of the effective refractive indices, also show a general trend of increase towards small bend radius. It is interesting to observe that the third mode has similar bending loss as that of the second mode for AA bend while experiencing higher ones in BB bend (not shown here), which is probably explained by the fact that in the former case the position of the air hole prevents the mode from shifting and thus decrease the amount of leaky losses.

Fundamental and 2_{nd} mode bend loss versus bending radius R are summarized in Figure 5.6 under both AA and BB orientations at various hole diameters d/Λ = 0.65, 0.7, 0.75, 0.8 and 0.85. Apparently, confinement loss for all modes increases with decreasing bend radius and the rate of increase also raises towards small bends. When R is large ~ 1 m, there is very little difference between AA and BB bend for all modes studied. For small bend radius, the fundamental mode is slightly leakier in BB than AA bend while there is a large contrast between two bending orientations for the 2_{nd} mode. To our surprises, the 2_{nd} mode can exhibit even less loss than the fundamental mode under BB bend. Fortunately, this only happens at very small bend radius where fundamental mode is extremely lossy and thus is out of the operation range of our interests. For a practical fiber without deliberate control of bend orientations, it is realistic to expect intermittent sections of AA and BB bends and thus the lower bend loss of the 2_{nd} mode under BB orientation may reduce overall differential mode loss between the 2_{nd} and fundamental mode, which must be considered during the design process. Another point to note is that all bend loss is significantly reduced for larger d/Λ. When operating at very small bend

radius, large d/Λ is preferred. Differential mode loss is, however, largest at large bend radius, a point to be further discussed later.

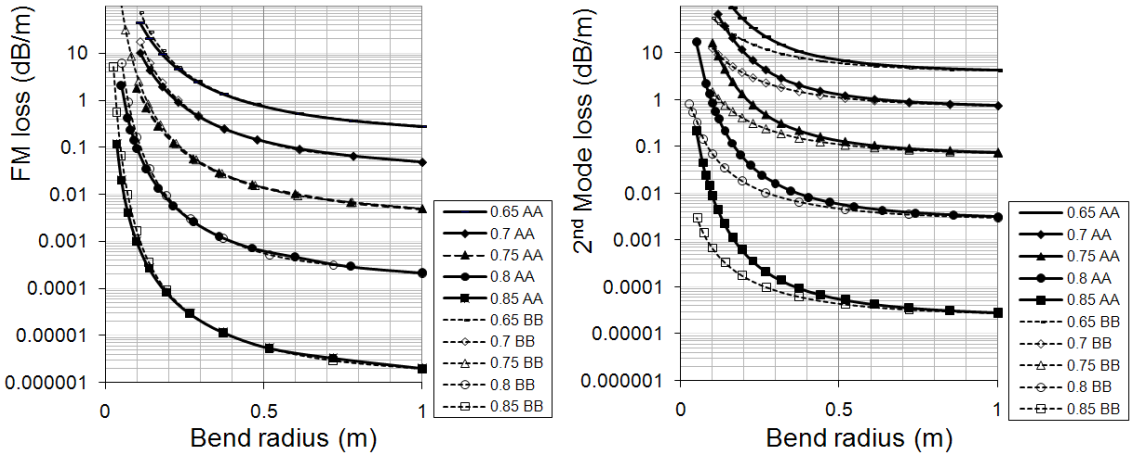

Figure 5.6: Bend loss of fundamental mode and 2nd mode for various d/Λ under AA and BB bend.

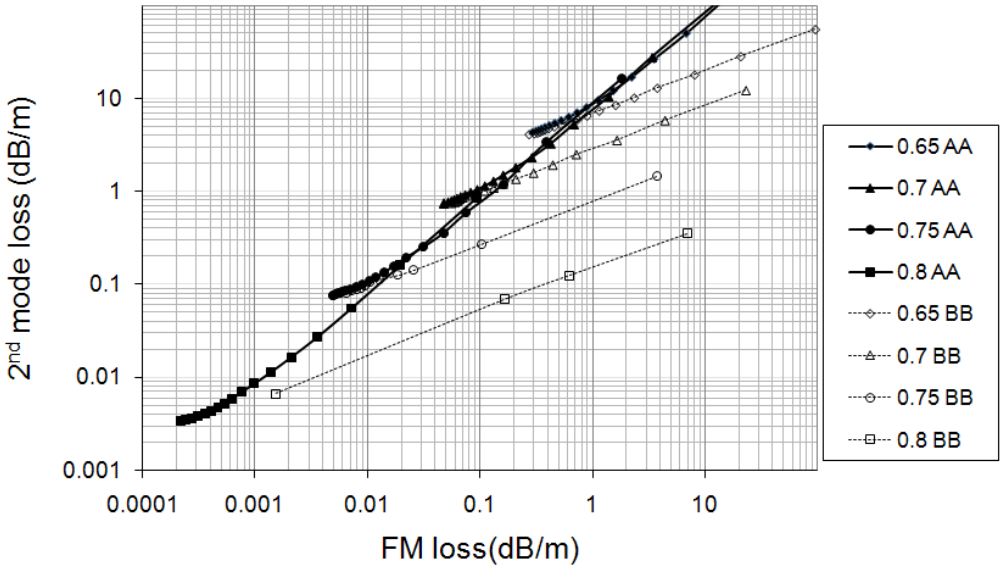

Figure 5.7: 2nd mode loss vs. fundamental mode loss for various d/Λ.

The data in Figure 5.6 is replotted in Figure 5.7 as the 2_{nd} versus the fundamental mode loss for better visualization of differential mode loss. Curves for AA orientation are shown with solid lines and filled symbols, while that of BB bends are plotted as dotted

lines and unfilled markers. For each d/Λ, lower left part of the curve corresponds to large bend radius and top right part to small ones. There are a few points to note. The first is that curves for both orientations essentially overlap for large R (bottom left part of the curves) as we pointed out earlier in the last paragraph, and they deviate towards small bend radius (top right part). The slope of the lines is larger in AA than BB bends indicating again the differential mode loss is smaller in latter case. Secondly, each curve for AA orientation falls onto a trend line represented by $\alpha_{2nd} = 9.1 \times \alpha_{FM}$ at small bend radius, i.e. the bend loss of the second order mode is 9.1 times of that of fundamental mode when both are expressed in decibels. Thirdly, at large bend radius, 2_{nd} mode loss is located above the corresponding points extended from the trend line. This is the preferred regime to operate for all d/Λ since high differential loss, $\alpha_{2nd} \approx 25 \times \alpha_{FM}$, can be obtained at this part of the curves. Based on these variations, d/Λ can be chosen to give acceptable fundamental mode loss depending on the desired device length and core diameters. Finally, each curve for BB orientation is substantially lower than corresponding curves for AA bend at small bend radius (top right part of curves). This shows that 2^{nd} order mode loss for BB orientation is lower than corresponding loss for AA bend with the same fundamental mode loss, a point we made earlier. Each curves for BB orientation is essentially parallel to each other at small bend radius, indicating that they will increase by a same factor when fundamental mode loss increases by a factor of 10.

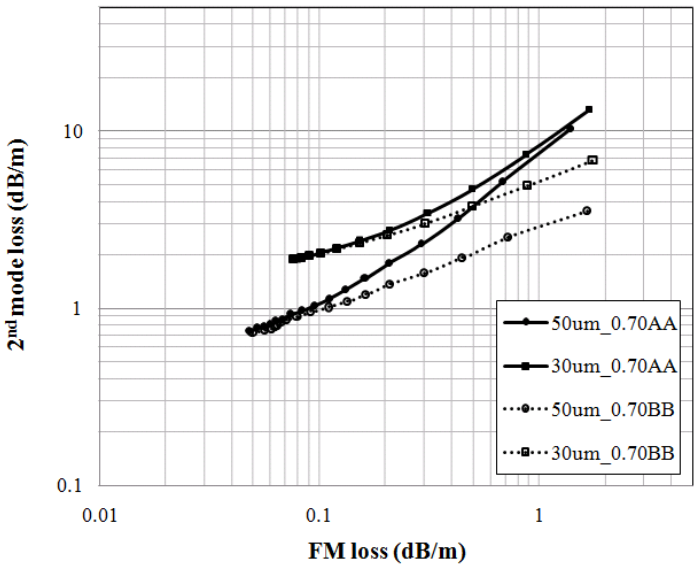

Figure 5.8: 2nd mode loss vs. fundamental mode loss for LCFs with 30μm and 50μm core diameter and d/Λ=0.7.

In a previous study of straight LCFs [2], it has been shown that LCFs can be designed for a wide range of core diameters. Here we also explore bend loss of a LCF with 30μm core diameter and d/Λ = 0.7 to further understand bend loss dependence on core diameter. The data is plotted in Figure 5.8 as 2_{nd} mode versus fundamental mode loss in both orientations for 30μm core as well 50μm LCFs with d/Λ = 0.7. The higher 2_{nd} order mode loss of the 30μm core LCF than that of the 50μm core at large bend radius, i.e. small fundamental mode loss, is clearly seen for both AA and BB bends. For BB orientation, 2_{nd} mode loss of the 30μm LCF is also higher than that of the 50μm for small bend radius, i.e. large fundamental mode loss, while, for AA orientation, the 2nd mode loss of the 30μm core LCF converges with that of the 50μm core LCF at very small bend radius. In any case, the increase of 2_{nd} mode loss for the 30μm LCF is helpful, but not significant, proving that the differential loss has weak core diameter dependence and much larger core diameter is possible with appropriate LCF designs.

5.6 Experiment results and discussion

Comparison between FEM simulations and experimental results is conducted in this section. The bend loss of a fabricated fiber with four large holes and two small holes was measured for both AA and BB directions. To ensure bending orientations, we took the images of the end face of the fiber cross section at the output stage and measure the transmitted power. The cross-sectional photo of the fiber is shown in the inset of Figure 5.9. The geometry information is obtained by boundary extraction from the photo to give a large hole spacing Λ_A 52 μm, a large hole diameter d_A 45.4 μm, a small hole separation Λ_B 52 μm and a small hole diameter d_B 39 μm. In addition, we notice that there is a small angle deviation of 2° between adjacent large holes as shown in Figure 5.9, which may be due to fabrication variations. This fiber with aforementioned parameters is then simulated using FEM. The measured loss for AA and BB orientations are plotted as circles and squares respectively; the simulated data for each orientation are shown as solid and dashed lines. The simulation fits the measured data reasonably well.

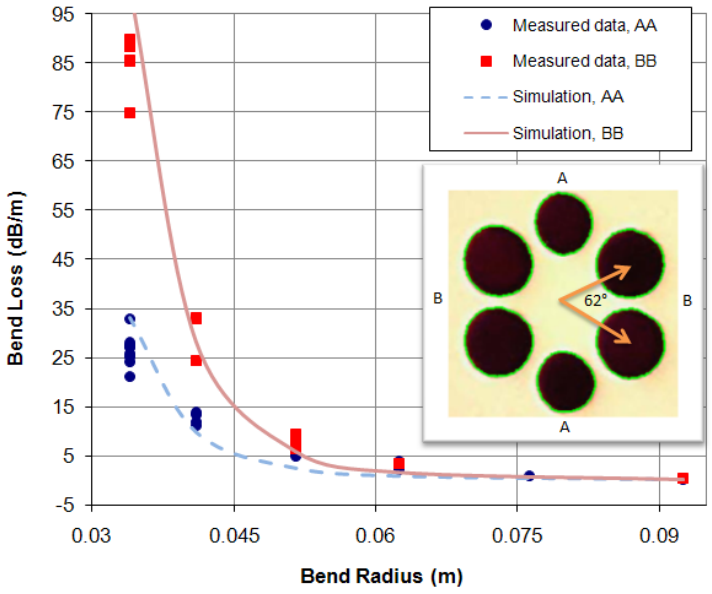

Figure 5.9: Measured and simulated bend loss for AA and BB orientations for a fabricated fiber. See text for details.

5.7 Discussion

For LCFs, increasing relative hole diameter, i.e. larger d/Λ, can effectively reduce fundamental mode loss even at very small bend radius. Considering a LCF of $d/\Lambda = 0.85$, fundamental bend loss can be achieved as low as 0.1 dB/m for a bend radius of 4cm. At the same time, 2_{nd} order mode can be estimated by the trend line given by $\alpha_{2nd} = 9.1 \times \alpha_{FM}$. As shown in Figure 5.7, relatively higher 2_{nd} order mode loss is obtained at larger bend radius, $\alpha_{2nd} \approx 25 \times \alpha_{FM}$ at straight operations. In many practical situations, higher differential mode loss is preferred. It is consequently better to work at large bend radius. Additional differential mode loss increase can be achieved by optimization of rare-earth doping profile so that it overlaps spatially better with the fundamental mode than the 2_{nd} order mode [113]. Further improvement can be gained by resonantly coupling out the 2_{nd} order mode as demonstrated in a theoretical study in [110] at the expense of narrow wavelength range of operation and much stringent fabrication tolerances. There is an additional reason for working at larger bend radius. This is due to that mode distortion at small bend radius leads to a reduction of effective area of the optical fiber [91]. In our simulation of effective mode area of LCFs with a core diameter of $2\rho = 50$ μm and $d/\Lambda =$ 0.7, 0.75, 0.8 and 0.85, the reduction of effective area of the 50 μm core diameter LCFs at small bend radius is dramatic. This effective area reduction has a weak dependence on d/Λ. To be able to maintain 90% of the maximum effective area for the LCFs with 50 μm core diameter, bend radius needs to be kept above ~0.4 m. At $R = 0.2$ m, effective area is reduced to ~75% of the maximum.

Bend loss of the 2_{nd} order mode, i.e. HE01+HE21, is studied in details in Figure 5.6 and Figure 5.7. We have also studied bend loss of the 3_{rd} mode, i.e. HE01-HE21, and found it to be higher than that of the 2_{nd} mode with very similar dependence on bends. It is not presented here. In this study of bending effect, we have focused on 50μm core LCFs with various d/Λ. In a previous study of straight LCFs, we have found that core diameters exceeding 100μm are possible with appropriate designs of LCFs. In addition, LCFs have weak wavelength dependence, i.e. capable of broad band operation. This weak wavelength dependence also translates into ease of fabrication due to the relaxed tolerance.

5.8 Conclusion

In conclusion, we have systematically studied bend performance of LCFs for both fundamental and higher order modes. It is found that low bend loss of all modes can be obtained with large d/Λ and greatest differential mode loss is achieved at large bend radius. In general, LCFs perform differently for distinct bending planes and depending on the degree of coiling, the bend loss of 2_{nd} mode can vary from 25 to 9.1 times of that of fundamental mode in AA orientation, which is preferred over BB bend for its superior mode filtering effects. In conventional step-index LMA fibers, small coils are required to provide significant differential mode loss for single mode operation [29]. This can reduce the effective area of coiled fiber to the point where no overall gain in effective area is achieved. On the other hand, LCF can be designed to provide maximum differential mode loss in straight fibers and large differential mode loss at large coil diameters. This would provide a real practice solution for large effective area fibers.

CHAPTER VI

Conclusions and Contributions

6

A theoretical investigation of three fiber laser structures was conducted in this dissertation toward developing diffraction-limited high power fiber laser sources. In CHAPTER II, model for coherent combining in passive fiber laser arrays, we proposed a novel and effective model for studying the beam combining mechanism, spectral/temporal dynamics, the role of nonlinearity and the power scaling issues of such composite cavities. The multiple longitudinal modes of fiber lasers were incorporated into the array simulation for the first time and highly efficient coherent combining was obtained without the need to deliberately control the fiber lengths (mismatch). The model closely resembles the real experimental conditions and is completed by including various effects such as propagation, group velocity dispersion, Kerr nonlinearity, loss dispersion, unbalanced mirror reflectivities, gain saturation and dynamics. Based on the model, the combining mechanism is elucidated and verified to be relying on the presence of multilongitudinal modes of the fiber lasers. We clarify the role of nonlinearity to be detrimental for array combining while the gain dynamics and the interaction of counterpropagating waves are found to have little impact on the combining performance. When there is more than one loss mechanism present, we showed that the array chooses to lase at the frequency with the minimum overall losses. The model can also be extended to four or more channel fiber laser arrays and the periodicity of the output power

spectrum is found to be determined by the greatest common divisor of the consisting fiber lengths. Finally, we provided a simple explanation for the drastic decrease in the combining efficiency of large arrays by the non-existence of exact solutions in an over-determined system where only optimal frequencies can be obtained in most cases. The deviation from the exact solution induces phase mismatch and is responsible for the power loss into the lossy port.

The studies for rare-earth doped fiber laser arrays are continued in CHAPTER III. We utilized the newly developed model to fit the experimental data and explored the evolution of the power scalability up to 16-channel arrays. In addition to the combining efficiencies, the observed power fluctuations were also modeled with the small length variations on the wavelength scale and they were found to be important factors giving rise to output instability especially for large arrays. The degree of the fluctuation increases monotonically and scales with the array size as N^3. We obtained good agreement between simulation and experimental results for the combining efficiency, the power fluctuations, and also the beat spectra. The application of the optical phase conjugation for coherent combining in passive fiber laser arrays was further studied and its phase reversal property was shown numerically to restore the combining efficiency to 100% regardless of the array sizes.

Due to the limited tunaiblity of the electronic transitions in active ions, we proposed Raman fiber laser arrays in CHAPTER IV as high power coherent sources with diffraction-limited beam quality, especially for wavelengths inaccessible by rare-earth doped fiber lasers. Under idealized conditions of single mode analysis, the intrinsic nonlinearity was found to result in the in- or anti-phase locked states of the Stokes

outputs depending on the pump power level. The coherent combining property of the Raman laser array was also investigated and the simulation showed that the Kerr nonlinearity merely reduces the combining efficiency, which is consistent with the results obtained for rare-earth doped fiber laser arrays.

In the last chapter, we took a different approach in realizing high power fiber lasers by analyzing the bend performance of large-mode-area leakage channel fibers. Through proper coordinate transformation of Maxwell equation and the setup of perfect matched layers, we accurately calculated the propagation loss of the fundamental and higher order modes for various bending radii in an attempt to enhance the mode filtering effects. The simulation results, however, suggest that greatest differential modal loss is achieved at large bend radius and the modal separation decreases with bending.

The results presented in this dissertation should prove useful in the quest for high power diffraction-limited fiber laser sources.

APPENDIX

Numerical Methods

7

In this appendix, I list the Fortran 90 codes for the numerical implementation of split-step Fourier method (SSFM) under parallel computing using Message Passing Interface (MPI) library. Considering an *N*-channel fiber laser array, the wave propagation governed by nonlinear Schrödinger equation in each of the laser element is designed to be integrated by a CPU node and so a total of *N* nodes need to be requested in the beginning of execution. For the formulations of SSFM and its solving principles, excellent material is covered in the Sec. 2.4.1 in Ref. [3]. The basic idea is that the complex electric field variable is transformed back and forth between the spectral and temporal domains for the ease of integration of linear (dispersion, gain or absorption) and nonlinear terms (SPM and XPM) respectively. Since the Fourier transformation is involved heavily, the adoption of fast Fourier transformation (FFT) algorithm enables faster numerical evaluation and thus shorter computation durations. As mentioned in Sec. 3.2.1, I chose the standard FFT library FFTW [FFTW], but other valid FFT codes can be used as well. The programming code below is particularly for solving a two-channel fiber laser array in the unidirectional configuration as discussed in Sec. 2.4 and it can be easily extended to larger arrays by simply changing *M* variable (the number of nodes requested in addition to the master node) and the formulation of coupling region.

```
program BeamC2
use mpi

!!!!!!!!!!!!!!!!!!!!!!!!!!!!!!!!!!!!!!!!!!!!!!!!!!!!!!!!!!!!!!!!!!!!!!!!!!!!
! compile with Fortran 90 mpi                                                  !
!                                                                             !
! % mpif90 -o exefile file.f90 -L$FFTW_LINK -lfftw3 -lacml                    !
! % miprun -np #processors exefile                                            !
!                                                                             !
!!!!!!!!!!!!!!!!!!!!!!!!!!!!!!!!!!!!!!!!!!!!!!!!!!!!!!!!!!!!!!!!!!!!!!!!!!!!


     implicit none

     ! MPI Constants
     integer numprocs, ierr, master, myid, tag, comm
     real*8 Cpu_start, Cpu_end, Cpu_total
     real*8 Wall_start, Wall_end, Wall_total

     ! FFTW constants
     integer*8 planf, planb
     integer*8 FFTW_FORWARD, FFTW_BACKWARD
     integer*8 FFTW_ESTIMATE, FFTW_MEASURE

     ! Common Constants
     integer*4 M
     integer*4 npts, dnpts
     integer*4 rtstps, RT
     integer*4 mod_rt
     real*8 c0, wvlngth
     real*8 Psat
     real*8 alpha
     real*8 spordr
     real*8 beta2, bcff
     real*8 n1
     real*8 kpl
     real*8 dlmin, dlmax, dlordr
     complex*16 i, iGammaN

     ! Specify the number of nodes needed in addition to the master
     ! node
     data M/1/

     ! Variables
     integer*4 flid(0:M,4)
     integer*4 nstps
     integer*4 k, kk, jrt, jstp
     real*8 pi
     real*8 L(0:M)
     real*8 refl(0:M)
     real*8 h, Twindow
     real*8 effP
     real*8 findmax
     real*8 findmin
     real*8 simpson, p_i, t_window
     complex*16 g0(0:M)
     complex*16 los, g, Gav, d_los
```

```
character*80 fmt, ganfmt
character*20 flestr(3)
common /simpson_cff/ p_i, t_window

! Set FFTW constants
data FFTW_FORWARD/-1/, FFTW_BACKWARD/1/
data FFTW_ESTIMATE/0/, FFTW_MEASURE/1/

! Set Common Constants
data master/0/
data npts/131072/        ! NOTE: npts has to be to the order of 2
data dnpts/1/
data rtstps/6/, RT/2000/
data mod_rt/200/
data c0/3.0D8/
data wvlngth/1.545D-6/
data Psat/0.6D-3/
data alpha/5.8D-2/
data spordr/1.0D-14/
data beta2/-0.003D-24/, bcff/0.0/
data n1/1.5D0/
data kpl/0.5D0/
data i/(0.0,1.0D0)/
data iGammaN/(0.0,0.003D0)/

! Common Vectors
real*8 omega(1:npts), omega2(1:npts), time(1:npts)
real*8 linphse(1:npts), gvdphse(1:npts), ttlphse(1:npts)
real*8 angl(1:npts)
complex*16 Ef(1:npts), Et(1:npts)
complex*16 losDp(1:npts)
complex*16 Ef_0(1:npts)

! Vectors used by master
real*8 EffP_buff(0:M)
real*8 ave(0:M), std(0:M), pwer(0:M,1:500)
real*8 angl_buff(1:(M+1)*npts)
complex*16 Gav_buff(0:M)
complex*16 Ef_buff(1:(M+1)*npts)
complex*16 Ef_out(1:(M+1)*npts)

! Set Variables
pi = dacos(-1.0)
L = (/24.001D0, 24.0D0/)
refl = (/0.2D0, 0.0/)
g0 = cmplx(2.67D0,0)
p_i = pi
write(fmt,*) '(',npts,'E15.7)'
write(ganfmt,*) '(3E15.7)'

! Initialize MPI
comm = MPI_COMM_WORLD
call MPI_Init(ierr)
call MPI_Comm_rank(comm, myid, ierr)
call MPI_Comm_size(comm, numprocs, ierr)

! Initialize FFTW
```

```
call  dfftw_plan_dft_1d(planf,npts,Et,Ef,FFTW_FORWARD,FFTW_ESTIMATE)
call  dfftw_plan_dft_1d(planb,npts,Ef,Et,FFTW_BACKWARD,FFTW_ESTIMATE)

! Set ranks-dependent variables
if (myid.EQ.master) then
   Twindow = findmax(L,M)*n1/c0*1
end if
h = L(myid)/rtstps
los  = cmplx(-alpha/2*h/2.0,0.0)

call MPI_Bcast( Twindow, &
                      1, &
              MPI_REAL8, &
                 master, &
                   comm, &
                   ierr)

t_window = Twindow

! Setup output file
if (myid.EQ.master) then
  do k = 0,M
     flid(k,:) = (/(kk*10, kk=1,4)/) + k*100
     write (flestr(1),'(A,I1,A)') 'time',k,'.txt'
     write (flestr(2),'(A,I1,A)') 'freq',k,'.txt'
     write (flestr(3),'(A,I1,A)') 'gain',k,'.txt'
     write (flestr(4),'(A,I1,A)') 'angl',k,'.txt'
     open (flid(k,1), FILE=flestr(1), STATUS='NEW')
     open (flid(k,2), FILE=flestr(2), STATUS='NEW')
     open (flid(k,3), FILE=flestr(3), STATUS='NEW')
     open (flid(k,4), FILE=flestr(4), STATUS='NEW')
   end do
   open (330, FILE="time.txt", STATUS='NEW')
   open (340, FILE="freq.txt", STATUS='NEW')
end if

! Measure Time & Initialize random number generator
Wall_start=MPI_Wtime()
call cpu_time(Cpu_start)

! Setup of propagation vectors (rank-dependent)
time = (/(k-1-npts/2, k=1,npts)/)*Twindow/(npts-1)
omega = (/(k-1,k=1,npts/2), &
        (k-npts-1,k=npts/2+1,npts)/)*2*pi/Twindow
omega2 = omega*omega
linphse = omega*n1*h/2.0/c0
gvdphse = omega2*beta2/2.0*h/2.0
ttlphse = modulo(linphse + gvdphse + &
          n1*2*pi/wvlngth*h/2.0, 2*pi)
losDp = cmplx(-omega2*bcff/2.0*h/2.0,0.0) + los

! Prepare for loop & output time and freq
call signedRNG(Ef_0, npts, spordr, myid)
Ef = Ef_0
g = g0(myid)
Gav = cmplx(0,0)
```

```
! Collected by master
call MPI_Gather( Ef, npts, MPI_DOUBLE_COMPLEX, &
            Ef_buff, npts, MPI_DOUBLE_COMPLEX, &
                           master, comm, ierr)

if (myid.EQ.master) then
   g = (0.0,0.0)
   write(330,fmt) (time(kk)*1e9, kk=1,npts,dnpts)
   write(340,fmt) (omega(kk)/2/pi/1e9,kk=1,npts,dnpts)
   do k=0,M
     Ef = Ef_buff(k*npts+1:(k+1)*npts)
     call dfftw_execute_dft(planb, Ef, Et)
     Et = Et/npts
     effP = simpson(Et,npts,1)
     angl = modulo(ATAN2(imag(Ef),real(Ef)),2*pi)

     write(flid(k,1),fmt) (cdabs(Et(kk))**2,kk=1,npts,dnpts)
     write(flid(k,2),fmt) (cdabs(Ef(kk))**2,kk=1,npts,dnpts)
     write(flid(k,3),ganfmt) L(k), refl(k), real(2*g/h)
     write(flid(k,4),fmt) (angl(kk),kk=1,npts,dnpts)
   end do
end if

! Main Loop !
do 66 jrt=1,RT

   ! Random number as ASE
   call signedRNG(Ef_0, npts, spordr, myid)
   Ef = Ef + Ef_0

   do jstp = 1,rtstps

      ! Calculate effective power
      call dfftw_execute_dft(planb, Ef, Et)
      Et = Et/npts
      effP = simpson(Et,npts,1)
      g = g0(myid)/2/(1+effP/Psat/Twindow)*h

      ! freq domain
      Ef = Ef*cdexp(g/2 + losDp + cmplx(0,ttlphse))

      ! time domain
      call dfftw_execute_dft(planb, Ef, Et)
      Et = Et/npts
      Et = Et*cdexp(iGammaN*cdabs(Et)**2*h)

      ! freq domain
      call dfftw_execute_dft(planf, Et, Ef)
      Ef = Ef*cdexp(g/2 + losDp + cmplx(0,ttlphse))

      ! average gain and pwer
      Gav = Gav + g
   end do

   !
   Gav = Gav*2/rtstps/h
   call dfftw_execute_dft(planb, Ef, Et)
```

```
Et = Et/npts
effP = simpson(Et,npts,1)
angl = modulo(ATAN2(imag(Ef),real(Ef)),2*pi)

! Collected by master
call MPI_Gather( Gav, 1, MPI_DOUBLE_COMPLEX, &
            Gav_buff, 1, MPI_DOUBLE_COMPLEX, &
                        master, comm, ierr)

call MPI_Gather( Ef, npts, MPI_DOUBLE_COMPLEX, &
            Ef_buff, npts, MPI_DOUBLE_COMPLEX, &
                         master, comm, ierr)

call MPI_Gather( EffP, 1, MPI_REAL8, &
            EffP_buff, 1, MPI_REAL8, &
                 master, comm, ierr)

call MPI_Gather( angl, npts, MPI_REAL8, &
            angl_buff, npts, MPI_REAL8, &
                    master, comm, ierr)

! Through 50:50 coupler
if (myid.EQ.master) then

    ! coupler
    Ef_out(1:npts) = &
          sqrt(kpl)*Ef_buff(1:npts) &
          -i*sqrt(1-kpl)*Ef_buff(npts+1:2*npts)
    Ef_out(npts+1:2*npts) = &
          -i*sqrt(1-kpl)*Ef_buff(1:npts)+ &
          sqrt(kpl)*Ef_buff(npts+1:2*npts)

    ! store feedback in Ef_buff
    SELECT CASE(refl(0).GT.refl(1))
           CASE(.True.)
              Ef_buff = refl(0)/sqrt(2.0)* &
                        (/Ef_out(1:npts), Ef_out(1:npts)/)

           CASE(.False.)
              Ef_buff = refl(1)/sqrt(2.0)* &
               (/Ef_out(npts+1:2*npts), Ef_out(npts+1:2*npts)/)

    END SELECT

    ! Output by master
    if (modulo(jrt,mod_rt).EQ.0) then
       do k = 0,M
          Gav = Gav_buff(k)
          Ef = Ef_out(k*npts+1:(k+1)*npts)*dsqrt(1-refl(k)**2)
          call dfftw_execute_dft(planb, Ef, Et)
          Et = Et/npts
          effP = simpson(Et,npts,1)
          angl = angl_buff(k*npts+1:(k+1)*npts)

          write(flid(k,1),fmt)(cdabs(Et(kk))**2,kk=1,npts,dnpts)
          write(flid(k,2),fmt)(cdabs(Ef(kk))**2,kk=1,npts,dnpts)
          write(flid(k,3),ganfmt) effP_buff(k)/Twindow, &
```

```
                                        effP/Twindow, real(Gav)
                  write(flid(k,4),fmt) (angl(kk),kk=1,npts,dnpts)

                  write(*,*) jrt, k, effP_buff(k)/Twindow, &
                             effP/Twindow, real(Gav)

               end do
            end if
         end if

         ! Feedback reflected wave
         Gav = cmplx(0,0)
         call MPI_Scatter( Ef_buff, npts, MPI_DOUBLE_COMPLEX, &
                           Ef, npts, MPI_DOUBLE_COMPLEX, &
                                     master, comm, ierr)

      ! End of Main Loop
      66   enddo

      ! Calculate elasped time
      Wall_end=MPI_Wtime()
      call cpu_time(Cpu_end)
      Wall_total = Wall_end - Wall_start

      call MPI_Reduce( Cpu_end-Cpu_Start, &
                       Cpu_total, &
                              1, &
                       MPI_REAL8, &
                         MPI_SUM, &
                          master, &
                            comm, &
                            ierr)

      ! Record CPU time and Wall time
      ! Ideally CPU time is (M+1) times of Wall time
      if (myid.EQ.master) then
         write(*,*) "Cpu time = ", Cpu_total, "sec."
         write(*,*) "Wall time = ", Wall_total, "sec."
      end if

      ! finalize FFTW
      call dfftw_destroy_plan(planf)
      call dfftw_destroy_plan(planb)

      ! finalize MPI
      call MPI_FINALIZE(ierr)

end program BeamC2
```

BIBLIOGRAPHY

1. T. Y. Fan, "Laser beam combining for high-power, high-radiance sources," Ieee Journal of Selected Topics in Quantum Electronics **11**, 567-577 (2005).

2. A. TÜNNERMANN, "High-power cw Fiber Lasers," LASER SOURCES (2005).

3. G. P. AGRAWAL, *Nonlinear Fiber Optics* (Academic Press, San Diego, 2001).

4. S. J. Augst, T. Y. Fan, and A. Sanchez, "Coherent beam combining and phase noise measurements of ytterbium fiber amplifiers," Optics Letters **29**, 474-476 (2004).

5. S. J. Augst, J. K. Ranka, T. Y. Fan, and A. Sanchez, "Beam combining of ytterbium fiber amplifiers (Invited)," Journal of the Optical Society of America B-Optical Physics **24**, 1707-1715 (2007).

6. C. Bellanger, A. Brignon, J. Colineau, and J. P. Huignard, "Coherent fiber combining by digital holography," Optics Letters **33**, 2937-2939 (2008).

7. T. M. Shay, V. Benham, J. T. Baker, A. D. Sanchez, D. Pilkington, and C. A. Lu, "Self-synchronous and self-referenced coherent beam combination for large optical arrays," Ieee Journal of Selected Topics in Quantum Electronics **13**, 480-486 (2007).

8. T. M. Shay, V. Benham, J. T. Baker, B. Ward, A. D. Sanchez, M. A. Culpepper, D. Pilkington, J. Spring, D. J. Nelson, and C. A. Lu, "First experimental demonstration of self-synchronous phase locking of an optical array," Optics Express **14**, 12015-12021 (2006).

9. K. H. No, R. W. Herrick, C. Leung, R. Reinhart, and J. L. Levy, "ONE-DIMENSIONAL SCALING OF 100 RIDGE-WAVE-GUIDE AMPLIFIERS," Ieee Photonics Technology Letters **6**, 1062-1066 (1994).

10. E. J. Bochove, P. K. Cheo, and G. G. King, "Self-organization in a multicore fiber laser array," Optics Letters **28**, 1200-1202 (2003).

11. P. K. Cheo, A. Liu, and G. G. King, "A high-brightness laser beam from a phase-locked multicore Yb-doped fiber laser array," IEEE Photon. Technol. Lett. **13**, 439-441 (2001).

12. P. Glas, M. Naumann, A. Schirrmacher, and T. Pertsch, "The multicore fiber - a novel design for a diode pumped fiber laser," Optics Communications **151**, 187-195 (1998).

13. V. P. Kandidov, and I. V. Terekhova, "Phase filtering of the inphase mode of a linear laser array in the Talbot resonator," Quantum Electronics **33**, 531-536 (2003).

14. Y. Kono, M. Takeoka, K. Uto, A. Uchida, and F. Kannari, "A coherent all-solid-state laser array using the Talbot effect in a three-mirror cavity," Ieee Journal of Quantum Electronics **36**, 607-614 (2000).

15. Q. Li, P. F. Zhao, and W. R. Guo, "Amplitude compensation of a diode laser array phase locked with a Talbot cavity," Applied Physics Letters **89** (2006).

16. Q. Li, P. F. Zhao, W. R. Guo, and B. Liu, "The in-phase mode selection of a high-power diode laser array by a talbot cavity with an amplitude compensator," Optics Communications **270**, 323-326 (2007).

17. A. P. Napartovich, and D. V. Vysotsky, "Phase-locking of multicore fibre laser due to Talbot self-reproduction," Journal of Modern Optics **50**, 2715-2725 (2003).

18. T. J. Tayag, M. B. Steer, J. F. Harvey, A. B. Yakovlev, and J. Davis, "Spatial power splitting and combining based on the Talbot effect," Ieee Microwave and Wireless Components Letters **12**, 9-11 (2002).

19. M. Wrage, P. Glas, M. Leitner, D. V. Vysotsky, and A. P. Napartovich, "Phase-locking and self-imaging properties of a Talbot resonator applied to circular structures," Optics Communications **191**, 149-159 (2001).

20. C. J. Corcoran, and F. Durville, "Experimental demonstration of a phase-locked laser array using a self-Fourier cavity," Applied Physics Letters **86** (2005).

21. J. L. Rogers, S. Peles, and K. Wiesenfeld, "Model for high-gain fiber laser arrays," IEEE J. Quantum Electron. **41**, 767-773 (2005).

22. H. Bruesselbach, D. C. Jones, M. S. Mangir, M. Minden, and J. L. Rogers, "Self-organized coherence in fiber laser arrays," Optics Letters **30**, 1339-1341 (2005).

23. H. Bruesselbach, M. Minden, J. L. Rogers, D. C. Jones, M. S. Mangir, and Ieee, *200 W self-organized coherent fiber arrays* (2005).

24. Corning, "Corning SMF-28e+ Optical Fiber."

25. P. Yeh, *Introduction to Photorefractive Nonlinear Optics* (John Wiley & Sons, Inc., 1993).

26. S. Hofer, A. Liem, J. Limpert, H. Zellmer, A. Tunnermann, S. Unger, S. Jetschke, H. R. Muller, and I. Freitag, "Single-frequency master-oscillator fiber power amplifier system emitting 20 W of power," Optics Letters **26**, 1326-1328 (2001).

27. M. C. T. B.E.A. Saleh, *Fundamentals of Photonics* (John Wiley & Sons, Inc., 1991).

28. D. Taverner, D. J. Richardson, L. Dong, J. E. Caplen, K. Williams, and R. V. Penty, "158-mu J pulses from a single-transverse-mode, large-mode-area erbium-doped fiber amplifier," Optics Letters **22**, 378-380 (1997).

29. J. P. Koplow, D. A. V. Kliner, and L. Goldberg, "Single-mode operation of a coiled multimode fiber amplifier," Optics Letters **25**, 442-444 (2000).

30. J. Limpert, A. Liem, H. Zellmer, and A. Tunnermann, "500W continuous-wave fibre laser with excellent beam quality," Electronics Letters **39**, 645-647 (2003).

31. D. Sabourdy, V. Kermene, A. Desfarges-Berthelemot, L. Lefort, A. Barthelemy, P. Even, and D. Pureur, "Efficient coherent combining of widely tunable fiber lasers," Optics Express **11**, 87-97 (2003).

32. D. Sabourdy, V. Kermene, A. Desfarges-Berthelemot, M. Vampouille, and A. Barthelemy, "Coherent combining of two Nd : YAG lasers in a Vernier-Michelson-type cavity," Appl. Phys. B **75**, 503-507 (2002).

33. A. Shirakawa, K. Matsuo, and K. Ueda, "Fiber laser coherent array for power scaling, bandwidth narrowing, and coherent beam direction control," in *Conference on Fiber Lasers II*, L. N. Durvasula, A. J. W. Brown, and J. Nilsson, eds. (San Jose, CA, 2005), pp. 165-174.

34. A. Shirakawa, T. Saitou, T. Sekiguchi, and K. Ueda, "Coherent addition of fiber lasers by use of a fiber coupler," Opt. Express **10**, 1167-1172 (2002).

35. T. B. Simpson, A. Gavrielides, and P. Peterson, "Extraction characteristics of a dual fiber compound cavity," Opt. Express **10**, 1060-1073 (2002).

36. J. Q. Cao, J. Hou, Q. S. Lu, and X. J. Xu, "Numerical research on self-organized coherent fiber laser arrays with circulating field theory," J. Opt. Soc. Am. B **25**, 1187-1192 (2008).

37. D. Kouznetsov, J. F. Bisson, A. Shirakawa, and K. Ueda, "Limits of coherent addition of lasers: Simple estimate," Opt. Review **12**, 445-447 (2005).

38. W. Ray, J. L. Rogers, and K. Wiesenfeld, "Coherence between two coupled lasers from a dynamics perspective," Opt. Express **17**, 9357-9368 (2009).

39. J. E. Rothenberg, "Passive coherent phasing of fiber laser arrays," in *Fiber Lasers V: Technology, Systems, and Applications*, J. Broeng, and C. Headley, eds. (2008), pp. U188-U196.

40. A. E. Siegman, "Resonant modes of linearly coupled multiple fiber laser structures," unpublished (2004).

41. C. J. Corcoran, F. Durville, and K. A. Pasch, "Coherent array of nonlinear regenerative fiber amplifiers," Ieee Journal of Quantum Electronics **44**, 275-282 (2008).

42. T.-w. W. Wei-zung Chang, Herbert G. Winful and Almantas Galvanauskas "Array size scalability of passively coherently phased fiber laser arrays."

43. A. Shirakawa, T. Sekiguchi, K. Matsuo, and K. Ueda, "Scalable coherent beam combining of fiber lasers," OSA TOPS in advanced solid-state photonics **83** (2003).

44. S. Peles, J. L. Rogers, and K. Wiesenfeld, "Robust synchronization in fiber laser arrays," Physical Review E **73** (2006).

45. W. Ray, K. Wiesenfeld, and J. L. Rogers, "Refined fiber laser model," Physical Review E **78** (2008).

46. K. Wiesenfeld, S. Peles, and J. L. Rogers, "Effect of Gain-Dependent Phase Shift on Fiber Laser Synchronization," Ieee Journal of Selected Topics in Quantum Electronics **15**, 312-319 (2009).

47. V. Roy, M. Piche, F. Babin, and G. W. Schinn, "Nonlinear wave mixing in a multilongitudinal-mode erbium-doped fiber laser," Opt. Express **13**, 6791-6797 (2005).

48. S. P. Chen, Y. G. Li, K. C. Lu, and S. H. Zhou, "Efficient coherent combining of tunable erbium-doped fibre ring lasers," Journal of Optics a-Pure and Applied Optics **9**, 642-648 (2007).

49. T. B. Simpson, F. Doft, P. R. Peterson, and A. Gavrielides, "Coherent combining of spectrally broadened fiber lasers," Optics Express **15**, 11731-11740 (2007).

50. E. Desurvire, "Analysis of erbium-doped fiber amplifiers pumped in the I-4(15/2)-I-4(13/2) band," IEEE Photon. Technol. Lett. **1**, 293-296 (1989).

51. E. Desurvire, C. R. Giles, and J. R. Simpson, "Gain saturation effects in high-speed, multichannel erbium-doped fiber amplifiers at λ=1.53 μm," J. of Lightwave Technol. **7**, 2095-2104 (1989).

52. C. R. Giles, E. Desurvire, and J. R. Simpson, "Transient gain and cross talk in erbium-doped fiber amplifiers," Opt. Letters **14**, 880-882 (1989).

53. Didomeni.M, "A single-frequency TEM00-mode gas laser with high output power," Appl. Phys. Lett. **8**, 20-22 (1966).

54. E. J. Bochove, "Effect of Nonlinear Phase on the Passive Phase Locking of an Array of Fiber Lasers of Random Lengths," in *Integrated Photonics and Nanophotonics Research and Applications (IPNRA)*(Honolulu, Hawaii, 2009).

55. C. J. Corcoran, and K. A. Pasch, "Output phase characteristics of a nonlinear regenerative fiber amplifier," Ieee Journal of Quantum Electronics **43**, 437-439 (2007).

56. B. S. Wang, E. Mies, M. Minden, and A. Sanchez, "All-fiber 50 W coherently combined passive laser array," Optics Letters **34**, 863-865 (2009).

57. J. E. Rothenberg, "Passive coherent phasing of fiber laser arrays," in *Conference on Fiber Lasers V*, J. Broeng, and C. Headley, eds. (San Jose, CA, 2008), pp. U188-U196.

58. S. M. Jensen, "THE NON-LINEAR COHERENT COUPLER," Ieee Journal of Quantum Electronics **18**, 1580-1583 (1982).

59. S. R. Friberg, Y. Silberberg, M. K. Oliver, M. J. Andrejco, M. A. Saifi, and P. W. Smith, "ULTRAFAST ALL-OPTICAL SWITCHING IN A DUAL-CORE FIBER NONLINEAR COUPLER," Applied Physics Letters **51**, 1135-1137 (1987).

60. S. R. Friberg, A. M. Weiner, Y. Silberberg, B. G. Sfez, and P. S. Smith, "FEMTOSECOND SWITCHING IN A DUAL-CORE-FIBER NONLINEAR COUPLER," Optics Letters **13**, 904-906 (1988).

61. T. W. Wu, W. Z. Chang, A. Galvanauskas, and H. G. Winful, "Model for passive coherent beam combining in fiber laser arrays," Optics Express **17**, 19509-19518 (2009).

62. B. I. Stepanov, "Frequencies of the axial modes of a composite cavity " Journal of Applied Spectroscopy **6**, 399-403 (1967).

63. D. Hollenbeck, and C. D. Cantrell, "Parallelizable, Bidirectional Method for Simulating Optical-Signal Propagation," Journal of Lightwave Technology **27**, 2140-2149 (2009).

64. J. Q. Cao, Q. S. Lu, S. P. Chen, J. Hou, and X. J. Xu, "Effect of polarization controlling on coherent beam combining of two-fiber laser arrays of interferometric configuration," Optics Letters **34**, 133-135 (2009).

65. "FFTW (Fastest Fourier Transform in the West)," http://www.fftw.org/.

66. A. Brignon, *Phase Conjugate Laser Optics* (John Wiley & Sons, Inc., 2004).

67. E. N. Leith, and Upatniek.J, "HOLOGRAPHIC IMAGERY THROUGH DIFFUSING MEDIA," Journal of the Optical Society of America **56**, 523-& (1966).

68. S. Weiss, S. Sternklar, and B. Fischer, "DOUBLE PHASE-CONJUGATE MIRROR - ANALYSIS, DEMONSTRATION, AND APPLICATIONS," Optics Letters **12**, 114-116 (1987).

69. S. Ayotte, H. S. Rong, S. B. Xu, O. Cohen, and M. J. Paniccia, "Multichannel dispersion compensation using a silicon waveguide-based optical phase conjugator," Optics Letters **32**, 2393-2395 (2007).

70. S. Ayotte, S. Xu, H. Rong, O. Cohen, and M. J. Paniccia, "Dispersion compensation by optical phase conjugation in silicon waveguide," Electronics Letters **43**, 1037-1039 (2007).

71. A. Yariv, D. Fekete, and D. M. Pepper, "COMPENSATION FOR CHANNEL DISPERSION BY NON-LINEAR OPTICAL PHASE CONJUGATION," Optics Letters **4**, 52-54 (1979).

72. T. Bach, K. Nawata, M. Jazbinsek, T. Omatsu, and P. Gunter, "Optical phase conjugation of picosecond pulses at 1.06 mu m in Sn2P2S6:Te for wavefront correction in high-power Nd-doped amplifier systems," Optics Express **18**, 87-95.

73. A. Mocofanescu, and K. D. Shaw, "Stimulated Brillouin scattering phase conjugating long multimode optical fibers properties," Optics Communications **266**, 307-316 (2006).

74. G. T. Moore, "A model for diffraction-limited high-power multimode fiber amplifiers using seeded stimulated brillouin scattering phase conjugation," Ieee Journal of Quantum Electronics **37**, 781-789 (2001).

75. A. Yariv, "PHASE CONJUGATE OPTICS AND REAL-TIME HOLOGRAPHY," Ieee Journal of Quantum Electronics **14**, 650-660 (1978).

76. L. Reekie, R. J. Mears, S. B. Poole, and D. N. Payne, "TUNABLE SINGLE-MODE FIBER LASERS," Journal of Lightwave Technology **4**, 956-960 (1986).

77. M. C. Farries, P. R. Morkel, and J. E. Townsend, "SAMARIUM3+-DOPED GLASS-LASER OPERATING AT 651-NM," Electronics Letters **24**, 709-711 (1988).

78. M. Yamada, M. Shimizu, Y. Ohishi, T. Kanamori, S. Sudo, and J. Temmyo, "GAIN CHARACTERISTICS OF PR3+-DOPED FLUORIDE FIBER AMPLIFIER," Electronics and Communications in Japan Part Ii-Electronics **77**, 75-87 (1994).

79. C. Ghisler, W. Luthy, and H. P. Weber, "TUNING OF A TM3+HO3+-SILICA FIBER LASER AT 2 MU-M," Ieee Journal of Quantum Electronics **31**, 1877-1879 (1995).

80. S. A. Babin, D. V. Churkin, A. E. Ismagulov, S. I. Kablukov, and E. V. Podivilov, "Turbulence-induced square-root broadening of the Raman fiber laser output spectrum," Optics Letters **33**, 633-635 (2008).

81. S. A. Babin, D. V. Churkin, A. E. Ismagulov, S. I. Kablukov, and E. V. Podivilov, "Spectral broadening in Raman fiber lasers," Optics Letters **31**, 3007-3009 (2006).

82. S. H. Huang, G. S. Qin, Y. Feng, A. Shirakawa, M. Musha, and K. I. Ueda, "Single-frequency fiber laser from linear cavity with loop mirror filter and dual-cascaded FBGs," Ieee Photonics Technology Letters **17**, 1169-1171 (2005).

83. M. Engelbrecht, A. Ruehl, D. Wandt, and D. Kracht, "Single-frequency ytterbium-doped fiber laser with 26 nm tuning range," Optics Express **15**, 4617-4622 (2007).

84. N. Jovanovic, M. Aslund, A. Fuerbach, S. D. Jackson, G. D. Marshall, and M. J. Withford, "Narrow linewidth, 100 W cw Yb3+-doped silica fiber laser with a point-by-point Bragg grating inscribed directly into the active core," Optics Letters **32**, 2804-2806 (2007).

85. N. Vermeulen, C. Debaes, A. A. Fotiadi, K. Panajotov, and H. Thienpont, "Stokes-anti-Stokes iterative resonator method for modeling Raman lasers," Ieee Journal of Quantum Electronics **42**, 1144-1156 (2006).

86. J. Auyeung, and A. Yariv, "THEORY OF CW RAMAN OSCILLATION IN OPTICAL FIBERS," Journal of the Optical Society of America **69**, 803-807 (1979).

87. H. G. Winful, and G. D. Cooperman, "Self-Pulsing and Chaos in Distributed Feedback Bistable Optical-Devices," Applied Physics Letters **40**, 298-300 (1982).

88. K. Ikeda, "Multiple-Valued Stationary State and Its Instability of the Transmitted Light by a Ring Cavity System," Optics Communications **30**, 257-261 (1979).

89. K. Ikeda, H. Daido, and O. Akimoto, "Optical Turbulence - Chaotic Behavior of Transmitted Light from a Ring Cavity," Physical Review Letters **45**, 709-712 (1980).

90. L. Dong, G. E. Berkey, P. Chen, and D. L. Weidman, "Resonant ring fiber filters," Journal of Lightwave Technology **18**, 1018-1023 (2000).

91. J. M. Fini, R. T. Bise, M. F. Yan, A. D. Yablon, and P. W. Wisk, "Distributed fiber filter based on index-matched coupling between core and cladding," Optics Express **13**, 10022-10033 (2005).

92. J. Limpert, N. D. Robin, I. Manek-Honninger, F. Salin, F. Roser, A. Liem, T. Schreiber, S. Nolte, H. Zellmer, A. Tunnermann, J. Broeng, A. Petersson, and C. Jakobsen, "High-power rod-type photonic crystal fiber laser," Optics Express **13**, 1055-1058 (2005).

93. W. S. Wong, X. Peng, J. M. McLaughlin, and L. Dong, "Breaking the limit of maximum effective area for robust single-mode propagation in optical fibers," Optics Letters **30**, 2855-2857 (2005).

94. L. Dong, J. Li, and X. Peng, "Bend-resistant fundamental mode operation in ytterbium-doped leakage channel fibers with effective areas up to 3160 mu m(2)," Optics Express **14**, 11512-11519 (2006).

95. M. Heiblum, and J. H. Harris, "ANALYSIS OF CURVED OPTICAL-WAVEGUIDES BY CONFORMAL TRANSFORMATION," Ieee Journal of Quantum Electronics **QE11**, 75-83 (1975).

96. D. Marcuse, "BEND LOSS OF SLAB AND FIBER MODES COMPUTED WITH DIFFRACTION THEORY," Ieee Journal of Quantum Electronics **29**, 2957-2961 (1993).

97. J. Sakai, and T. Kimura, "BENDING LOSS OF PROPAGATION MODES IN ARBITRARY-INDEX PROFILE OPTICAL FIBERS," Applied Optics **17**, 1499-1506 (1978).

98. K. Thyagarajan, M. R. Shenoy, and A. K. Ghatak, "ACCURATE NUMERICAL-METHOD FOR THE CALCULATION OF BENDING LOSS IN OPTICAL WAVE-GUIDES USING A MATRIX APPROACH," Optics Letters **12**, 296-298 (1987).

99. R. L. Espinola, R. U. Ahmad, F. Pizzuto, M. J. Steel, and R. M. Osgood, "A study of high-index-contrast 90 degrees waveguide bend structures," Optics Express **8**, 517-528 (2001).

100. A. Jiang, S. Y. Shi, G. Jin, and D. W. Prather, "Performance analysis of three dimensional high index contrast dielectric waveguides," Optics Express **12**, 633-643 (2004).

101. N. N. Feng, G. R. Zhou, C. L. Xu, and W. P. Huang, "Computation of full-vector modes for bending waveguide using cylindrical perfectly matched layers," Journal of Lightwave Technology **20**, 1976-1980 (2002).

102. K. Kakihara, N. Kono, K. Saitoh, and M. Koshiba, "Full-vectorial finite element method in a cylindrical coordinate system for loss analysis of photonic wire bends," Optics Express **14**, 11128-11141 (2006).

103. T. Yamamoto, and M. Koshiba, "NUMERICAL-ANALYSIS OF CURVATURE LOSS IN OPTICAL WAVE-GUIDES BY THE FINITE-ELEMENT METHOD," Journal of Lightwave Technology **11**, 1579-1583 (1993).

104. S. J. Li, and Y. Y. Lu, "Accurate Multipole Analysis for Leaky Microcavities in Two-Dimensional Photonic Crystals," Ieee Photonics Technology Letters **22**, 94-96.

105. S. Kim, and A. Gopinath, "Vector analysis of optical dielectric waveguide bends using finite-difference method," Journal of Lightwave Technology **14**, 2085-2092 (1996).

106. Z. Y. Li, and L. L. Lin, "Photonic band structures solved by a plane-wave-based transfer-matrix method," Physical Review E **67** (2003).

107. Z. Ye, X. H. Hu, M. Li, K. M. Ho, and P. D. Yang, "Propagation of guided modes in curved nanoribbon waveguides," Applied Physics Letters **89** (2006).

108. M. Koshiba, and K. Inoue, "SIMPLE AND EFFICIENT FINITE-ELEMENT ANALYSIS OF MICROWAVE AND OPTICAL WAVE-GUIDES," Ieee Transactions on Microwave Theory and Techniques **40**, 371-377 (1992).

109. M. Koshiba, and Y. Tsuji, "Curvilinear hybrid edge/nodal elements with triangular shape for guided-wave problems," Journal of Lightwave Technology **18**, 737-743 (2000).

110. Y. Tsuchida, K. Saitoh, and M. Koshiba, "Design of single-moded holey fibers with large-mode-area and low bending losses: The significance of the ring-core region," Optics Express **15**, 1794-1803 (2007).

111. T. W. Wu, L. Dong, and H. Winful, "Bend performance of leakage channel fibers," Optics Express **16**, 4278-4285 (2008).

112. L. Dong, X. Peng, and J. Li, "Leakage channel optical fibers with large effective," Journal of the Optical Society of America B-Optical Physics **24**, 1689-1697 (2007).

113. J. R. Marciante, "Gain Filtering for Single-Spatial-Mode Operation of Large-Mode-Area Fiber Amplifiers," Ieee Journal of Selected Topics in Quantum Electronics **15**, 30-36 (2009).